Tissue Classification from Electric Impedance Spectroscopy for Haptic Feedback in Minimally Invasive Surgery

by

Brayden Kent

A thesis submitted to the

School of Graduate and Postdoctoral Studies in partial

fulfillment of the requirements for the degree of

Master of Applied Science in Mechanical Engineering

Faculty of Engineering and Applied Science

University of Ontario Institute of Technology (Ontario Tech University)

Oshawa, Ontario, Canada

October 2020

Abstract

Haptic feedback is missing in teleoperated surgical robots creating a sensory disconnect from the surgeon and their patient. This thesis proposes using the electric impedance of tissues, instead of the traditionally used mechanical impedance, to develop haptic feedback for surgical robots. Electric impedance spectroscopy (EIS) and a modified surgical needle were successfully able to measure the electric impedance for gel-based phantoms, ex-vivo tissue, and freshly excised organs. Processes for fitting the electric impedance of these tissues to the double-dispersion Cole model were developed including stochastic and deterministic approaches. The tissues were classified with least square error, k-Nearest Neighbour and Naïve Bayes using the measured electric impedance and the extracted model parameter values. The thesis culminates in applications of using EIS as part of implementing vibrotactile and force feedback applications involving sets of user trials to validate its effectiveness in identifying the tissue through haptic feedback.

Keywords: Electric Impedance Spectroscopy; Haptics; Surgical Robots; Tissue Classification

Author's Declaration

I hereby declare that this thesis consists of original work of which I have authored. This is a true copy of the thesis, including any required final revisions, as accepted by my examiners.

I authorise the University of Ontario Institute of Technology (Ontario Tech University) to lend this thesis to other institutions or individuals for the purpose of scholarly research. I further authorise University of Ontario Institute of Technology (Ontario Tech University) to reproduce this thesis by photocopying or by other means, in total or in part, at the request of other institutions or individuals for the purpose of scholarly research. I understand that my thesis will be made electronically available to the public.

BRAYDEN KENT

Statement of Contribution

Parts of the works described in **Chapter 1** and **Chapter 5** has been accepted for publication as:

B. Kent, A. Cusipag, and C. Rossa - Tissue discrimination through force-feedback from impedance spectroscopy in robot-assisted surgery. International Conference on Smart Multimedia, San Diego, Dec 2019, pp. 274–285, 2019, doi: 10.1007/978-3-030-54407-2_23.

At the time of writing, the contents of the following submitted paper currently under review are used in **Chapter 2**, **Chapter 3**, **Chapter 4** and **Chapter 5**:

B. Kent, and C. Rossa - Development of a Rapid Tissue Discrimination Electrode Embedded Surgical Needle using Vibro-Tactile Feedback derived from Electric Impedance Spectroscopy. Medical & Biological Engineering & Computing, 2020

Part of the work in **Chapter 3** and **Chapter 4** has been accepted for publication as: B. Kent, and C. Rossa - Tissue Discrimination from Impedance Spectroscopy as a Multi-objective Optimisation Problem with Weighted Naïve Bayes Classification, IEEE International Conference on Systems, Man, and Cybernetics, October 2020

Acknowledgements

I would like to thank my supervisor, Dr. Carlos Rossa, for his seemingly endless patience and guidance over these last few years. This thesis would not have been possible without it. I have learned more than I could have thought possible while working in the Biomechatronics lab.

I am truly grateful to my family, Diane, Steve and Chelsea, whose support helped me achieve my goals.

I would also like to thank the staff of Taunton Road Animal Hospital in providing tissue samples for my research.

Lastly, I would like to thank Nicole for always believing in me.

Contents

List of Figures

List of Tables

List of Abbreviations and Symbols

Abbreviations	
AC	Alternating current
EIS	Electric impedance spectroscopy
kNN	k-Nearest Neighbours
LSE	Least square error
NBC	Naïve Bayes Classifier
PSO	Particle Swarm Optimisation
RMIS	Robot-aided minimally invasive surgery
RPD-NSGA-II	Reference point dominance, non-dominated sorting genetic algorithm
Chapter 2	
V	Voltage (Generic)
I	Electric current (Generic)
R	Resistance (Generic)
V_0	Amplitude of a sinusoidal voltage signal
I_0	Amplitude of a sinusoidal current signal
ω	Frequency of the applied stimulus signal (rad/s)
θ	Phase shift of the sinusoidal signal
X	Electrical reactance (Generic)
j	The imaginary unit $\sqrt{-1}$
f	Frequency of the sinusoidal signal
$|Z(\omega)|$	Magnitude of the impedance at a given frequency
$\angle Z(\omega)$	Phase of the impedance at a given frequency
R_e	Electrode resistance
C_e	Electrode capacitance
L_{ca}	Effective capacitor length
r_{si}	Inner radius of the needle shaft
r_{so}	Outer radius of the needle shaft
r_c	Radius of the core electrode

ϵ_r	Relative permittivity of the dielectric
ϵ_0	Permittivity of free space
ρ_c	Resistivity of the core material
ρ_c	Resistivity of the needle shaft
L_c	Length of the core material
L_s	Length of the needle shaft
$\mathbf{f}$	Vector: Frequencies measured at in experiments
$Z(\omega)$	Impedance of the tissue, dependent on frequency
V_{Exc}	The excitation voltage signal
V'_{Exc}	The estimated excitation voltage signal
I_{Exc}	The excitation current signal
R_{Ref_1}, R_{Ref_2}	Reference resistance
V_{Res}	Measured voltage response across the tissue
Chapter 3	
R_∞	Double-dispersion model high frequency resistance
R_1, R_2	Double-dispersion model resistance
C_1, C_2	Double-dispersion model capacitance
α_1, α_2	Dispersion coefficient
$\mathbf{p}$	Vector: equivalent circuit model parameters
Z_w	Warburg impedance
n	Number of unique frequencies the impedance is measured at
$\hat{\mathbf{z}}$	Vector: calculated impedance determined by the model
$\mathbf{z}$	Vector: measured impedance
E	Least square error of calculated and measured impedance
$\mathbf{J}$	Matrix: Jacobian/sensitivity of impedance to parameter change
δ	Small number to aid in Jacobian approximation
λ	Small number to help prevent singular matrices during inversion
$\mathbf{I}$	Matrix: Identity, ones along diagonal
$\mathbf{p}^{i+1}$	Vector: next iteration of model parameters
$\mathbf{p}^i$	Vector: current iteration of model parameters

$\hat{\mathbf{z}}^{i-1}$	Vector: previous iteration of model impedance
$\hat{\mathbf{z}}^{i}$	Vector: current iteration of model impedance
$\Delta\mathbf{p}^{i}$	Vector: changes to current iteration of model parameters
κ	Vector: learning rates on each parameter
$\mathbf{p}^{o}$	Vector: initial guess of model parameters
$\mathbf{p}_1^{o} ... \mathbf{p}_5^{o}$	Parameter value at the index in subscript
$\mathbf{z}_{(\omega_1)} ... \mathbf{z}_{(\omega_n)}$	Impedance value at index in subscript
$e_1 ... e_3$	Values to assess convergence of optimiser
$\mathbf{z}_m$	Vector: measured impedance magnitude
$\mathbf{z}_p$	Vector: measured impedance phase
$\hat{\mathbf{z}}_m$	Vector: calculated impedance magnitude determined by the model
$\hat{\mathbf{z}}_p$	Vector: calculated impedance phase determined by the model
W	Set of reference points
m	Number of objective functions
v	Number of hyper-plane divisions
d_1, d_2	Distance to the reference points
ζ_c	Crossover rate for the genetic algorithm
ζ_m	Mutation rate for the genetic algorithm
N	Population size for the genetic algorithm
Chapter 4	
$|\mathbf{z}|_{\mathbf{t},\mathbf{n}}$	Vector: impedance magnitude of the sample from test data set
$|\mathbf{z}|_{\mathbf{s},\mathbf{n},\mathbf{x}}$	Vector: impedance magnitude of the sample from training data set
$(\angle\mathbf{z})_{\mathbf{t},\mathbf{n}}$	Vector: impedance phase of the sample from test data set
$(\angle\mathbf{z})_{\mathbf{s},\mathbf{n},\mathbf{x}}$	Vector: impedance phase of the sample from training data set
x	Index of the current sample used in the training data set
n	Index of the frequency
$w_{f,n}$	Weight of the impedance error at a frequency
$\mathbf{v}_i$	PSO: vector of population member velocities at generation i
c_1, c_2	PSO: Personal and global best error weight
r_1, r_2	PSO: Random numbers between 0 and 1

$\mathbf{p}_i$	PSO: vector of population member values for circuit model parameters
$\mathbf{w}_{p,j}$	Vector: weight of the parameter error at index j
$\mathbf{p_{t,j,i}}$	Vector: j^{th} parameter in the ith test sample population member
$\mathbf{p_{s,j,q,x}}$	Vector: j^{th} parameter in the qth solution of the xth training sample
$\mathbf{p}_{t,j}$	kNN: j^{th} parameter of the test sample population member
$\mathbf{p}_{s,j}$	kNN: j^{th} parameter of the training sample population member
$P(c_k|\mathbf{p}_j)$	NBC: Probability of a given class given a model parameter
$P(\mathbf{p}_m|c_k)$	NBC: Probability of a model parameter given a class
$P(c_k)$	NBC: Probability of a given class occurring
$P(\mathbf{p}_j)$	NBC: Probability of a given model parameter occurring
Chapter 5	
K	Mechanical stiffness of the tissue
γ_1	Conversion factor for stiffness and electric impedance
$Z(\omega)$	Electric impedance at frequency ω
F	Tissue cutting force
γ_2	Conversion factor for stiffness and cutting force
γ	Conversion factor to relate cutting force to electric impedance
$F(d)$	Displayed haptic force at depth d
$Z_i(\omega,d)$	i^{th} measurement of the impedance at frequency ω and depth d
n	Number of measurements
$Z(\omega,0)$	Impedance at frequency ω and depth $d=0$
v	Poisson's ratio
F_k	Indentation force
x	Indentation depth
a	Indenter radius

Chapter 1

Challenges and Solutions in Tissue Discrimination during Minimally Invasive Surgery

1.1 Introduction

Robot-assisted minimally invasive surgery (RMIS) has shown increasing promise in improving the quality of treatment in the operating room. Typically, the goal of tele-operated RMIS systems is to enhance the dexterity and precision of the surgeon rather than having robots replace them in the operating room. Through a remote console, the surgeon controls a robotic manipulator that operates on the patient, see Figure 1.1. However, the lack of force feedback in the currently available commercial systems presents a steep learning curve for novice surgeons to become proficient in RMIS and achieve the desired levels of performance. In some minimally invasive procedures, the surgeon can rely on other forms of sensory feedback such as laparoscopic cameras to visualise the surgical site. Yet, this is not always a feasible solution for percutaneous procedures such as brachytherapy.

Brachytherapy is a surgical procedure that utilises radiation for cancer treatment. The surgery is often used in the treatment of breast and prostate cancers where there are two approaches that can be taken: low-dose-rate and high-dose-rate. The lower dose refers to implanting radioactive seeds into the tissue, where they will remain permanently, irradiating nearby tumours over time. The higher dose alternative is temporary, lasting a few minutes in specially designed guide tubes to the tissue. In both cases the surgeon inserts needles into the organ typically guided by ultrasound imaging. In the past two decades, there has been growing interest in improving the technique with robot-assisted technologies [1] [2], including the implementation of haptic feedback [3]. This push is driven by challenges in accurately locating lesions during treatment, resulting in radiation being needlessly applied to healthy tissue.

The first issue presents itself in the form of loss of tactile information. In the early stages of cancer screening, clinicians are able to use palpation to identify possible abnormalities. The sense of touch is what enables them to feel the change in tissues, alerting them to possible issues. While this is useful for screening, it is not feasible to do during further surgery such as biopsy or treatment in brachytherapy. While

inserting brachytherapy or biopsy needles, it is a difficult task to perceive the change in tissue stiffness by hand. The loss of this tactile feedback presents a loss of key information to the surgeon that could aid them in identifying the location of tumours.

The second challenge is the interpretation of imaging methods. The current gold standard in breast cancer diagnosis is fine-needle aspiration biopsy, in which the procedure is used in tandem with some form of medical imaging, typically ultrasound, and the expertise of the pathologist to sample suspect lesions for malignancy. During these procedures the clinician identifies regions of interest depending on, among other properties, the echogenicity of the tissue [4]. Hyperechoic regions are indicative of benign lesions. In contrast, hypoechoic regions are regions of interest for malignant tissue [5]. However, it is not sufficient to simply rely on echogenicity to diagnose tissue malignancy, and biopsy is typically used to give histological assessment. These challenges are not limited to the breast; similar difficulties are seen in other tissues as well, including prostate cancer.

In prostate cancer biopsy, the needles are guided using transrectal ultrasound. Similar to the breast tissue, not all tissue structures like cancerous tumours are identifiable on ultrasound images. Physicians can target hypoechoic regions but it has been reported that some prostate cancers are difficult to detect with traditional grayscale ultrasound images [5]. This inability to identify cancerous regions requires multiple biopsy tissue samples at various locations in the prostate without targeting suspicion lesions [6]. A longitudinal study from 2007 found that over 25% of patients were under diagnosed and up to 7.1% were over diagnosed [7], which may result in unnecessary or insufficient treatment. Furthermore, as false-negatives can occur, one may attempt repeated sampling, been this has not necessarily shown an improvement in cancer detection [8] [9]. Since the biopsy only samples a small volume of the tissue and different types of tissue may be observed by similar ultrasound characteristics, it is worthwhile to explore how these types of procedures could be improved.

A different approach could be to explore medical imaging techniques other than ultra-

sound. CT scans and X-ray imaging are able to delineate tumours [10], but segmentation is non-trivial and with the radiation exposure makes it unsuitable for online treatment and guidance. Similarly, MRI [9] is well known for identifying suspect lesions, but the size and cost make them prohibitive to use in routine surgical procedures. Consequently, as an alternative to image-based tissue targeting, there has been a great deal of research invested in implementing haptic feedback in teleoperation systems as a method of communicating tissue composition.

1.1.1 Haptic Feedback with Surgical Robots

Surgical robots like the da Vinci system are among the more popular teleoperation tools for surgery. The system, and many others like it, are composed primarily of three parts: the robotic manipulator(s), visualisation/imaging, and the remote control console. The surgeon operates on the patient by controlling the robot through this console. In the context of the da Vinci robot, the surgeon can view the surgical site with an endoscopic camera connected to a 3D display, and the actuation of the tools connected to the manipulator arms can be controlled with joysticks and foot pedals. In [11] it was found that experienced surgeons applied inconsistent suture tension when performing the task with the da Vinci robot. The research further investigates solutions to incorporating feedback, including audible and visual cues, to improve precision and accuracy in teleoperation [11].

Similar investigations to develop haptic feedback have occurred with other surgical robots, like the AESOP robotic arms controlled by a PHANToM haptic device in [12], where a force sensor was installed at the with a scalpel tool and forceps such that force feedback could be calculated and displayed. Several other researchers have attempted to augment surgical tools with force sensors [13] [14].

The motivation to use force sensors is that it is relatively intuitive to communicate force measurements to a perceived force by the operator through a haptic device. In the context of biopsy or brachytherapy it is well-known that the mechanical properties of tumours are different than that of their healthy tissue counterpart. With a force

sensor installed on the tool, one should be able to measure a difference in the stiffness of the tissue as the tool is inserted during the procedure. Unfortunately, depending on the location of the force sensor, there are associated challenges. A force sensor installed at the base of the tool, outside of the body, will be subject to noise since the sensor will measure friction, cutting and puncturing forces simultaneously, among others [15] [16]. To mitigate this, one could try to install a force sensor at the tip of the tool [16], where ideally the tissue stiffness would be the main contributor to the measurement. This is a non-trivial task however, as the needle tip poses additional constraints, namely limited size and degrees of freedom [17].

As a result there has been increasing interest in developing new technologies to aid in the discrimination of different tissues in minimally invasive surgery. There have been approaches that attempt to utilise the mechanical properties of the tissue, but there are additional properties of the tissue that could be potentially exploited.

1.1.2   A New Approach

It is intuitive to connect the mechanical properties to physical haptic feedback, but there are associated challenges with these methods. It is then worthwhile exploring what other information could be extracted and utilised. Notably, tissues do need to be characterised solely on their mechanical properties, as organic tissues also have been reported to possess unique electric and dielectric properties [18]. Researchers have found such behaviour in benign and malignant tissues for several organs, including in the prostate [19], breast [20], bladder [21] and skin [22].

One such technology that can discern this electrical information is the method of electric impedance spectroscopy (EIS). The method involves applying an alternating current stimulus across a sample and measuring the resulting response, at a wide range of frequencies. The following will discuss the origins of this method and how it came to be of interest to research in identification of various tissues.
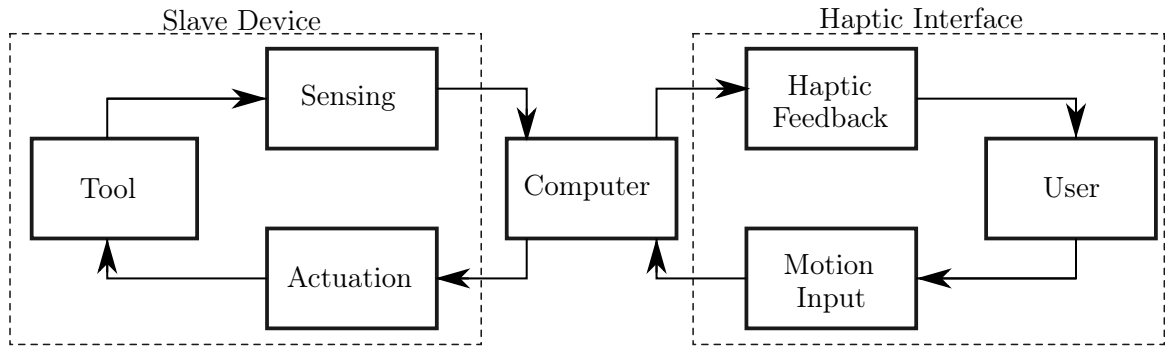
Figure 1.1: A flow diagram representing the system that composes a teleoperation haptic interface.

1.2 Electric Impedance Spectroscopy

The method of electrical impedance spectroscopy has a long history, evolving from of the works of Issac Newton and studies on the effects of electromagnetic waves on materials. The study of how material interacts with electromagnetic radiation became known as spectroscopy. In the late 1800s researchers began to explore how materials would react to alternating electric current of various frequencies. Heaviside is regarded as the first to coin the term for electric impedance.

In its essence, electric impedance spectroscopy (EIS) is the analysis of a system's impedance as it is applied with alternating current of various frequencies. This research has evolved over the past century and has become relevant to the analysis of many different applications. While this thesis focuses on the application to biological tissues, there is a thriving field of research in the analysis of electrochemical cells since, by its very nature, EIS is heavily intertwined with electrochemistry. For the sake of clarity it is important to note that bioimpedance analysis and EIS, while related in principles, traditionally investigate different topics. In the literature, the term bioimpedance is generally associated in analysis of impedance for the whole body, where electrodes are placed across multiple limbs, to study body composition such as body fat and muscle mass. In electric impedance spectroscopy with biological tissues, one is more concerned about the analysis of small groups of (or in some cases individual) cells.

A thorough review of EIS history is provided by Schwan and Foster in [23]. In gist, the analysis of applying electric stimulus to tissue began in the later 1800's. Over time it was understood that electric stimulus will cause cells to react on a microscopic level where ions act as charge carriers in the tissue. How well these ions are able to carry charge became a measure of the tissue's conductivity. Since the inception of EIS, tissues have been known to exhibit complex dielectric behaviour. The mobility of these ions within the cells leads to formation of effects such as polarisation, and double-layer capacitance at the electrode-electrolyte interface. Thus, the permittivity of tissues also became a matter of interest to researchers. Through the turn of the century, and into the modern era, there has been specific interest in the application of EIS to medical technology. Specifically, in the works published by Halter et al., there is a difference in the conductivity and permittivity in prostate tissues: notably carcinoma and benign hyperplasia, where current technology is challenged in differentiating them [24]. Among other similar findings there is a recent thrust in the past decade to integrate EIS with surgical tools.

The advantage to adopting EIS over traditional force sensor approaches is not to be understated. As stated above, there are challenges with friction obscuring tissue stiffness when using force sensors at the base of the needle - and integrating these sensors at the tip of the needle is non-trivial. The capabilities in micro-machining methods have improved considerably in recent years, enabling electrodes to be integrated directly onto needles without impeding their surgical function [25] [26].

Provided that EIS is capable of of discriminating between tissues and can be integrated with surgical instruments, there is an opportunity to explore it's viability in a haptic feedback system. Depending on the frequencies measured, and how many samples are taken per measurement, EIS could rapidly acquire impedance information about the tissue. The post-processing of this data is also a factor, if the data is fit to a model for instance, additional processing time is required. Considering this can be done rapidly, the method would be able to identify tissue fast enough to be used in a haptic feedback system, ideally in real-time.

1.3 Objectives and Outline

Presented in this thesis is further development of tissue classification using EIS, but with the novel application to surgical needles and haptic feedback. The following chapters of this manuscript will range from the development of a prototype EIS electrode-embedded needle, the implementation of a fitting method to extract the properties of the tissue from EIS, the classification procedures, to culminating in two example applications. The thesis will conclude by reviewing the success of the presented ideas, and recommendations for further development.

Chapter 2 will introduce an provide and overview of the system developed to acquire EIS data and how it relates to similar designs seen in other publications. The chapter continues to explain how the system is used to acquire assorted tissue sample data from frequencies of 10.4 Hz to 349 kHz. The tissue samples include gel based phantoms, ex-vivo (poultry, bovine) tissue, and freshly excised (canine, feline) tissue. Lastly, a comparison of the EIS data for these tissues is discussed.

Chapter 3 builds upon the former chapter, where the collected data is fit to a circuit model that represents the electric properties of the tissue samples. The chapter will introduce the purpose of these circuit models and their development. The later sections detail the processes used to extract the parameters of the model for each tissue sample, using both single and multi-objective optimisation approaches.

In Chapter 4, a few approaches are explored on how EIS data and model parameters can be used classify new tissue samples. The analysis includes a comparison of least square error to a database of existing samples, k-Nearest Neighbours, and Naïve Bayes classification. The effectiveness of these methods is also discussed.

With the EIS system and classification algorithms developed, the applications to haptic feedback are explored in Chapter 5. The chapter presents two studies where the content discussed in the former chapters culminate. In the first study a prototype needle provides vibrotactile feedback to the wielder; informing them of the tissue

at the needle tip. In the second study the system is integrated to a teleoperation scenario, where a remote user receives haptic force feedback; alerting them about tissue composition at the needle tip.

Chapter 6 will summarise the developments of the thesis. Alongside concluding remarks, recommendations are suggested for future developments of the system and proposed techniques.

The contributions of this thesis are:

- Tissue classification with an electrode embedded needle using electric impedance spectroscopy with a combined database containing gel-based phantoms, ex-vivo tissue and, and freshly excised tissue.

- Fitting electric impedance measurements to the double-dispersion Cole model with the RPD-NSGA-II algorithm.

- Generating haptic feedback from electric impedance spectroscopy. Force and vibrotactile feedback applications investigated.

Chapter 2

An Electrode Embedded Needle for Tissue Discrimination

2.1 Electric Impedance

The objective of EIS is to analyse the properties of an object by applying electric stimulus of varying frequencies. To achieve this, the electric impedance of the tissue needs to be known. The fundamental equation in defining electric impedance is defined by Ohm's Law,

$$R = \frac{V}{I} \tag{2.1}$$

where the resistance R is a measure of an object's ability to impede the flow of electric current. It is evaluated as the ratio of the electric potential difference, voltage V, across the object, over the current I through it. The relationship in (2.1) is applicable in a purely resistive element. As mentioned in the previous chapter, the electric impedance of tissues changes with frequency of the excitation signal. Thus, a more general consideration of (2.1) for alternating current (AC) should be considered. In the time domain, the excitation signal can be written as,

$$V(t) = V_0 \sin(\omega t) \tag{2.2}$$

with V_0 as the amplitude of the voltage signal. The angular frequency is $\omega = 2\pi f$, where f is the inverse of the excitation signal period, in Hz. Similarly, the current can be defined, and is relative to the voltage by a phase shift of θ,

$$I(t) = I_0 \sin(\omega t + \theta) \tag{2.3}$$

This enables deriving the AC impedance using Euler's formula and the ratio defined in (2.1),

$$Z(\omega) = R + X(j\omega) \tag{2.4}$$

with the impedance Z comprised of the resistance R and the reactance X. $j = \sqrt{-1}$ is the imaginary unit. The impedance can also be represented as the magnitude and phase,

$$|Z(\omega)| = \sqrt{R^2 + X^2} \tag{2.5}$$

$$\angle Z(\omega) = \tan^{-1}\left(\frac{X}{R}\right) \tag{2.6}$$

There are multiple ways to visualise the change in impedance with respect to frequency, but the most commonly used forms include the Nyquist plot, where impedance is plotted on the complex plane, or a Bode plot, where magnitude and phase of the impedance are plotted separately against frequency, see Figure 2.1. In EIS literature plotting on the complex plane is more-often seen, but this manuscript will utilise the Bode representation.

(a)   (b)
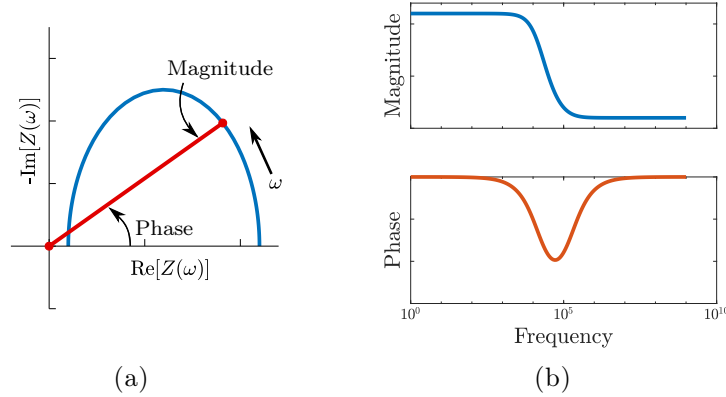
Figure 2.1: (a) An example of a Nyquist plot where the impedance is plotted on the complex plane. (b) An example of a Bode plot where the impedance is plotted in two parts, the magnitude and phase. Both figures illustrate how the impedance change with respect to frequency.

With electric impedance defined, the following sections detail how the electric impedance of tissue can be measured, and the system developed to acquire the impedance information will be introduced.

2.2 Existing Implementations of Needle Probes

In the current state of the art, several instruments have been developed to differentiate healthy and cancerous cells through their electrical characteristics. NASA and BioLuminate Inc. developed a biopsy probe to identify breast cancer through electric impedance [27]. Yun et al. utilized an electrode embedded needle to identify thyroid cancer [28]. Park et al. integrated a microelectrode array onto a biopsy needle for liver cancer discrimination [29].

From the literature it is seen that there are multiple different possible configurations to conduct EIS. Perhaps the most intuitive approach is the bipolar configuration, shown in Figure 2.2(a), where two electrodes are placed across the tissue. An AC voltage is applied to the tissue and the resulting current is measured in-line [30]. The impedance of the tissue is found from the ratio of the applied voltage over the current, see (2.1); repeating this process at many frequencies forms the impedance spectrum of the tissue. One known drawback to the bipolar approach is that electrodes can become polarised, resulting a source of error in the measurement [31]. Polarisation is caused by the ions in the metal electrode reacting with the ions in the electrolyte of the tissue. As negatively charged ions collect on the surface of the electrode, negative ions are attracted to them, behaving like two charged plates of capacitor. This layer of negative ions in the electrolyte solution will further attract positive ions forming a secondary layer. This phenomenon is referred to as double layer capacitance. Electrode polarisation is more noticeable during low frequency measurements [32] [33], as there is more time for charge to build on surface of the electrode interface. In higher frequency analysis, this effect is negligible as there is insufficient time to polarise the electrode before the polarity is switched on the excitation signal. Despite the existence of electrode polarisation in bipolar configurations, as shown in [33] tissue classification can still be conducted. Furthermore, one can compensate for this phenomena by considering it in the system model [32].

The tetrapolar configuration is another popular approach, where two pairs of elec-

trodes are used, which solves the issue with electrode polarisation. One pair injects current through the tissue and potential difference is measured across the other pair of electrodes, see Figure 2.2(b).

(a)   (b)
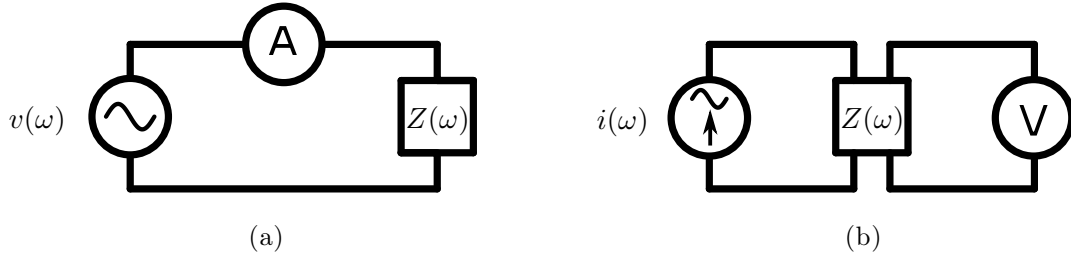
Figure 2.2: (a) A bipolar EIS arrangement where two electrodes are attached to an object with unknown, frequency dependent impedance $Z(\omega)$ where a voltage is applied and current is measured in line. (b) A tetrapolar EIS arrangement where the applied signal electrodes are separate from the measurement electrodes, requiring four electrodes attached to the object. The current is injected into the object and voltage is measured.

The existing designs of electrode embedded needles seen in literature tend more often to adopt the bipolar configuration [31] [34] [19], however monopolar, tripolar and tetrapolar configurations exist [35]. In a coaxial bipolar configuration the needle shaft serves as one electrode and the metallic core suspended concentrically inside the needle serves as the secondary electrode, as shown in Figure 2.3(a). While relatively easy to manufacture, the notable flaw with this design in that the bore of the needle is obstructed by the electrode. There have been attempts to circumvent this flaw with different designs. Trebbels et al. used a concentric shaft in lieu of a solid core in their augmented brachytherapy needle [34]. Other researchers have managed to miniaturise electrodes and apply them to the surface of needles [29]. Electrodes on a micrometer scale have been fabricated into needles using photolithography shown in [25]. For the sake of simplicity in the design, the coaxial approach with a solid core electrode was adopted in this thesis. The details of this design are detailed in the following section.

2.3 Prototype Needle With Coaxial Electrode for EIS

In order to validate the concept of using EIS as a means of providing haptic feedback in RMIS, a prototype needle probe was developed using the coaxial bipolar configuration. The concept of the design is shown in Figure 2.3(a).

Keeping the brachytherapy application in mind, an 18 gauge brachytherapy needle (Eckert & Ziegler, New York, USA) was used as part of the design for the EIS probe. The design considers the needle shaft itself to act as one of the electrodes. The other electrode is a copper wire sheathed in PTFE tubing and suspended in the middle of the needle bore. Cyanoacrylate was used to affix the PTFE tubing to the inner wall of the needle shaft. The tip of the electrode was tinned with solder to prevent oxidation and corrosion. Another copper lead is soldered to the base of the needle. Consequently, with the wire from the core and from the shaft routed to the excitation and measurement circuits, the probe was complete.

The impedance of the needle should be known such that its effect is accounted for when measuring the impedance of the tissue. Several models have been proposed to represent the parasitic impedance of coaxial bipolar electrodes [36] [37] [38] [39]. In this thesis the augmented needle's impedance is estimated by a resistor and a capacitor. The model consists of the metals resistance R_e and the capacitance between the two electrodes C_e. The capacitance can be determined from the general form of concentric cylinder capacitors [40],

$$C_e = 2\pi \left(\frac{L_{ca}}{\ln(r_{si}) - \ln(r_c)} \right) \epsilon_r \epsilon_0 \qquad (2.7)$$

where L_{ca} is the effective length of the capacitor, ϵ_r is the relative permittivity factor for the dielectric insulator between the core (subscript c hereinafter) and needle shaft (subscript s hereinafter) which is multiplied by permittivity of free space ϵ_0. The radius of the core and needle bore is r_c and r_{si} respectively, refer to Figure 2.3(b).

The electrode resistance R_e can also be estimated by considering the resistivity of the shaft and core metals ρ_s, ρ_c, their lengths L_s, L_c and radii,

$$R_e = \frac{\rho_c L_c}{\pi r_c^2} + \frac{\rho_s L_s}{\pi (r_{so}^2 - r_{si}^2)} \tag{2.8}$$

The variables for (2.7) and (2.8) are defined in Table 2.1 and in Figure 2.3(b). Using these parameters the capacitance of the electrode is evaluated as $C_e = 31.70$ pF. The resistance of metal electrodes was calculated to be $R_e = 0.24\ \Omega$.

Compared to the tissue impedance values reported in the literature, these values will have a near negligible effect on the entire impedance, and consequently are omitted for the remainder of this thesis. However, one should consider the impedance of the electrode in their own research to confirm its impact on their impedance measurements.

As noted by Schwan, the effects of electrode polarisation should be considered [41]. An additional source of capacitance is caused by the electrode polarisation that occurs on the surface of both electrodes. This frequency dependent impedance is not considered here as part of the needle model, but will be touched upon in the development of the tissue model.

With the prototype needle introduced, the next step is to understand how it is able to apply electric stimulus and measure the impedance of the tissue.

2.4 Impedance Acquisition Device

The prototype needle needs to be connected to circuitry that is able to apply electric stimulus to the tissue as well as measure the response. Several circuits have been developed to accomplish these tasks. The experiments within this thesis utilise the Quadra (Eliko, Tallin, Estonia), a device specifically designed for electric impedance spectroscopy research [42] [43] [44]. Using binary PWM excitation signals, the device
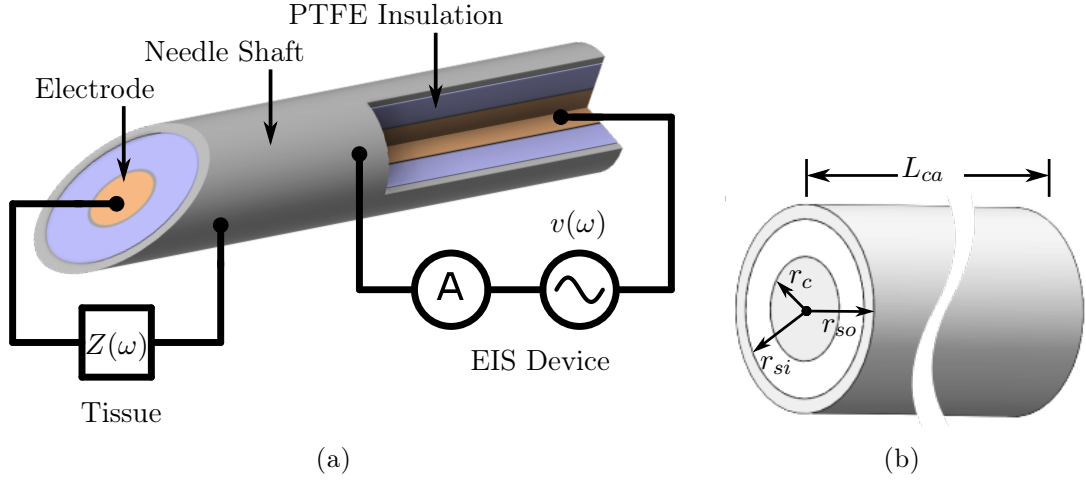
Figure 2.3: A close up view of a model for an electrode embedded needle in a bipolar electrode arrangement for EIS. The two electrodes in this instance are the inner core electrode and the needle shaft. An insulating material, such as polytetrafluoroethylene (PTFE), separates the two electrodes.

Table 2.1: Electrode Needle Parameters

Property	Var.	Value
Resistivity of copper	ρ_c	1.68×10^{-8} Ωm
Resistivity of steel	ρ_s	6.90×10^{-7} Ωm
Radius of copper electrode	r_c	4.50×10^{-4} m
Inner radius of steel electrode	r_{si}	4.65×10^{-4} m
Outer radius of steel electrode	r_{so}	6.35×10^{-4} m
Total length of copper	L_c	1.682 m
Total length of steel	L_s	0.165 m
Effective length of capacitor	L_{ca}	0.197 m
Permittivity of free space	ϵ_o	8.854 pF/m
Relative permittivity of PTFE	ϵ_r	2.1

can determine the impedance magnitude and phase in real-time [44] [45]. The device can be programmed to sample the impedance from frequencies as low as 0.56 Hz to 349 kHz. For obvious reasons, real-time analysis is impossible at such low frequencies, but critical impedance information may exist at lower frequencies.

2.4.1 Measurement and Excitation Circuit

To begin, the device functions by generating a PWM voltage excitation signal V_{Exc}, that is converted into a current I_{Exc} using the operational amplifier stages shown in Figure 2.4.

$$I_{Exc} = \frac{V_{Exc}}{R_{Ref_1}} \tag{2.9}$$

The current through the tissue's impedance will result in voltage across the tissue V_{Res}. Considering the operational amplifiers having sufficiently large input impedance, the entirety of the current will flow through the load and pass through the reference resistor R_{Ref_2}, which can be used to quantify the excitation voltage V'_{Exc} as,

$$V'_{Exc} = I_{Exc} \times R_{Ref_2} \tag{2.10}$$

As noted in [43], while the current is known from the initial conversion stage, signal degradation can occur due to a decrease in output impedance at higher frequencies. Thus, where one would normally estimate the unknown impedance through (2.1) as,

$$Z(\omega) = \frac{V_{Res}}{I_{Exc}} \tag{2.11}$$

can be adjusted to use measurable quantities. The response voltage V_{Res} across the
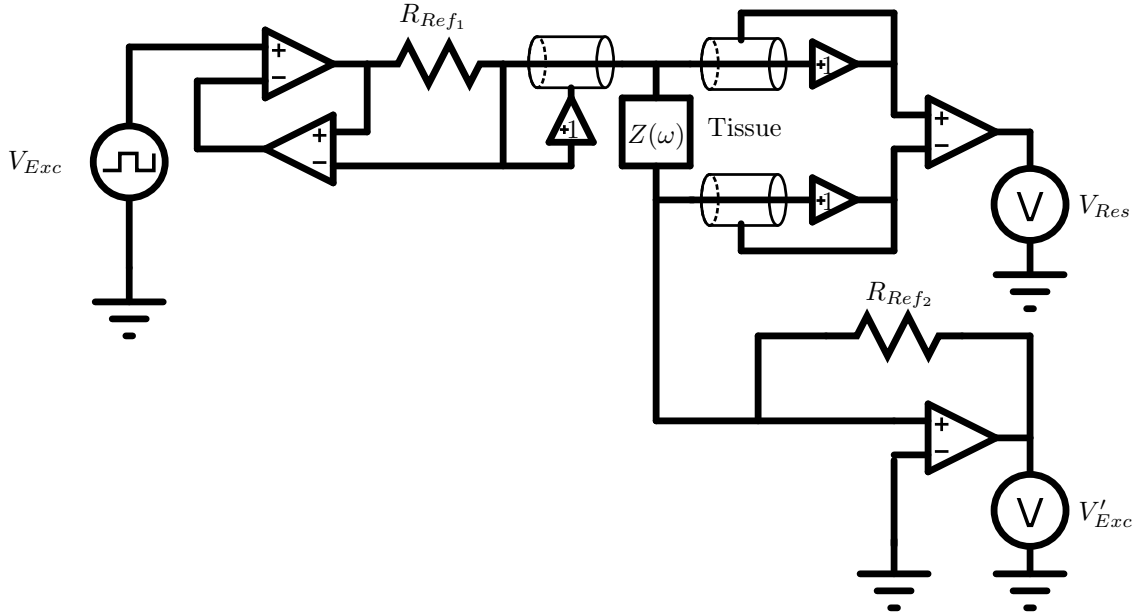
Figure 2.4: The circuit diagram of the Quadra electric impedance device, redrawn from [43]. The primary objective of the device is to measure the unknown impedance $Z(\omega)$. This is accomplished by comparing the response voltage V_{Res} across the load and the measured excitation V'_{Exc}.

unknown impedance $Z(\omega)$ is measured along with V'_{Exc}.

$$Z(\omega) = \frac{V_{Res}}{V'_{Exc}} \times R_{Ref_2} \tag{2.12}$$

2.5 Experimental Validation

Once the prototype was built and integrated with the excitation and measurement electronics, a series of experiments were conducted to measure the electric impedance of different tissue samples. The objective is to show that the obtained impedance data among the same type of tissue is similar and can be differentiated from other tissues. To this end, an assortment of tissues were prepared and measured, as shown in Table 2.2, including gelatin, agar, bovine liver/kidney/muscle, poultry liver, testicles, ovaries and fat. The following subsections detail the categories and specifics of the

Table 2.2: Tissue Samples Collected

Tissue	No. of Samples	Impedance Figure
Canine & Feline Testes	22	Appendix A.1
Canine & Feline Ovaries	22	Appendix A.2
Fat	18	Appendix A.3
Poultry Liver	22	Appendix A.4
Bovine Liver	22	Appendix A.5
Bovine Kidney	22	Appendix A.6
Bovine Muscle	22	Appendix A.7
Agar (Blue)	18	Appendix A.8
Agar (Yellow 1)	14	Appendix A.9
Agar (Yellow 2)	16	Appendix A.10
Gelatin (Original)	16	Appendix A.11
Gelatin (Green)	16	Appendix A.12
Gelatin (Red)	16	Appendix A.13

tissue samples, followed by the measurement procedure.

2.5.1 Experiment Setup

All samples were placed on an aluminium tray, grounded to the Quadra. The excitation signal voltage was set to 4.2V. The electrode embedded needle was inserted approximately 5-10 mm into the tissue sample. While inserted in the tissue the electric impedance was measured. At a single frequency, the impedance magnitude and phase were measured 10 times and averaged to account for noise in a single measurement. Unless otherwise stated, the experiments in this thesis measure the impedance at the following frequencies in Hz:

$$\mathbf{f} = \begin{bmatrix} 10.42 & 20.83 & 31.25 & 100 & 114.58 & 300 & 322.92 & 700 & \ldots \\ 1100 & 1700 & 2300 & 3100 & 11000 & 17000 & 23000 & 31000 & \ldots \\ 43000 & 61000 & 89000 & 127000 & 179000 & 251000 & 349000 & & \end{bmatrix} \quad (2.13)$$

The data was collected with approval from Ontario Tech Biosafety Committee, adhering to the procedures in handling tissue and sanitation of the equipment.

2.5.2 Gel-Based Phantoms

Powdered porcine gelatin and agar-agar (agar) were used to make gel-based phantoms. By adding salt in differing concentrations, the conductivity of the phantom could be altered in a repeatable and controllable fashion. To ensure variability in the data, multiple batches were made separately for each phantom, where each batch yielded multiple samples. Three types of gelatin were created using the following recipes:

- **Gelatin (Original)** a ratio of 6.7 grams porcine gelatin powder in 80 mL deionized water;

- **Gelatin (Green)** a ratio of 6.7 grams porcine gelatin powder with 2.0 grams of ionized salt diluted in 80 mL deionized water, tinted green with food colouring;

- **Gelatin (Red)** a ratio of 6.7 grams porcine gelatin powder with 5.0 grams of ionized salt diluted in 80 mL deionized water, tinted red with food colouring;

Agar was used to create a additional types of phantom tissue, with the following recipes:

- **Agar (Yellow 1)** a ratio of 0.7 grams agar powder with 1.0 gram of ionized salt diluted in 80 mL deionized water, tinted green with yellow colouring;

- **Agar (Yellow 2)** a ratio of 0.7 grams agar powder in 80 mL deionized water, tinted yellow with food colouring;

- **Agar (Blue)** a ratio of 0.7 grams agar powder with 0.5 grams of ionized salt diluted in 80 mL deionized water, tinted blue with food colouring;

The samples were stored in a refrigerator for a minimum of 4 hours, such that they would firm-up and set. The samples were removed from the fridge and measured quickly, at an approximate internal temperature of $14 - 18°C$.

Figure 2.5: The gelatin and agar samples were prepared using their corresponding recipes. Pictured here are Gelatin (Original), Gelatin (Red), Gelatin (Green), Agar (Blue), and Agar (Yellow 2).

2.5.3 Ex-Vivo Tissue

An assortment of meat from the grocery store was also measured. In this manuscript bovine liver, kidney and muscle are measured, along with poultry liver. All of the meats were trimmed of excess fat and connective tissue where applicable. Each of the tissues were segmented into 22 samples.

The lobes of the kidney samples were severed and then cut in half to expose their cross section. The kidney lobe was probed in the renal cortex across all samples, see Figure 2.6.

The bovine muscle was cubed into 2 cm samples. The probe was inserted into the tissue, parallel with the direction of the muscle fibres. Strands of fat in the samples were avoided. The samples were recorded at room temperature.

Figure 2.6: Preparation of the bovine kidney samples. The kidney was sectioned into 22 pieces and placed on an aluminium tray. The needle was inserted into the same location across the other samples. The other ex-vivo tissue samples received similar preparation.

2.5.4 Freshly Excised Tissue

Testicle and ovary samples were procured and measured following surgical removal by a local veterinarian clinic during their scheduled laparoscopic spay and neuters. Fat tissue surrounding the ovary was also sampled when it was possible. The tissues were collected from canine and feline patients that varied in age and breed, see Appendix C for a detailed list. The samples were sampled with urgency, less then five minutes from excision, with one exception as noted in the entry of Appendix C. The samples were also recorded at room temperature.

Figure 2.7: Pictured left are two sample ovaries: (top) German Shepard Mix - 6 months, (bottom) Golden Doodle - 7 months. Pictured right are two testicle samples: (top) Husky Mix - 12 months, (bottom) Yorkshire Terrier - 8 months.

2.6 Experimental Data & Observations

All of the tissue samples were measured using the EIS needle prototype. The measurements for each sample are compiled in Appendix A and Appendix B. For a cursory comparison, the average impedance magnitude is listed in Table 2.5. For a high-level comparison, the magnitude and phase for each tissue were averaged and are plotted in Figure 2.8. The results clearly show that the different tissues exhibit distinct electric impedance spectra.

The data of the tissues is relatively consistent across samples of the same tissue. A general trend seen across the samples is the difference in the variation of the data at the extremes of the frequency ranged measured: the data at higher frequencies was more consistent and was more broad at lower frequencies, especially in the freshly excised tissues. This is reflected in the standard deviation of the samples at the respective frequencies, see Table 2.5. A possible cause for this difference in variation may stem from the dielectric dispersions of the tissue. Coined by Schwan, the α, β and γ dispersion regions refer loosely to the low, RF and GHz of frequency bands respectively [46]. The exact frequencies are disputed in the literature, see [46] [47] and [48], but in general the ranges are 1 Hz - several kHz for the α dispersion, 1kHz to several MHz for the β dispersion, and upwards of 1 GHz for the γ dispersion. The frequency band measured line-up with the ranges for the α and β dispersion regions.

The increase in impedance at the lower end of the spectrum may also be heavily influenced by the capacitance as the electrodes become polarised. The impedance matches that of a capacitor in series with the circuit: infinite impedance as the frequency approaches zero. The findings in [33] also found greater influence of electrode polarisation at low frequencies. However, as the measured frequencies in these experiments did not explore this region, it is difficult to conclude exact behaviour. The phase decreases further as frequency is lessened, but does not appear to approach the $-90°$ phase shift seen in an ideal capacitor.

There are a few comparisons that can be made to the work by Kalvøy et al. who analysed the impedance data for different tissues of a living pig, including fat, muscle and liver [33]. The experiments in this thesis do not include porcine samples (excluding gelatin), but there is some benefit to a comparison. Notably, Kalvøy observed the impedance across a similar range of frequencies. Their results show a much greater phase shift at lower frequencies than seen in this data, and by extension, an order of magnitude greater in the impedance magnitude at lower frequencies. Nevertheless, despite the differences in the absolute values, Kalvøy observed different impedance spectra for different tissues, as seen in these results. They claimed the phase angle

between 20 and 300 kHz showed sufficient differences that it could be used for tissue characterisation [33].

Noteworthy features can be seen across the different tissues. At higher frequencies, fat was observed to have consistently high impedance relative to the other tissues samples. At lower frequencies, bovine liver has significantly higher impedance than the other tissues, perhaps making this a defining feature for this type of tissue. The spectrum of the gelatin samples reinforce the expected results; with the increased concentration in salt, the lower the magnitude of the impedance. In other words, the additional salt ions make the samples conduct better. The freshly excised tissue data-set is limited in size, therefore broad claims regarding the effects of breed, animal body weight and age can not be made definitively. General observations are made in Figures 2.9 and 2.10.

A few samples of abnormal tissue were recorded from some of the freshly excised tissue, see Figure 2.11 and Table 2.3. The limited number of samples can not decide universal features, but some observations can be made. As shown in [26], where renal cancer and normal tissue specimens were measured, differences exist in the electric impedance but are subtle. The authors in [26], recommend that the magnitude of the impedance at 1 MHz be used as the key characteristic in discriminating between normal and cancer tissues. The findings from these experiments seem to corroborate the idea of using higher frequency impedance values for tissue discrimination, as the impedance appears to be most distinct and consistent across all of the tissues investigated. That being said, at a macro level, the impedance is noticeably different at lower frequencies as well for categories of tissue. There appear to be distinct groups of tissue types, shown in Figure 2.8, where the gel-based phantoms are very different from the ex-vivo and excised tissues. In the paper by Zhang et al. they showed that a frequency of 1465 Hz resulted in the most unique impedance across their samples of healthy and cancerous skin cells, favouring neither high or low frequencies [49]. To conclude, it is seen that there is no universal solution when using electric impedance to distinguish between different types of tissue and classify malignancy against healthy tissue. Depending
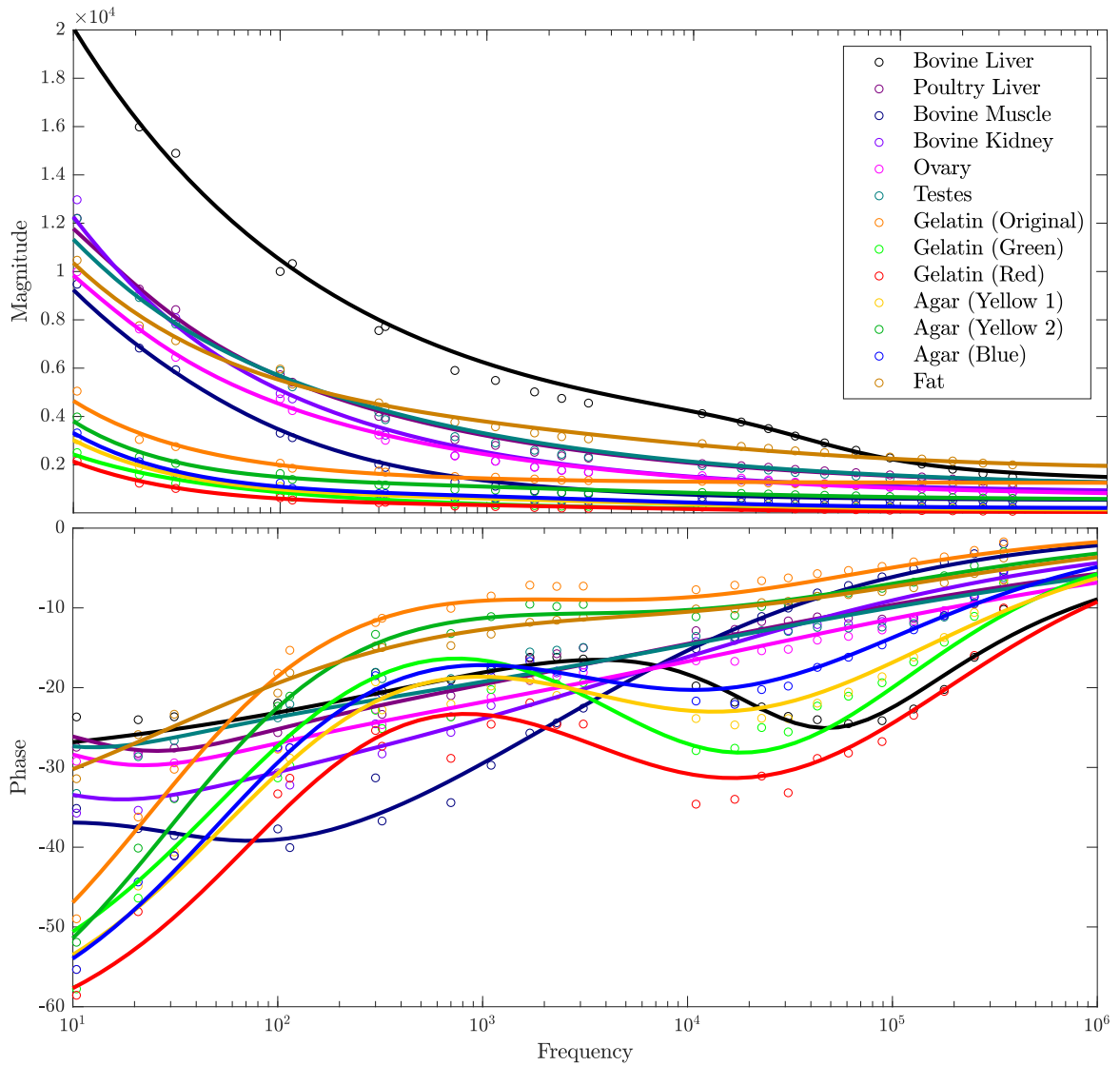
Figure 2.8: The average magnitude and phase spectra for all tissue samples. For clarity, a trendline is included for each tissue, interpolating the values between the measured frequencies. The spectra prove that the electric impedance of the tissues can be different, and supports the notion that electric impedance could be used for tissue classification.
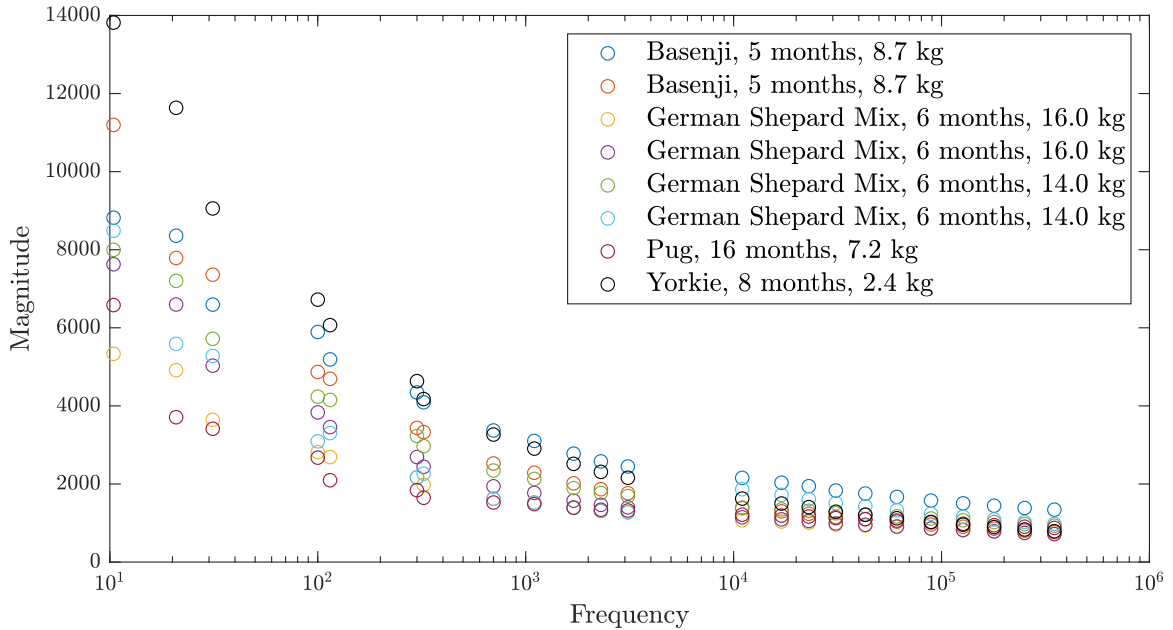
Figure 2.9: A comparison of the impedance magnitude of ovaries for different canine breeds. At the higher frequencies the impedance of the samples is relatively consistent. There does not appear to be any distinct correlation between the left and right ovaries of the same donor, nor across breeds, age or body weight.
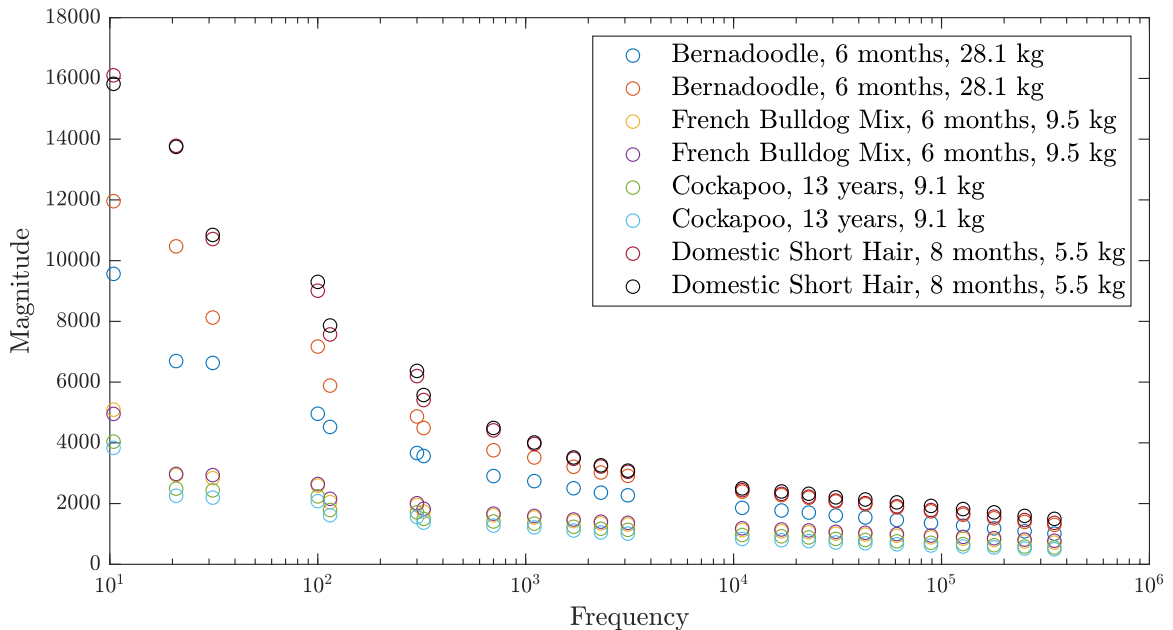
Figure 2.10: A comparison of the impedance magnitude of testes for three canine breeds and a feline sample. Notably, the left and right testes of the same donor share similar impedance across the spectrum, but differ when compared to other pairs at lower frequencies. With this limited data set, there does not appear to be any distinct correlation between age or body weight.

on the tissue one may find differences in impedance across the frequency spectrum. Thus, the upcoming chapters in this thesis will further develop the idea of using electric impedance to classify an assortment of tissue in a general manner; where the methods may be adapted for classifying a specific tissue malignancy.
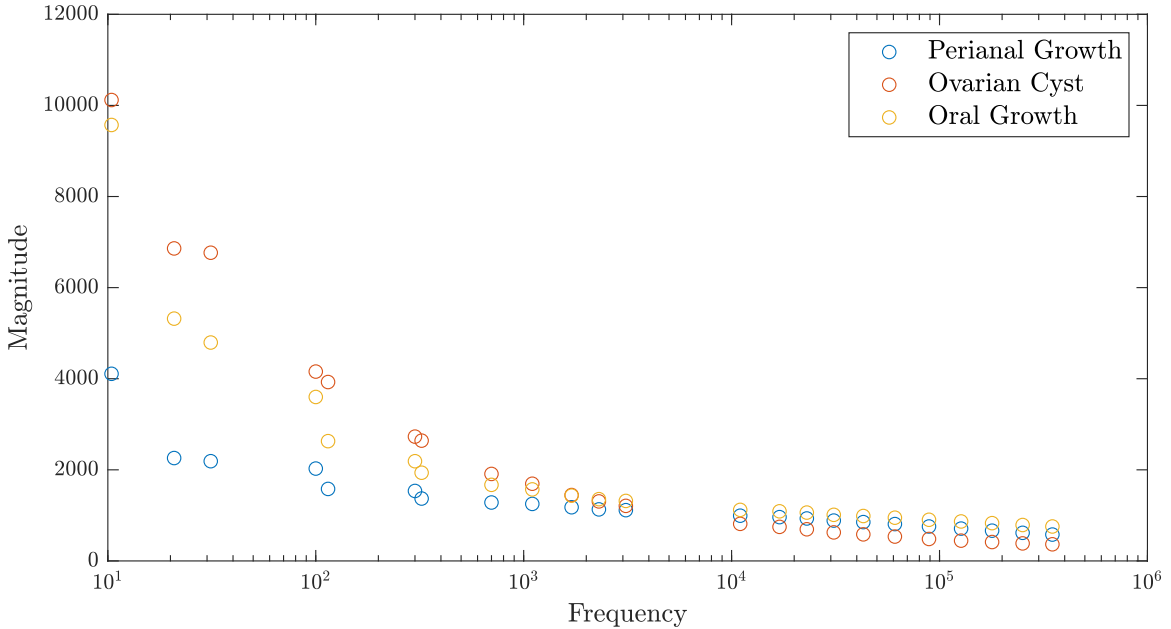
Figure 2.11: A comparison of the impedance magnitude for three types of abnormal tissue.

Table 2.3: Impedance Magnitude at 4 Frequencies for Abnormal Tissue Samples

Tissue	10.4 Hz	300 Hz	3.1 kHz	349 kHz
Perianal Growth	4108	1536	1146	578
Ovarian Cyst	10118	27293	12091	1231
Oral Growth	10467	4564	3074	365

Based on these results, it can be concluded that the prototype needle and system are capable of measuring the electric impedance of tissues, and that the impedance data could be used in tissue classification. The following chapter of this manuscript will explore how the collected impedance data can be fit to an equivalent circuit model, which may aid in the classification process.

Table 2.4: Average Value & Standard Deviation of the Impedance Magnitude at 4 Frequencies for All Tissue Samples (See Appendix B)

Tissue	10.4 Hz	300 Hz	3.1 kHz	349 kHz
Bovine Liver	20859 ± 3450	7556 ± 1129	4554 ± 735	1497 ± 211
Poultry Liver	12208 ± 1579	4004 ± 308	2275 ± 244	1231 ± 108
Bovine Muscle	9475 ± 1575	2022 ± 342	791 ± 264	491 ± 189
Bovine Kidney	12971 ± 1793	3386 ± 314	1691 ± 256	854 ± 76
Ovary	9987 ± 2825	3237 ± 842	1688 ± 419	864 ± 220
Testes	12193 ± 9755	4185 ± 2640	2323 ± 1240	1108 ± 503
Gelatin (Original)	5048 ± 1635	1741 ± 175	1348 ± 114	1060 ± 72
Gelatin (Green)	2501 ± 704	566 ± 79	278 ± 93	140 ± 45
Gelatin (Red)	2158 ± 834	434 ± 149	198 ± 85	77 ± 19
Agar (Yellow 1)	3036 ± 743	698 ± 98	391 ± 51	205 ± 81
Agar (Yellow 2)	3979 ± 718	1174 ± 182	840 ± 158	609 ± 139
Agar (Blue)	3317 ± 798	804 ± 141	480 ± 95	253 ± 40
Fat	10467 ± 3388	4564 ± 1698	3074 ± 1188	1997 ± 876

Table 2.5: Average Value & Standard Deviation of the Impedance Phase at 4 Frequencies for All Tissue Samples (See Appendix B)

Tissue	10.4 Hz	300 Hz	3.1 kHz	349 kHz
Bovine Liver	-23.7 ± 2.9	-18.1 ± 2.1	-16.4 ± 1.5	-10.2 ± 1.2
Poultry Liver	-27.5 ± 1.4	-20.5 ± 1.5	-15 ± 1.7	-6.4 ± 1
Bovine Muscle	-35.1 ± 1.7	-31.3 ± 2.9	-22.6 ± 2.9	-2 ± 0.4
Bovine Kidney	-35.7 ± 2.3	-24.5 ± 2.5	-17.2 ± 1.1	-5.7 ± 1.1
Ovary	-29.2 ± 6.4	-22.7 ± 3.5	-18.1 ± 2.9	-5.3 ± 0.8
Testes	-33.3 ± 8.8	-18.1 ± 5.6	-15 ± 4.3	-6.2 ± 1.5
Gelatin (Original)	-49 ± 4.7	-11.8 ± 2.8	-7.3 ± 0.7	-1.7 ± 0.5
Gelatin (Green)	-57.8 ± 3.5	-22.8 ± 5.2	-19.4 ± 2.5	-6.9 ± 1.6
Gelatin (Red)	-58.6 ± 4.4	-25.4 ± 4.5	-24.6 ± 4.6	-10 ± 2.4
Agar (Yellow 1)	-55.3 ± 3.6	-19.3 ± 2	-20.6 ± 2.4	-6.5 ± 0.7
Agar (Yellow 2)	-51.9 ± 4.3	-13.3 ± 1.5	-9.6 ± 1.3	-3 ± 0.4
Agar (Blue)	-55.3 ± 3.4	-18.5 ± 2	-17.5 ± 1.2	-5.4 ± 0.4
Fat	-31.4 ± 11	-14.8 ± 1.9	-11.2 ± 2.4	-3.7 ± 0.6

Chapter 3

Fitting Electric Impedance Data to an Equivalent Circuit Model

3.1 Introduction to the Equivalent Circuit Model

In some cases when working with electric impedance spectra, it is beneficial to fit the data to an equivalent circuit model. The model is comprised of electric circuit elements that effectively recreate the impedance at any frequency. Concerning biological tissue itself, several models have been proposed that relate the electric impedance spectra to an equivalent circuit of passive components. These models typically consist of resistive elements in combination with pseudo-capacitive elements [35] [50] , see Figure 3.3.

One of the earliest attempts to characterise the behaviour of electrolytes was done by Warburg [51] [52] in 1899. Traditionally, the Warburg element is considered to have -10 dB/decade magnitude and a constant $45°$ phase shift, see Figure 3.3(a). The Warburg element has still been used as part of more complicated models, and can be approximated by the series combination of a resistor and capacitor in parallel (R||C) [53]. In 1925 Fricke and Morse presented the equivalent model shown in Figure 3.3(b) to characterise the electric response of blood [54]. This model has been used in several publications for classification of tissues [55] [56]. In the 1940's, Kenneth Cole and Robert Cole published their landmark paper, which built upon the work of Debye [57], and led to the use of the Cole-Cole model in plotting the real and imaginary components of the electric impedance. Kenneth Cole's paper paved the way for the single dispersion model with a constant phase element, which has been one of the most popular models in EIS to date, see Figure 3.3(c) [35] [58]. This model includes the constant phase element (CPE) to account for non-ideal capacitive behaviour.

The CPE evolved out of the need for better fit to the impedance of real data. It was well observed that the change in impedance with frequency resembled that of a capacitor, but it did not mimic the behaviour perfectly. The impedance of this
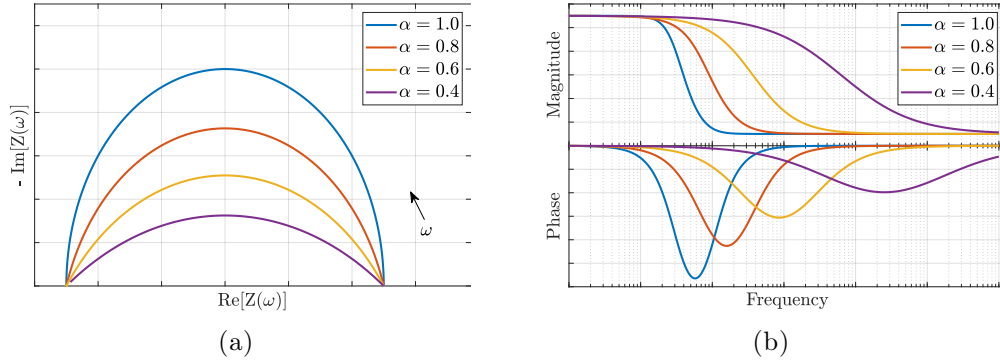
Figure 3.1: The impedance plots of the single dispersion model, see Figure 3.3(c), to illustrate the effect of changing the value of the dispersion coefficient α.

element is similar to that of capacitor [59],

$$Z_{CPE} = \frac{1}{C(s)^\alpha} \tag{3.1}$$

where C is the admittance constant [60], $s = j\omega$, with $j = \sqrt{-1}$ and ω as the frequency of the excitation signal. The exponent ($0 \leq \alpha \leq 1$) is referred to as the dispersion coefficient [61]. An example of the CPE in a model is provided in Figure 3.1. Should $\alpha = 1$, the CPE behaves like an ordinary capacitor.

A couple of years later, Randles introduced an equivalent circuit, which includes the Warburg impedance in series with the resistor in the parallel branch, see Figure 3.3(d) [62] [63]. Since then, Cole's work has been expanded to encompass multiple dispersions by introducing an additional R||C stage shown in Figure 3.3(f) [58]. Interestingly, the double-dispersion Cole model can also be developed from Randles' model, if one considers the double layer capacitance, shown as the CPE in Figure 3.3(d), to have negligible impact on the impedance and approximate the Warburg impedance as a series of R||C stages [53], one would also arrive at model shown in Figure 3.3(e).

More advanced models have evolved in the recent literature, such as the model proposed by Yun et al. [26], which accounts for the double layer, as well as the effects of insulating coatings. While these advanced models are more realistic, one should make informed in the development of their circuit model. If certain parameter elements of

32

the model are unknown, this increases the computational cost, as the optimisation method that fits the model to the impedance data will have to attempt to solve for this additional unknown. One should consider if the additional circuit elements are critical to fit the data; if a simpler model exists, and there is a negligible amount of improvement in the fit, it may be better to forgo the added complexity. This is especially important when considering the application to haptic feedback. Ideally, the tissue will be classified within real time. The computation time to fit the circuit model increases with more unknowns.

The equivalent circuit models have varying levels of accuracy in representing the impedance spectrum for a given tissue. Different models may be better suited for a given type of tissue [64]. The single dispersion Cole model has often been used to characterise the electric impedance of an assortment of organs [65] as well as fruit [66]. The extended version, the double-dispersion Cole model, can be used to accurately represent the impedance over a larger frequency range or for more complex materials [64] [65] [67].

The remainder of this manuscript utilises the double-dispersion Cole model, see Figure 3.2. The model has been known to capture the resistive and pseudo-capacitive behaviour of biological tissues. Furthermore, it has shown to fit tissue impedance well over a wide range of frequency [64] and the additional number of parameters in the model, compared to the more simple models, potentially yield more markers to use when classifying tissue.

The impedance of the double-dispersion Cole model is,

$$Z(\omega) = R_\infty + \frac{R_1}{R_1 C_1 s^{\alpha_1} + 1} + \frac{R_2}{R_2 C_2 s^{\alpha_2} + 1} \tag{3.2}$$

The capacitive behaviour of the tissue is represented by the constant phase elements (CPE), with C_1 and C_2.

In this thesis, the resistive nature of the tissue is represented by resistors R_∞, R_1, R_2,

where R_∞ represents the magnitude of the impedance as $\omega \to \infty$, R_1 (in combination with the other resistive elements) ensures the high magnitude impedance as $\omega \to 0$, and R_2 aids in the positioning of the cutoff frequencies.

The impedance in (3.2) can then be rewritten as,

$$\mathrm{Re}\left(Z\right) - j\,\mathrm{Im}\left(Z\right) = (z_1 + z_2) - j(z_3 + z_4) \tag{3.3}$$

and the phase and magnitude are given as follows,

$$|Z(\omega)| = \sqrt{(z_1 + z_2)^2 + (z_3 + z_4)^2} \tag{3.4}$$

$$\angle Z(\omega) = \frac{180°}{\pi}\arctan\left(\frac{z_3 + z_4}{z_1 + z_2}\right) \tag{3.5}$$

where z_1 to z_4 are defined as,

$$z_1 = \frac{R_\infty + R_1(R_1 C_1 e^{\alpha_2 \ln(w)} \cos\left(\alpha_2 \frac{\pi}{2}\right) + 1)}{\left(R_1 C_1 e^{\alpha_2 \ln(w)} \cos\left(\alpha_2 \frac{\pi}{2}\right) + 1\right)^2 + R_1^2 C_1^2 e^{(\alpha_2 \ln(w))^2} \sin(\alpha_2 \frac{\pi}{2})^2} \tag{3.6}$$

$$z_2 = \frac{R_2\left(R_2 C_2 e^{a_3 \ln(w)} \cos\left(a_3 \frac{\pi}{2}\right) + 1\right)}{\left(R_2 C_2 e^{a_3 \ln(w)} \cos\left(a_3 \frac{\pi}{2}\right) + 1\right)^2 + R_2^2 C_2^2 e^{(a_3 \ln(w))^2} \sin\left(a_3 \frac{\pi}{2}\right)^2} \tag{3.7}$$

$$z_3 = \frac{R_1^2 C_1 e^{\alpha_1 \ln(w)} \sin\left(\alpha_1 \frac{\pi}{2}\right)}{\left(R_1 C_1 e^{\alpha_1 \ln(w)} \cos\left(\alpha_1 \frac{\pi}{2}\right) + 1\right)^2 + R_1^2 C_1^2 e^{(\alpha_1 \ln(w))^2} \sin\left(\alpha_1 \frac{\pi}{2}\right)^2} \tag{3.8}$$

$$z_4 = \frac{R_2^2 C_2 e^{\alpha_2 \ln(w)} \sin\left(\alpha_2 \frac{\pi}{2}\right)}{\left(R_2 C_2 e^{\alpha_2 \ln(w)} \cos\left(\alpha_2 \frac{\pi}{2}\right) + 1\right)^2 + R_2^2 C_2^2 e^{(\alpha_2 \ln(w))^2} \sin\left(\alpha_2 \frac{\pi}{2}\right)^2} \tag{3.9}$$

Let $\mathbf{p} \in \mathbb{R}^+$ be the vector containing the 7 unknown model parameters that form the
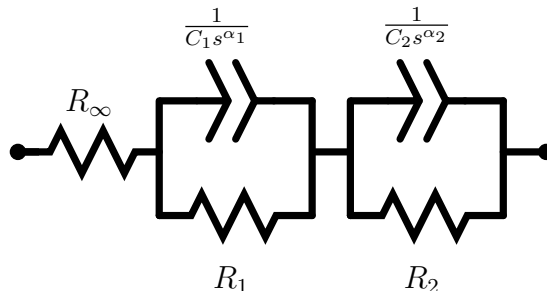
Figure 3.2: The double-dispersion Cole model, commonly used to fit bioimpedance spectra. The model consists of resistors and constant phase elements (CPE).

double-dispersion Cole model,

$$\mathbf{p} = [R_\infty, \quad R_1, \quad R_2, \quad C_1, \quad C_2, \quad \alpha_1, \quad \alpha_2] \tag{3.10}$$

The goal is, for a given measured impedance spectrum, to find the parameter values that would result in similar calculated impedance from (3.2) to (3.5). Thus, one needs an optimisation method that determines these parameter values such that the calculated impedance matches the measured impedance at various frequencies.

3.2 Optimisation to Derive Circuit Parameters

There have been attempts to fit the electric impedance data to a generalised model comprised of equivalent circuit elements [58]. In the simple models, the equivalent parameters quantify the conductivity and permeability of the tissue [68] [69], resulting in easily identifiable metrics. In the more complicated circuit models, it still provides a smaller number of parameters that describe a wide impedance spectrum. To fit the electric impedance spectra data to a model, many optimisation algorithms have been applied in the literature; the deterministic methods include the trust-region-reflective algorithm [58], Levenberg-Marquardt [70], Nelder–Mead [71], Newton-Raphson (Gauss-Newton) [72], among others. To overcome the issue of local minima traps, some researchers have explored stochastic methods, including particle filter, simulated annealing and evolution [73]. Regardless of the method, one can de-
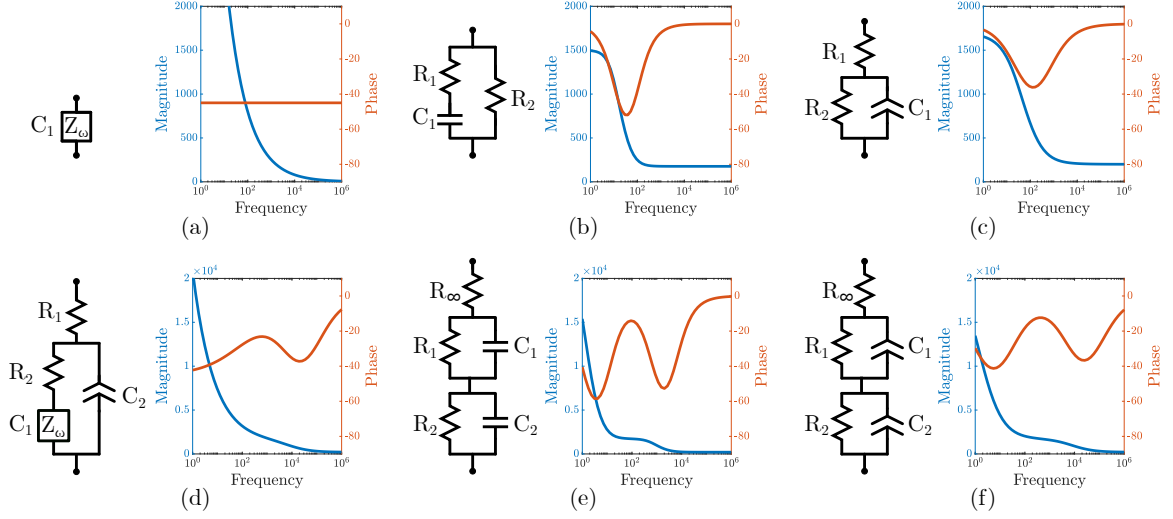
Figure 3.3: Equivalent circuit models used in part to represent bioimpedance of tissue alongside an example of their respective impedance spectra. (a) The Warburg model, (b) the Fricke-Morse model, (c) single dispersion Cole model with constant phase element $\alpha = 0.75$, (d) Randles' model, (e) double-dispersion Cole model with ideal capacitors $\alpha = 1.00$, (f) Double-dispersion Cole model with constant phase elements $\alpha = 0.75$. The impedance spectra is dependent on the parameter values; for models (a-c) $R_1 = 200\,\Omega$, $R_2 = 1500\,\Omega$, $C_1 = 5 \times 10^{-5}$ F, $C_2 = 1 \times 10^{-6}$ F, For models (d-f) $R_\infty = 200\,\Omega$, $R_1 = 20000\,\Omega$, $R_2 = 1500\,\Omega$, $C_1 = 5 \times 10^{-5}$ F, $C_2 = 1 \times 10^{-6}$ F.

termine parameter values for a given equivalent circuit model that would best yield similar electric impedance to that measured in the tissue. In the following subsections, the Newton-Raphson method and a multi-objective approach are introduced, and detail how the parameters for the double-dispersion Cole model are determined.

3.2.1 Newton-Raphson Optimisation Approach

If the impedance is measured at n frequencies, then equations (3.4) and (3.5) both yield $n \times 1$ column vectors. These column vectors are concatenated into a $2n \times 1$ vector to form the estimated impedance vector $\hat{\mathbf{z}} \in \mathbb{R}^{2n \times 1}$. To elaborate, the first n elements of the vector are the magnitude of the impedance from (3.4) and the elements $n + 1$ to $2n$ are the phase of the impedance from (3.5), such that $\mathbf{z} = [|Z(\omega_1)|, |Z(\omega_2)|, \cdots \angle Z(\omega_{n-1}), \angle Z(\omega_n)]^\top$. Let the actual measured impedance magnitude and phase be $\mathbf{z} \in \mathbb{R}^{2n \times 1}$, in the same form.

Let $\mathbf{p} = [R_\infty, R_1, R_2, C_1, C_2, \alpha_1, \alpha_2]$ be the unknown parameters that comprise the

equivalent circuit. The method proposed here simply finds a set of parameters $\mathbf{p}$ that results in a close approximation of the measured impedance at frequencies $\boldsymbol{\omega} \in \mathbb{R}^{n \times 1}$; where the difference in the calculated impedance $\hat{\mathbf{z}}$ and the measured values $\mathbf{z}$ is minimised. These circuit parameters in $\mathbf{p}$ do not necessarily constitute the conductivity or permittivity of the tissue, as others have found [24], since different combinations of parameters are feasible solutions.

The optimisation algorithm selected to perform this was the Newton-Raphson (Gauss-Newton) method [74]. The cost function is defined as the least square error between the measured impedance and calculated impedance at all frequencies,

$$E = \frac{1}{2}(\hat{\mathbf{z}} - \mathbf{z})^{\top}(\hat{\mathbf{z}} - \mathbf{z}) \tag{3.11}$$

with the objective of minimising (3.11), one needs to find the set of parameters $\mathbf{p} \in \mathbb{R}^{m \times 1}$ such that this is achieved. To do this one differentiates (3.11) with respect to the parameters $\mathbf{p}$, and set it equal to zero,

$$\frac{\partial E}{\partial \mathbf{p}} = 0 \tag{3.12}$$

Expanding the above yields,

$$\frac{\partial E}{\partial \mathbf{p}} = \left(\frac{\partial \hat{\mathbf{z}}}{\partial \mathbf{p}}\right)^{\top}(\hat{\mathbf{z}} - \mathbf{z}) = 0 \tag{3.13}$$

and the term $\partial \hat{\mathbf{z}}/\partial \mathbf{p}$ is the Jacobian matrix $\mathbf{J} \in \mathbb{R}^{2n \times m}$ defined as,

$$\mathbf{J} = \begin{bmatrix} \frac{\partial \hat{\mathbf{z}}_{w_1}}{\partial R_{\infty}} & \frac{\partial \hat{\mathbf{z}}_{w_1}}{\partial R_1} & \frac{\partial \hat{\mathbf{z}}_{w_1}}{\partial R_2} & \frac{\partial \hat{\mathbf{z}}_{w_1}}{\partial C_1} & \frac{\partial \hat{\mathbf{z}}_{w_1}}{\partial C_2} & \frac{\partial \hat{\mathbf{z}}_{w_1}}{\partial \alpha_1} & \frac{\partial \hat{\mathbf{z}}_{w_1}}{\partial \alpha_2} \\ \frac{\partial \hat{\mathbf{z}}_{w_2}}{\partial R_{\infty}} & \frac{\partial \hat{\mathbf{z}}_{w_2}}{\partial R_1} & \frac{\partial \hat{\mathbf{z}}_{w_2}}{\partial R_2} & \frac{\partial \hat{\mathbf{z}}_{w_2}}{\partial C_1} & \frac{\partial \hat{\mathbf{z}}_{w_2}}{\partial C_2} & \frac{\partial \hat{\mathbf{z}}_{w_2}}{\partial \alpha_1} & \frac{\partial \hat{\mathbf{z}}_{w_2}}{\partial \alpha_2} \\ \vdots & \vdots & \vdots & \vdots & \vdots & \vdots & \vdots \\ \frac{\partial \hat{\mathbf{z}}_{w_{2n}}}{\partial R_{\infty}} & \frac{\partial \hat{\mathbf{z}}_{w_{2n}}}{\partial R_1} & \frac{\partial \hat{\mathbf{z}}_{w_{2n}}}{\partial R_2} & \frac{\partial \hat{\mathbf{z}}_{w_{2n}}}{\partial C_1} & \frac{\partial \hat{\mathbf{z}}_{w_{2n}}}{\partial C_2} & \frac{\partial \hat{\mathbf{z}}_{w_{2n}}}{\partial \alpha_1} & \frac{\partial \hat{\mathbf{z}}_{w_{2n}}}{\partial \alpha_2} \end{bmatrix} \tag{3.14}$$

While (3.14) can be determined explicitly, for computational efficiency the partial derivatives in the Jacobian can be approximated by determining how the impedance changes given a small finite step $\delta \to 0$ in a given parameter,

$$\frac{\partial \hat{\mathbf{z}}_{w_n}}{\partial \mathbf{p}_m} \approx \frac{\hat{\mathbf{z}}_{w_n}(\mathbf{p}_m + \delta) - \hat{\mathbf{z}}_{w_n}(\mathbf{p}_m)}{\delta} \tag{3.15}$$

Since the problem defined in (3.13) is non-linear, a Taylor series expansion at an arbitrary point $\mathbf{p}^i$ gives,

$$\frac{\partial E}{\partial \mathbf{p}} \approx \frac{\partial E}{\partial \mathbf{p}}(\mathbf{p}^i) + \frac{\partial^2 E}{\partial \mathbf{p}^2}(\mathbf{p}^i)\Delta \mathbf{p}^i \tag{3.16}$$

where $\partial^2 E/\partial \mathbf{p}^2$ is the Hessian matrix, which is approximated by [75],

$$\frac{\partial^2 E}{\partial \mathbf{p}^2} = \left[\frac{\partial \hat{\mathbf{z}}}{\partial \mathbf{p}}\right]^\top \left[\frac{\partial \hat{\mathbf{z}}}{\partial \mathbf{p}}\right] = \mathbf{J}^\top \mathbf{J} \tag{3.17}$$

Setting (3.16) to zero and solving for $\Delta \mathbf{p}$, the parameters are updated through a small change $\Delta \mathbf{p}^i$ dependent on the difference between the estimated $\hat{\mathbf{z}}$ and measured impedance $\mathbf{z}$,

$$\Delta \mathbf{p}^i = -[\mathbf{J}^\top \mathbf{J} + \lambda \mathbf{I}]^{-1}[\mathbf{J}]^\top [\hat{\mathbf{z}} - \mathbf{z}] \tag{3.18}$$

where $\lambda = 1 \times 10^{-8}$ and is used with an identity matrix $\mathbf{I} \in \mathbb{R}^{m \times m}$ to prevent a singular matrix that cannot be inverted.

Through the iterations, a small change is made to each of the parameters such that the error converges to a minimum. Through the ith iteration of the optimiser, the parameter updates are,

$$\mathbf{p}^{i+1} = \mathbf{p}^i + \kappa \, \mathbf{I} \, \Delta \mathbf{p}^i \tag{3.19}$$

where κ is vector of learning rates for the parameters, which intentionally slows the progress of the optimiser to gradually converge to the minimum value. This iterative
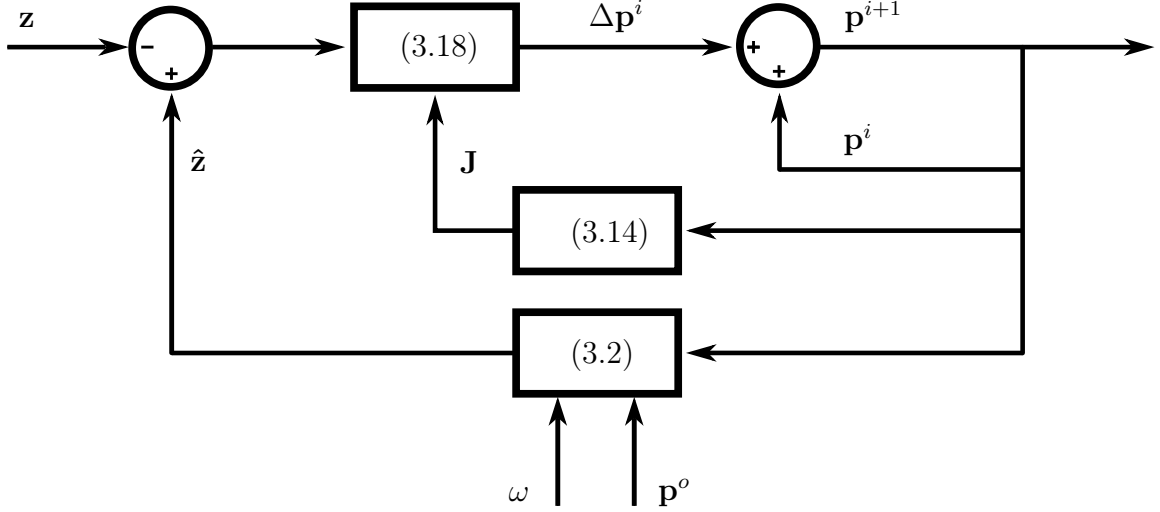
Figure 3.4: General flow diagram for the Newton-Raphson method to determine the set of parameters **p** to minimise the error between the measured and calculated impedance $(\mathbf{z} - \hat{\mathbf{z}})$. $\mathbf{p}^o$ is the initial guess for the parameter values.

approach is summarised in Figure 3.4.

Since this method is deterministic, the final solution is heavily dependent on the starting values of the optimiser $\mathbf{p}^o$. The initial values for the parameters are estimated by analysing the spectrum data of the measured impedance **z**. As seen in (3.2) as $\omega \to \infty$ the pseudo-capacitors will act like short circuits, thus one could assign $R_\infty = |Z(\omega = \infty)|$. At the other extreme, as $\omega \to 0$ the impedance can be taken as $R_\infty + R_1 + R_2 = |Z(\omega = 0)|$. However, the device used to measure the impedance is typically limited in the range of frequencies it can sample, thus one needs to consider the lowest and highest frequencies sampled: ω_1 and ω_n respectively [58]. Concerning the capacitance values C_1 and C_2, they play an important role in the location of the pole/zero pairs along the spectrum and should be selected with care.

Provided that Newton-Raphson converges to a set of parameters for the tissue under test, one can compare these set of parameters to a database to classify the tissue based on the similarities in the parameters. The following subsection introduces how this database is developed. Chapter 4 details how the data here will be used to aid classify the tissue.
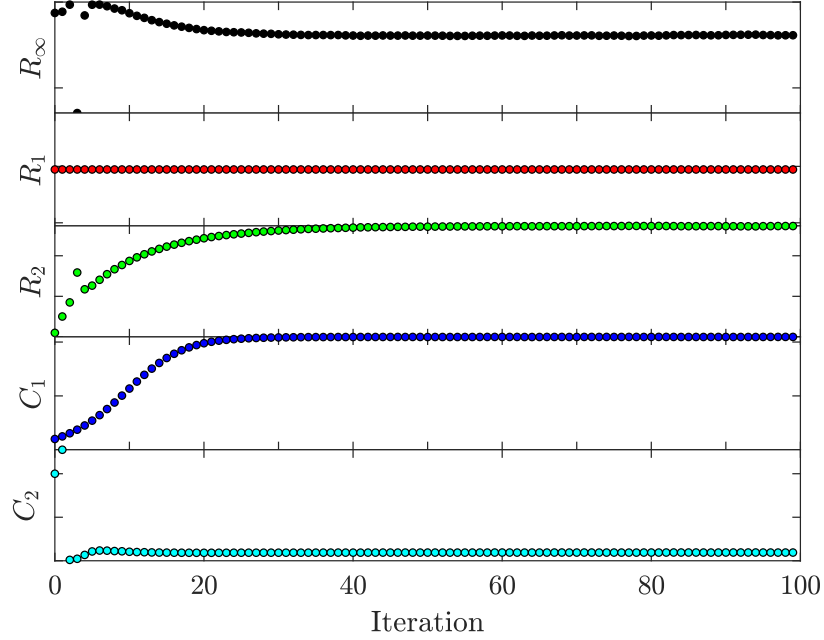
Figure 3.5: An example of how the parameters of the double-dispersion Cole model converge from the intial to final values during the Newton-Raphson method.

Developing the Parameter Database from Newton-Raphson

This method is used with the impedance data for all tissues as described in Section 2, and listed in Appendix B. As mentioned in the preceding section, the impedance magnitude and phase data for a tissue sample are concatenated. The optimiser will take in a starting set of parameters, provided by the user, and across iterations update these parameters such that when they are applied to the double-dispersion circuit, the model impedance should be similar to the measured impedance.

It was found that the optimiser struggled to converge when searching for all 7 parameters of the model. Thus, to simplify the problem the dispersion coefficients were fixed by the user. The dispersion coefficients were, as a default, selected to be $\alpha_1 = 0.4$ and $\alpha_2 = 0.9$, but were updated depending on the nature of the individual tissue impedance spectrum as appropriate. The initial parameter values were selected as,

$$\mathbf{p}^o = [\mathbf{z}_{(\omega_n)}, \quad 10^5 \times \mathbf{z}_{(\omega_1)}, \quad 10^2, \quad 5 \times 10^{-6}, \quad 2 \times 10^{-7}] \tag{3.20}$$

Table 3.1: Bounds of Circuit Parameters during Newton-Raphson Optimisation

Var.	Lower Bound	Upper Bound
R_∞	$0.50 \times \mathbf{p}_1^o$	$2.0 \times \mathbf{p}_1^o$
R_1	$10^{-2} \times \mathbf{p}_2^o$	$10^3 \times \mathbf{p}_2^o$
R_2	$10^{-2} \times \mathbf{p}_3^o$	$10^3 \times \mathbf{p}_3^o$
C_1	$10^{-2} \times \mathbf{p}_4^o$	$10^2 \times \mathbf{p}_4^o$
C_2	$10^{-2} \times \mathbf{p}_5^o$	$10^2 \times \mathbf{p}_5^o$

Table 3.2: Newton-Raphson Optimisation Stopping Criteria

	Criteria	Value
(a)	$i > i_{max}$	$i_{max} = 100$
(b)	$e_1 > \lvert \hat{\mathbf{z}}^i - \hat{\mathbf{z}}^{i-1} \rvert$	$e_1 = 5.0 \times 10^{-4}$
(c)	$\boldsymbol{e}_2 > \Delta\mathbf{p}$	$\boldsymbol{e}_2 = [10, \quad 50, \quad 50, \quad 10^{-7}, \quad 10^{-7}]^\top$
(d)	$e_3 > E^i$	$e_3 = 1.0 \times 10^{-2}$

where $\mathbf{z}_{(\omega_n)}$ is the magnitude of the impedance measured at the highest frequency, and $\mathbf{z}_{(\omega_1)}$ is the magnitude of the impedance measured at the lowest frequency. These initial parameter values were selected through empirical testing and observations in the impedance spectrum across different tissues. The bounds on these parameter values were determined based off the initial values, as seen in Table 3.1.

There are multiple stopping criteria that are checked through an iteration of the optimiser to determine if the parameters have converged to a solution. These stopping criteria, listed in Table 3.2, are:

- The maximum number of iterations are exceeded.

- Minimal absolute change in impedance at all frequencies across iterations.

- A minimal change in all parameters through an iteration.

- There is minimal error in an iteration at all data points from (3.11).

The parameters for all 246 tissue samples were determined using the Newton-Raphson method. An example of how the parameters converged to their final values can be seen in Figure 3.5. The fit impedance for each tissue type is provided in Figures 3.6(a) to 3.6(m).
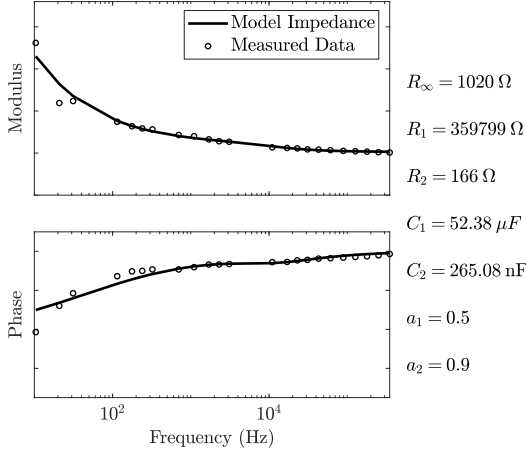
(a) Gelatin (Original)
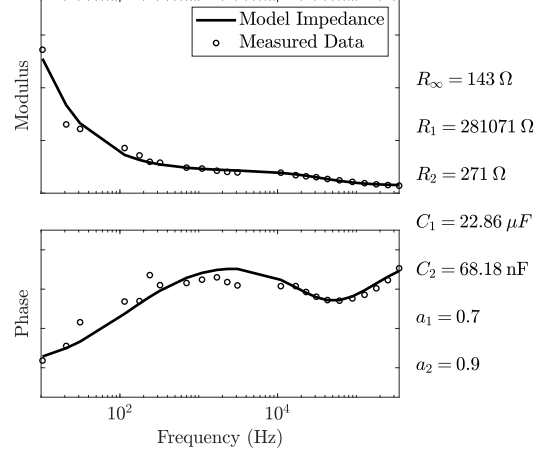
(b) Gelatin (Green)
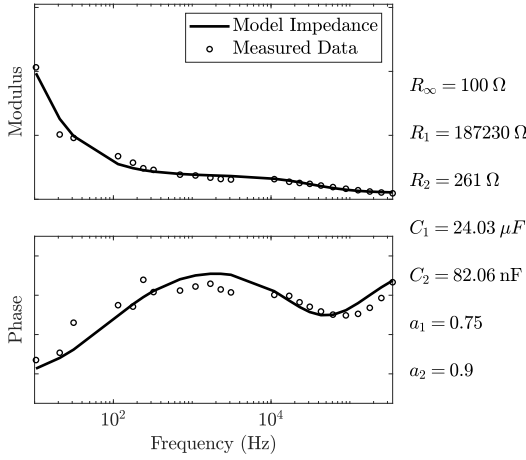
(c) Gelatin (Red)
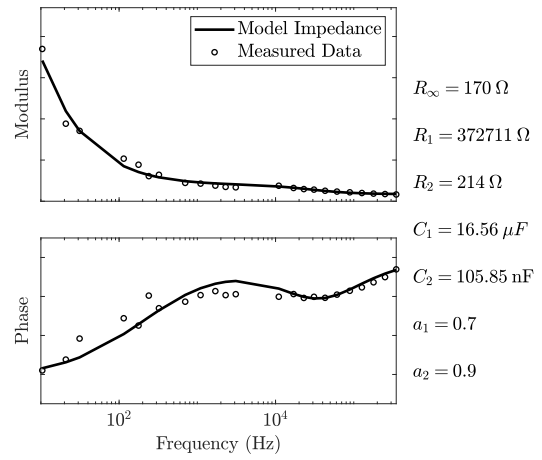
(d) Agar (Yellow 1)
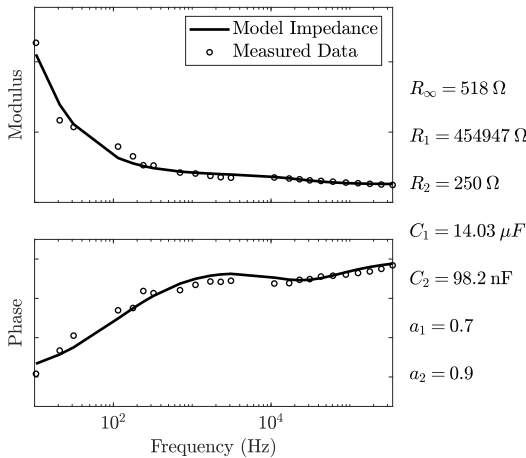
(e) Agar (Yellow 2)
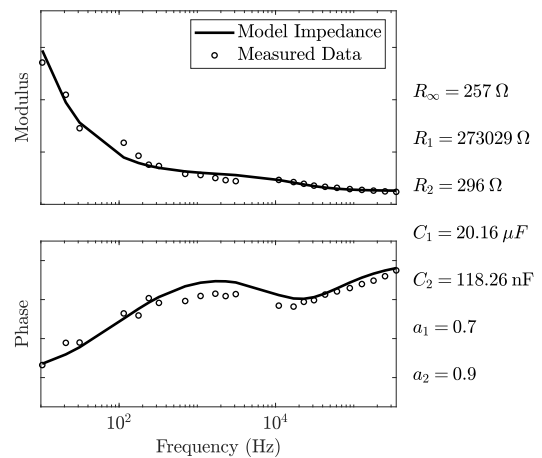
(f) Agar (Blue)
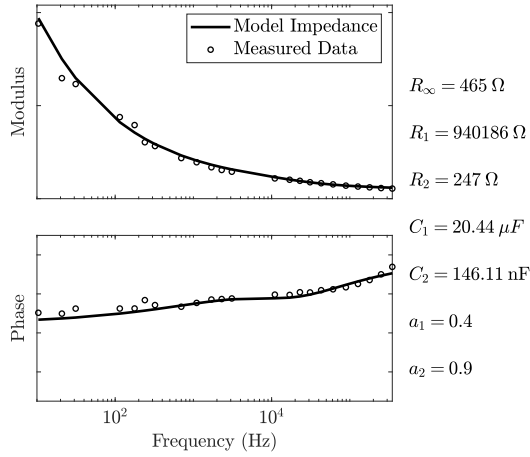
(g) Canine & Feline Ovary
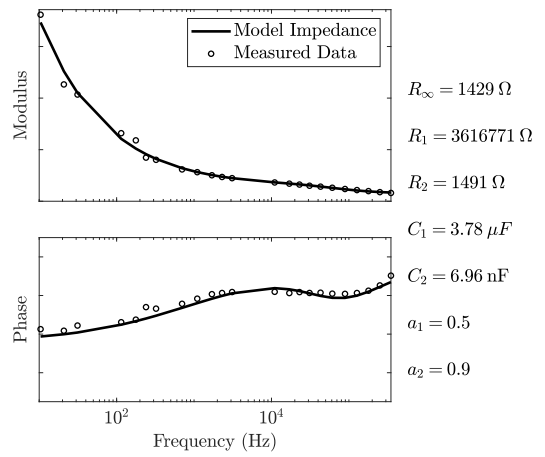
$R_\infty = 465\,\Omega$

$R_1 = 940186\,\Omega$

$R_2 = 247\,\Omega$

$C_1 = 20.44\,\mu F$

$C_2 = 146.11\,\text{nF}$

$a_1 = 0.4$

$a_2 = 0.9$

(h) Canine & Feline Testes

$R_\infty = 1429\,\Omega$

$R_1 = 3616771\,\Omega$

$R_2 = 1491\,\Omega$

$C_1 = 3.78\,\mu F$

$C_2 = 6.96\,\text{nF}$

$a_1 = 0.5$

$a_2 = 0.9$

(i) Bovine Kidney

$R_\infty = 764\,\Omega$

$R_1 = 1107237\,\Omega$

$R_2 = 417\,\Omega$

$C_1 = 18.04\,\mu F$

$C_2 = 17.95\,\text{nF}$

$a_1 = 0.4$

$a_2 = 0.9$

(j) Bovine Muscle

$R_\infty = 1112\,\Omega$

$R_1 = 1295019\,\Omega$

$R_2 = 3135\,\Omega$

$C_1 = 19.72\,\mu F$

$C_2 = 5\,\mu F$

$a_1 = 0.4$

$a_2 = 0.9$

(k) Bovine Liver

$R_\infty = 1225\,\Omega$

$R_1 = 1678162\,\Omega$

$R_2 = 2261\,\Omega$

$C_1 = 12.72\,\mu F$

$C_2 = 8.48\,\text{nF}$

$a_1 = 0.4$

$a_2 = 0.9$

(l) Poultry Liver

$R_\infty = 1274\,\Omega$

$R_1 = 1037790\,\Omega$

$R_2 = 636\,\Omega$

$C_1 = 20.29\,\mu F$

$C_2 = 14.22\,\text{nF}$

$a_1 = 0.4$

$a_2 = 0.9$

$R_\infty = 2276\,\Omega$

$R_1 = 1367962\,\Omega$

$R_2 = 869\,\Omega$

$C_1 = 4.56\,\mu F$

$C_2 = 21.97\,nF$

$a_1 = 0.7$

$a_2 = 0.9$

(m) Fat
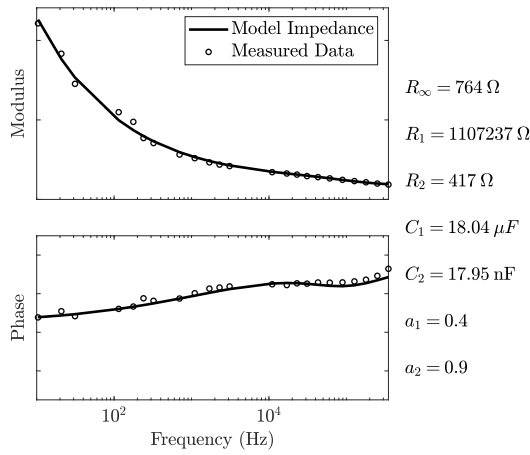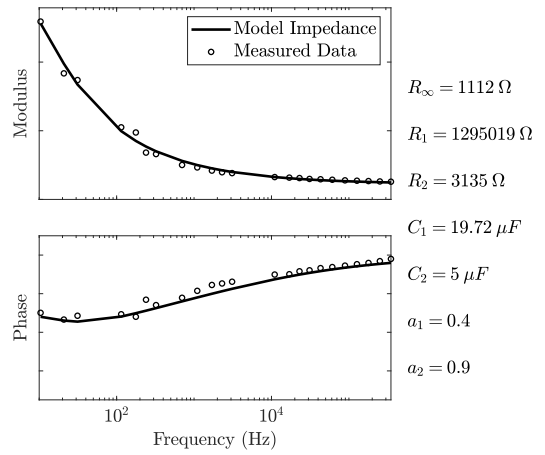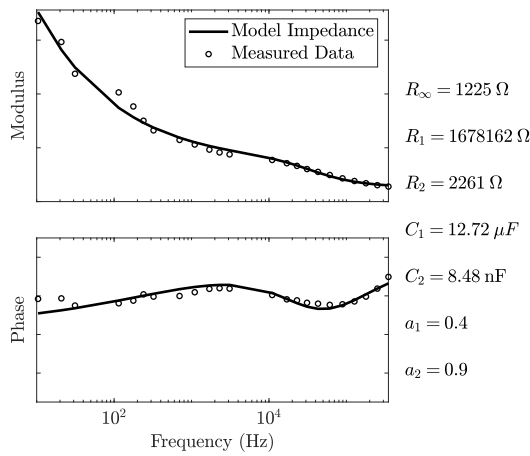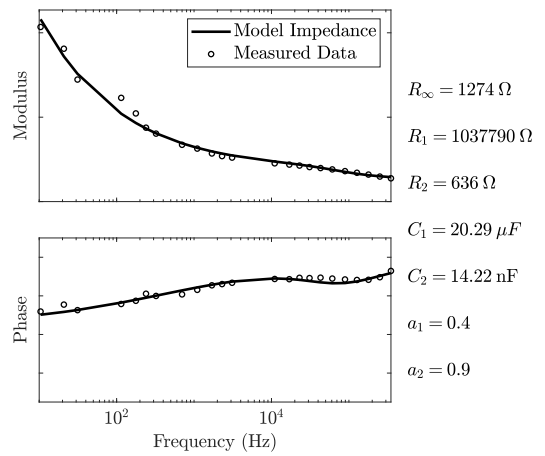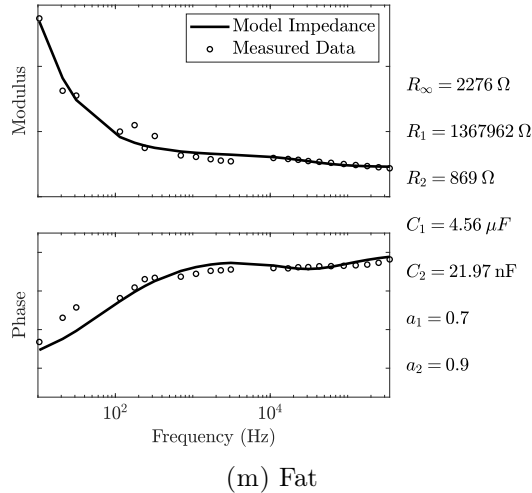
Figure 3.6: For each tissue the measured impedance for one sample and the estimated impedance using the equivalent model and the circuit parameters determined from the Newton-Raphson method.

The optimisation process generates a solution for each tissue sample. To understand the variation of the parameters across the samples for a tissue statistics are presented in Figure 3.7 and in Table 3.3. A few observations can be made from the data. First, for most tissues, the extracted parameters are consistent across the samples. This is beneficial, since the parameters with small deviation can mean that a new sample will likely also fall within the same range, increasing the chance that the parameter can be used as a recognisable feature in classification. Secondly, one can observe how unique a tissue is in relation to the others based on these parameters. Take Bovine Liver and Bovine Muscle for example; excluding outliers, the tissues do not have any overlap for parameters R_∞, R_1, C_1, C_2, but overlap does exist in R_2. Thus, if one were comparing these two tissues, it would be favourable to use the more distinct parameters than those that possibly share similar values. In contrast, consider the parameter values for Agar (Yellow 1) and Gelatin (Green), where significant overlap in the values exist in several parameters. This is likely the result of two issues: the tissues have relatively similar impedance spectra, and the general rule applied to the initial guess of the parameters. Third, the fit to the measured data is poor in some samples, again stemming in part from the initial guess, and how the parameters converge to the solution. This poor fit will lead to parameter values that lie outside those one

44

would expect from that tissue, based off previous samples. Lastly, expanding upon the previous, it is unlikely that this method will find the global minimum parameters that will generate the best fit to the impedance. Therefore there exist several more possible solutions that are equally viable that could generate the impedance, that are not being acknowledged in this method.

Evidently, it seen that there is promise in using the equivalent circuit parameters as classification features, but issues exist in the extraction method. The next section will move away from the rigidity imposed by the deterministic algorithm and explore an alternative stochastic approach, which may solve some of these issues.

Table 3.3: Model Parameter Statistics of Tissue Samples from Newton-Raphson

Statistics of R_∞ (Ω)				Statistics of R_1 (Ω)		
Tissue	**Mean**	**Std Dev**	**Median**	**Mean**	**Std Dev**	**Median**
Agar (Blue)	274	45	252	332920	81312	326761
Agar (Yellow 1)	200	27	198	305615	78012	304821
Agar (Yellow 2)	652	150	663	398022	75629	402735
Bovine Kidney	829	288	759	1297099	183505	1311092
Bovine Liver	1240	220	1198	2085875	353120	2025907
Bovine Muscle	357	192	317	948548	160389	998790
Poultry Liver	1205	257	1247	1221126	161145	1240585
Fat	2332	995	2265	1046703	348200	1125442
Gelatin (Green)	143	42	120	246778	74175	212159
Gelatin (Original)	1156	98	1138	501985	167236	490967
Gelatin (Red)	79	22	74	210960	86169	189726
Ovary	860	296	738	997724	289587	931547
Testes	1178	618	962	1220131	997890	944676

Statistics of R_2 (Ω)				Statistics of C_1 (F)		
Tissue	**Mean**	**Std Dev**	**Median**	**Mean**	**Std Dev**	**Median**
Agar (Blue)	314	72	301	1.86e-05	4.20e-06	1.87e-05
Agar (Yellow 1)	326	128	315	2.02e-05	4.63e-06	2.00e-05
Agar (Yellow 2)	326	75	309	1.72e-05	3.45e-06	1.66e-05
Bovine Kidney	4963	10326	478	1.56e-05	4.93e-06	1.53e-05
Bovine Liver	2539	1487	2176	1.02e-05	2.39e-06	1.04e-05
Bovine Muscle	4171	1937	4391	3.16e-05	7.06e-06	3.12e-05
Poultry Liver	775	488	650	1.69e-05	3.01e-06	1.69e-05
Fat	2131	1091	1961	8.03e-06	3.51e-06	6.63e-06
Gelatin (Green)	205	78	203	2.14e-05	5.10e-06	2.06e-05
Gelatin (Original)	11782	30877	673	2.39e-05	3.06e-05	6.02e-06
Gelatin (Red)	201	105	173	2.26e-05	6.91e-06	2.28e-05
Ovary	7026	20833	1060	2.51e-05	1.09e-05	2.07e-05
Testes	1101	1112	716	3.27e-05	2.50e-05	2.33e-05

Statistics of C_2 (F)			
	Mean	**Std Dev**	**Median**
Agar (Blue)	1.73e-07	3.08e-07	1.06e-07
Agar (Yellow 1)	1.00e-07	3.28e-08	9.96e-08
Agar (Yellow 2)	3.95e-07	5.69e-07	9.52e-08
Bovine Kidney	2.03e-06	1.99e-06	2.24e-06
Bovine Liver	1.47e-07	6.50e-07	7.77e-09
Bovine Muscle	3.15e-06	9.95e-07	3.13e-06
Poultry Liver	2.14e-06	2.21e-06	1.62e-06
Fat	1.83e-07	1.28e-07	1.48e-07
Gelatin (Green)	1.09e-07	3.74e-08	1.092e-07
Gelatin (Original)	1.76e-06	3.22e-06	6.445e-07
Gelatin (Red)	1.71e-07	9.80e-08	1.33e-07
Ovary	1.57e-06	1.62e-06	1.06e-06
Testes	7.45e-07	2.06e-06	7.30e-08
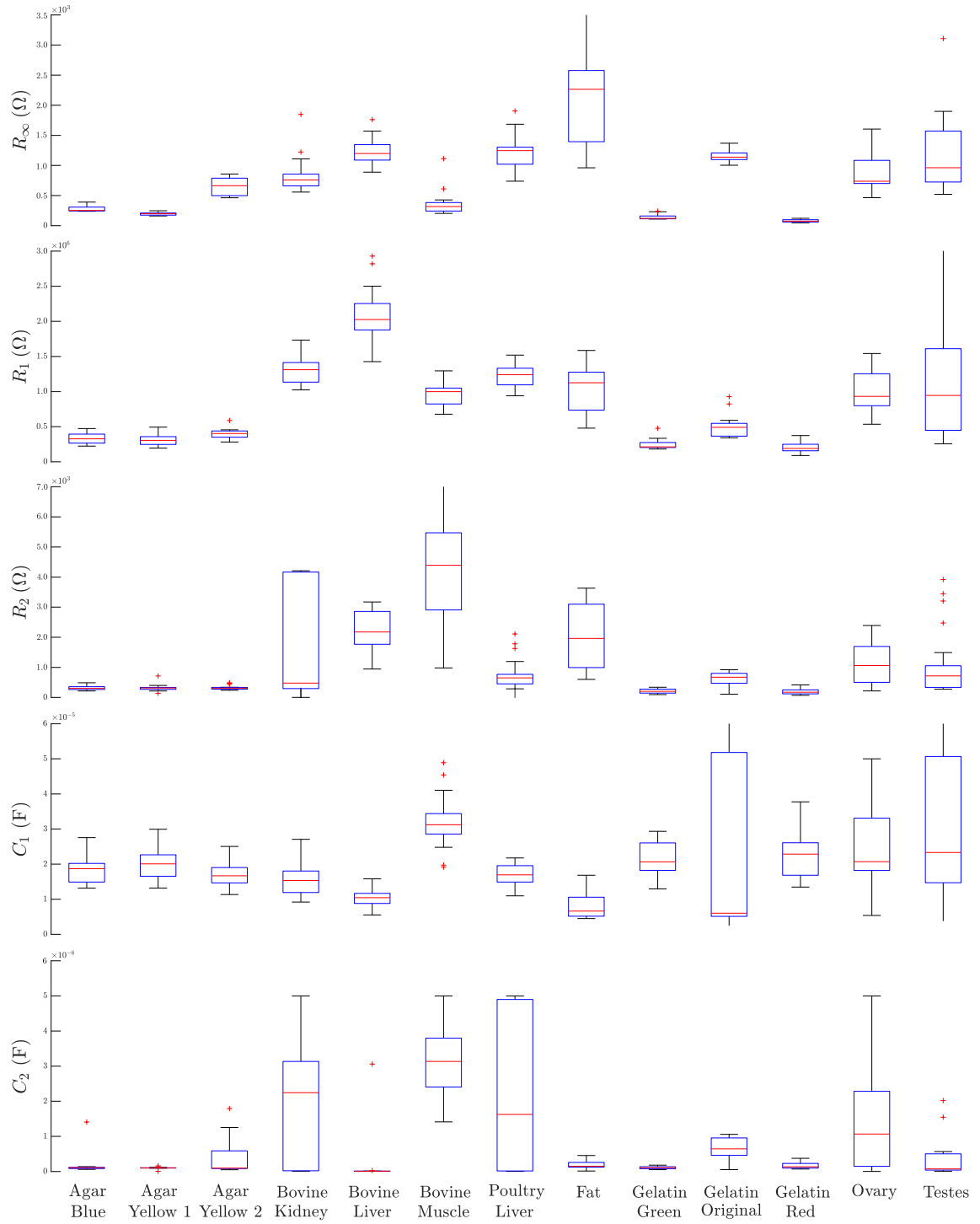
Figure 3.7: Boxplots that display the distribution of the circuit parameters for each of the tissues extracted using Newton-Raphson. The line within the box denotes the median value. The cross outside of the boxes denote outliers in the data. Reference Tables 3.3 for specific values.

3.2.2 Multi-objective Approach

Consider that the electric impedance of the sample tissue is measured at n frequencies. The impedance data is organised into $n \times 1$ column vectors, containing the measured impedance magnitude $\mathbf{z}_m$ and phase $\mathbf{z}_p$ separately. If the parameters of the circuit $\mathbf{p}$ were known, then equations (3.4) and (3.5) both form $n \times 1$ column vectors as well, and yield the estimated impedance magnitude $\hat{\mathbf{z}}_m$ and phase $\hat{\mathbf{z}}_p$ respectively.

There exists two desired tasks: to minimise the error in the estimated and measured magnitude $\hat{\mathbf{z}}_m - \mathbf{z}_m$, and phase $\hat{\mathbf{z}}_p - \mathbf{z}_p$, by only altering $\mathbf{p}$. This can be formed into a multi-objective problem as [76],

$$
\begin{aligned}
\textbf{Minimise:} \qquad & \mathbf{F}(\mathbf{p}) = (f_1(\mathbf{p}), f_2(\mathbf{p}))^T, \mathbf{p} \in \Omega \\
\textbf{Subject to:} \qquad & g_k(\mathbf{p}) \geq 0 \quad k = 1 \dots P \\
& h_l(\mathbf{p}) = 0 \quad l = 1 \dots Q
\end{aligned}
$$

where P and Q are the numbers of inequality and equality constraints respectively, Ω is the variable space for $\mathbf{p}$ as a candidate solution, and $\mathbf{F}$ houses the objective functions, where it is desired to minimise the square error,

$$
f_1 = \frac{1}{2} \left((\mathbf{z}_m - \hat{\mathbf{z}}_m)^\top (\mathbf{z}_m - \hat{\mathbf{z}}_m) \right) \tag{3.21}
$$

$$
f_2 = \frac{1}{2} \left((\mathbf{z}_p - \hat{\mathbf{z}}_p)^\top (\mathbf{z}_p - \hat{\mathbf{z}}_p) \right) \tag{3.22}
$$

This may seem unintuitive to decompose the impedance problem, but this enables the problem to include more objective functions in the future. Also, this enables multiple solutions can be found, which alleviates some of dependency on the initial guess of the parameters.

During optimisation with more than one objective, there is not a guaranteed global solution that minimises all objective functions. More often, there will be a set of solutions that are non-dominated, see Figure 3.9. The challenge that typically comes with finding the multi-objective solutions is that, as the number of objectives increase, the more likely the solutions are to become non-dominated, resulting in poor convergence or representation of solutions. Thus, this thesis includes the approach presented by Elarbi et al. [76] to prevent this from occurring.

The solution proposed in [76] is to define a set of evenly distributed reference points across the hyperplane of the search space [76]. These reference points are used to evaluate the convergence and diversity of nearby candidate solutions. The reference point set W is generated by,

$$W = \begin{pmatrix} m + v - 1 \\ v \end{pmatrix} \tag{3.23}$$

where m is the number of objective functions, and v is the number of divisions along the objective. As previously mentioned, the distance from the solution candidates to the reference points are determined as,

$$d_1(\mathbf{p}) = \frac{\left\| \tilde{f}(\mathbf{p})^T R_k \right\|}{\|R_k\|} \tag{3.24}$$

$$d_2(\mathbf{p}) = \left\| \tilde{f}(\mathbf{p}) - d_1(\mathbf{p}) \left(\frac{R_k}{\|R_k\|} \right) \right\| \tag{3.25}$$

with $\tilde{f}(\mathbf{p})$ being the normalised objective function. R_k is an M-dimensional direction vector [76].

The method selected to solve the multi-objective problem is the wildly popular Non-dominated Sorting Genetic Algorithm II (NSGA-II) [77], but with the additional consideration of reference point dominance (RPD) [76]. The method attempts to minimise both d_1 and d_2, which will ensure good convergence and diversity of the
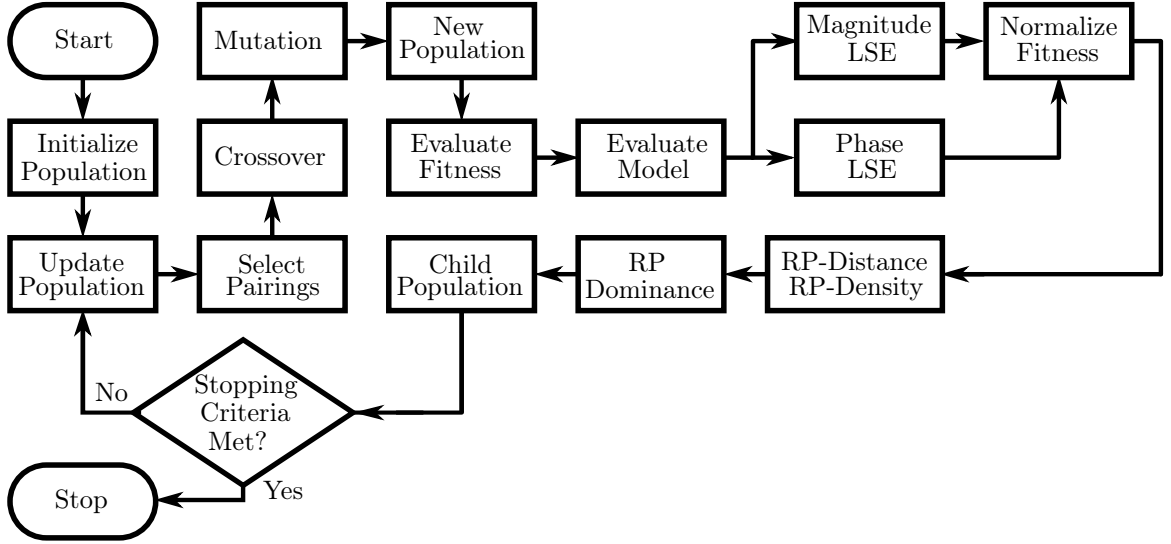
Figure 3.8: General flow diagram for the RPD-NSGA-II method method to determine the set of parameters that will fit the measured impedance data.

potential solutions respectively. The RPD-NSGA-II algorithm fundamentals are introduced here, but the reader is directed to the original publication [76] for further reading, where it is well documented. The flow diagram of the algorithm is presented in Figure 3.8. The process bears similarities to a traditional genetic algorithm.

Initialise Population: The population is comprised of individual members, where each population member represents the 7 parameters of the equivalent circuit model. The parameters are determined randomly between a set of boundary values determined by the programmer.

Crossover/Mutation: The population members are altered to explore the potential combinations of parameters. This is achieved using the fundamental transformations of a genetic algorithm: crossover and mutation. Crossover is performed first, where two parent population members $(\mathbf{p_{p1}}, \mathbf{p_{p2}})$ would be nominated and are used to create the two child members $(\mathbf{p_{c1}}, \mathbf{p_{c2}})$ using the following equations, using a random variable $0 \leq \mu_c \leq 1$ for each parameter and the user-defined crossover rate ζ_c [78] [79] [80] [81].

$$\mathbf{p_{c1}} = 0.5((1 - \beta)\mathbf{p_{p1}} + (1 + \beta)\mathbf{p_{p2}}) \tag{3.26}$$

$$\mathbf{p_{c2}} = 0.5((1 + \beta)\mathbf{p_{p1}} + (1 - \beta)\mathbf{p_{p2}}) \tag{3.27}$$

where β is determined by [78],

$$\beta = \begin{cases} (2\mu_c)^{1/(\zeta_c+1)} & \text{if } \mu_c \leq 0.5 \\ (2(1 - \mu_c))^{1/(\zeta_c+1)} & \text{if } \mu_c > 0.5 \end{cases} \tag{3.28}$$

The children then undergo the mutation stage using the following formulae for polynomial mutation [79]. Using a random variable $0 \leq \mu_m \leq 1$ for each parameter and the user-defined crossover rate ζ_m. If the random variable $\mu_m \leq 0.5$ then the update variable is [79],

$$\delta_l = (2\mu_m)^{(1/(\zeta_m+1))} - 1 \tag{3.29}$$

and the children are mutated using [79],

$$\mathbf{p_{c1}} = \mathbf{p_{c1}} + \delta_l(\mathbf{p_{c1}} - \mathbf{p}_{UB}) \tag{3.30}$$

$$\mathbf{p_{c2}} = \mathbf{p_{c2}} + \delta_l(\mathbf{p_{c2}} - \mathbf{p}_{UB}); \tag{3.31}$$

Alternatively, if the random variable is $\mu_m > 0.5$, the update variable becomes,

$$\delta_r = 1 - (2(1 - \mu_m))^{(1/(\zeta_m+1))} \tag{3.32}$$

and the children are mutated using,

$$\mathbf{p_{c1}} = \mathbf{p_{c1}} + \delta_r(\mathbf{p}_{LB} - \mathbf{p_{c1}}) \tag{3.33}$$

$$\mathbf{p_{c2}} = \mathbf{p_{c2}} + \delta_r(\mathbf{p}_{LB} - \mathbf{p_{c2}}) \tag{3.34}$$
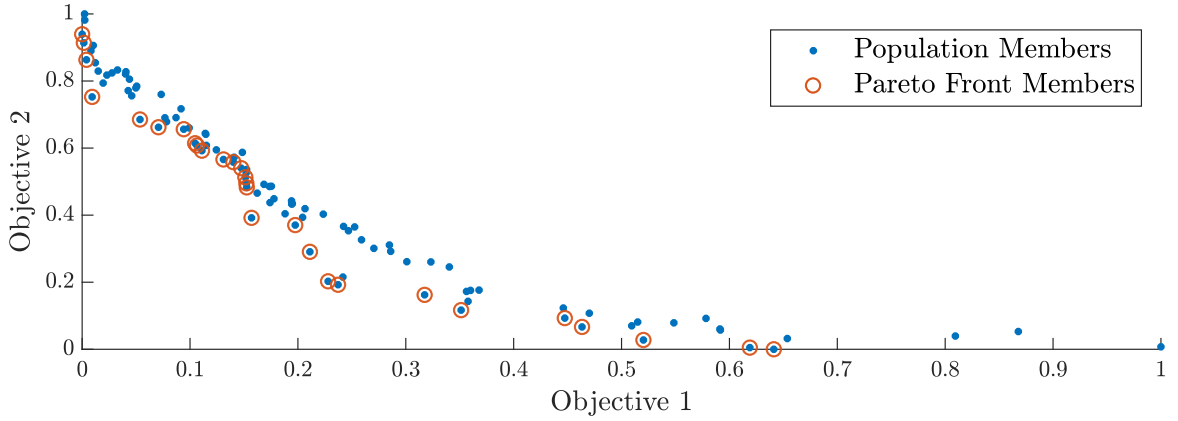
Figure 3.9: Normalised fitness values for the population members after 50 generations of the optimisation method. Encircled members constitute the non-dominated population, which are used to represent the final set of parameter combinations for the sample.

where $\mathbf{p}_{UB}$ and $\mathbf{p}_{LB}$ refer to the upper and lower bounds a parameter may take.

Evaluate Fitness: With the new population created each population member is tested to determine how well its combination of parameters will generate a similar impedance to that of the measured sample. One at a time, the parameters of a population member are used in the circuit model to determine the impedance at the frequencies the measured sample was taken at. From this, the estimated impedance magnitude and phase are compared to the measured sample using the least square error equations (3.21) and (3.22).

The maximum fitness value for each of the objective functions is then used to normalise the fitness values of the other population members, refer to Figure 3.9 where a value of zero on the horizontal axis would depict a best fit to the magnitude, and a value of zero on the vertical axis would depict a best fit to the phase.

RP-Dominance: With the fitness values normalised the RP-fronts can be determined using the Euclidean distance (3.24) and the normal distance (3.25). Using these distances, the non-RP dominated solutions can be found and the Pareto front determined. The child population is then constructed using the solutions in the Pareto front.

If the stopping criteria of the optimiser is met, then the process is complete. Other-

Table 3.4: Parameter Initial Value Bounds (top), and RPD-NSGA-II Optimiser Parameters (bottom)

Model Parameter	Lower Bound	Upper Bound
R_∞	1.0×10^0	2.0×10^3
R_1	1.0×10^5	2.0×10^7
R_2	1.0×10^0	2.0×10^3
C_1	1.0×10^{-9}	1.0×10^{-4}
C_2	1.0×10^{-9}	1.0×10^{-4}
α_1	0.30	1.0
α_2	0.30	1.0

Variable	Symbol	Value
Number of Objectives	m	2
Dimension of Problem	P	7
Population Size	N	25
Crossover Rate	p_c	20
Mutation Rate	p_m	20
Number of Divisions	v	20
Number of Generations		5000

wise, the process repeats. The stopping criteria, at a minimum, consists a maximum number of iterations but can also check the number of fitness function calls, change in the variables for convergence, or fitness level.

3.2.3   Optimisation Setup

This method is used with the impedance data for all tissues as described in Section 2. This optimisation method was allowed to run for 10000 generations, with 25 members in the population, to try and determine the 7 parameters of the double-dispersion Cole model. Since the optimiser is trying to minimise error among magnitude and phase separately, the number of objective functions, m, is 2. The number of divisions along the hyper-plane, v, is set as 20. The crossover and mutation rates are $\zeta_c = 20$ and $\zeta_m = 20$. The initial parent population is created randomly between the bounds as detailed in Table 3.4.

3.2.4   Optimisation Results

Provided in Figures 3.11(a) to 3.11(l) are examples of the tissues' impedance and the multiple solutions that fit the data. The fit curves in the figures show a high level of fit across the both the magnitude and phase. This showcases the success of the method, where solutions can be found that fit both objectives. Deviations exist in some examples, seen in Figure 3.11(i). This shows the possible variation that can occur from this approach, where a solution may have a better fit in one objective than another.

As the method generates a large volume of data, it is difficult to compare the results of all the tissues with clarity. For this reason, 4 tissues were selected to be compared in the boxplots of Figure 3.12, where 18 samples for each tissue are provided. Each box depicts the parameter data for 100 solutions. The data shows the variability that can occur within tissue through this optimisation process, as the combination of parameters the solutions may generate can vary extensively. Despite this, trends can be seen in the data. Most notably is what circuit parameters are most distinct across the different tissues. This supports the earlier observations in Figure 2.8 and Table 2.4, where the impedance magnitude at higher frequencies is the one of the more distinct features, which correlates to R_∞. However, across the possible solution combinations the spread of values leads to some overlap across the tissues. One could then look to the parameter a_1 where, for majority of the samples, the values are categorically different for each tissue. These results would suggest that this method could be used to develop the circuit model parameters and, in the case of these 4 tissues, one could use circuit parameters in classifying tissue.
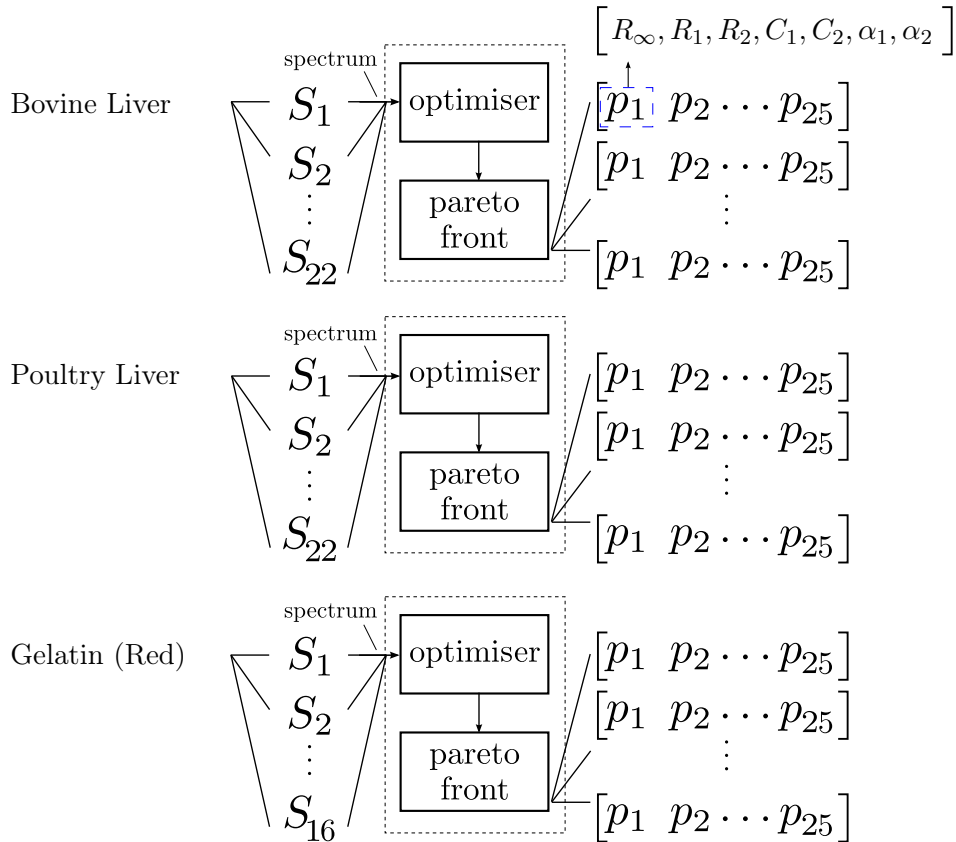
Figure 3.10: For a given tissue, all of the spectra samples are fed individually to the RPD-NSGA-II optimiser. This optimiser will generate the Pareto front of solutions that satisfy the objective functions. The 25 population members in this Pareto front are then extracted, where each population member contains the 7 model parameters. Refer to Table 3.4 and Table 2.2.
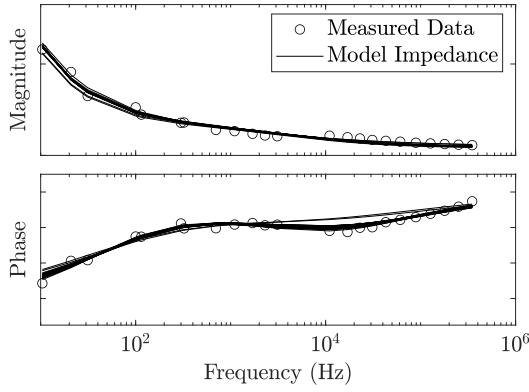
(a) Agar (Blue)
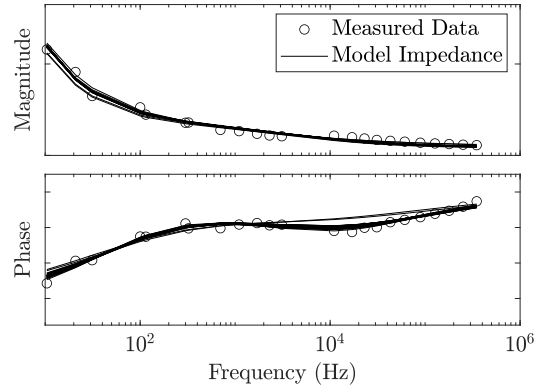
(b) Agar (Yellow 1)
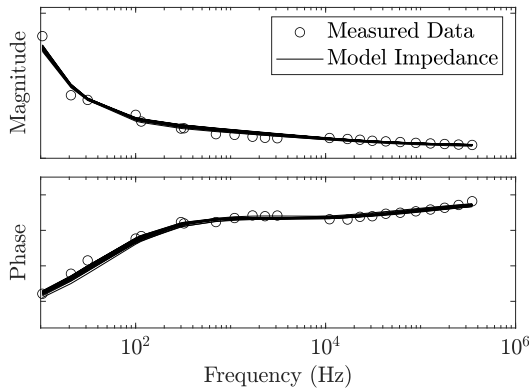
(c) Agar (Yellow 2)
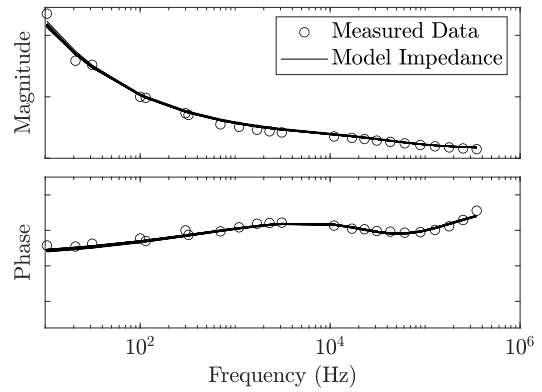
(d) Bovine Liver
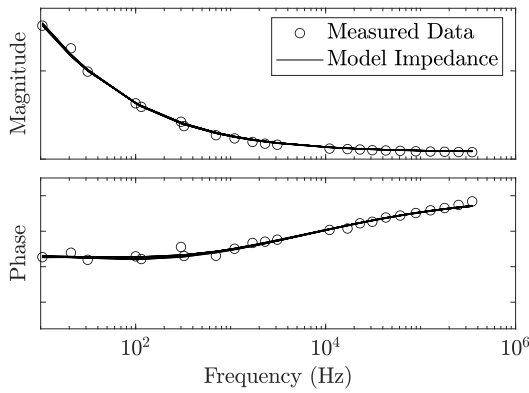
(e) Bovine Muscle

(f) Bovine Kidney

(g) Poultry Liver

(h) Gelatin (Original)

(i) Gelatin (Green)

(j) Gelatin (Red)

(k) Ovary

(l) Fat
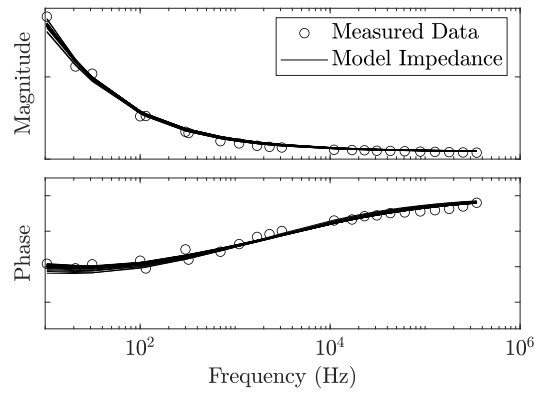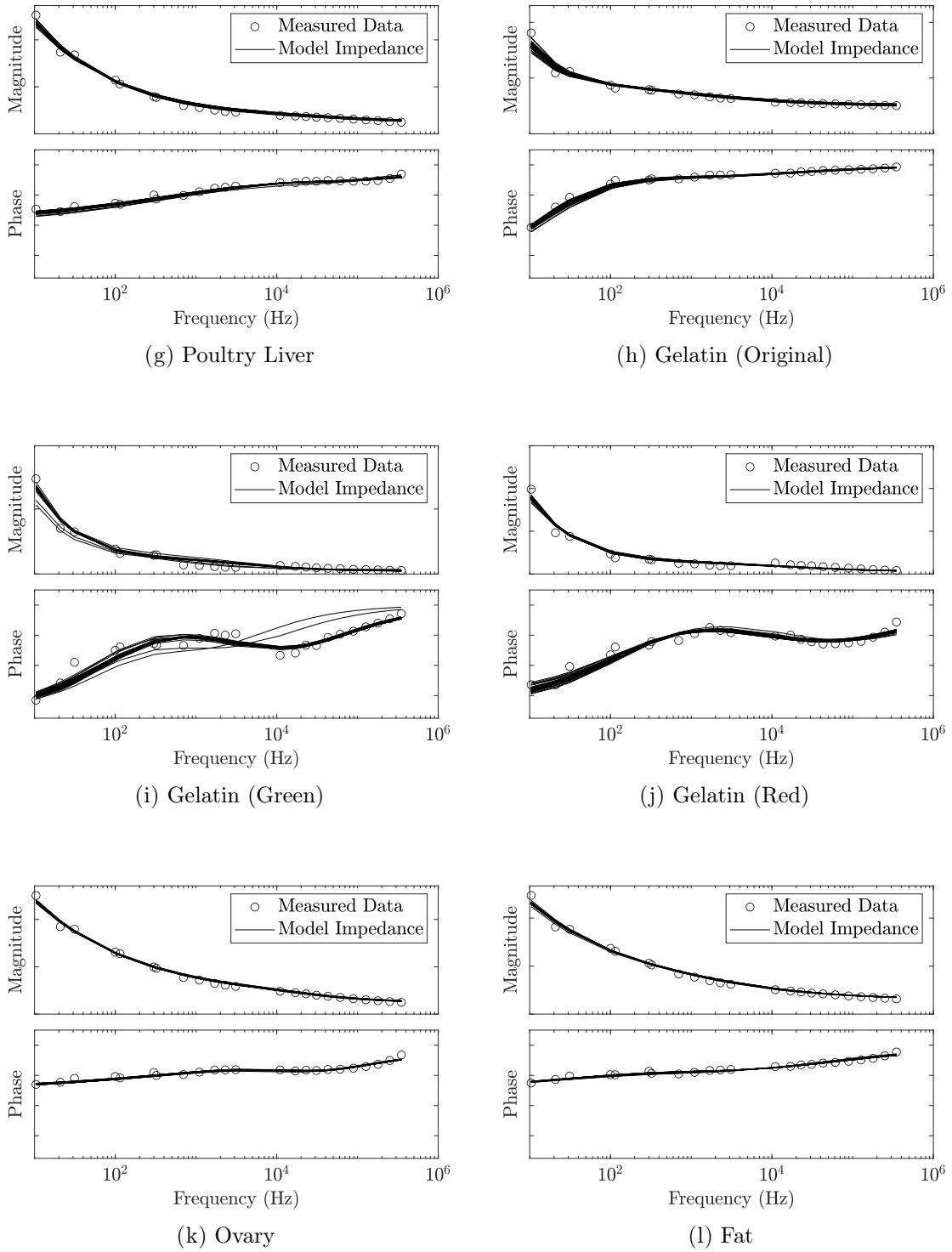
Figure 3.11: The fit solutions for the assorted tissues using the RPD-NSGA-II optimiser.
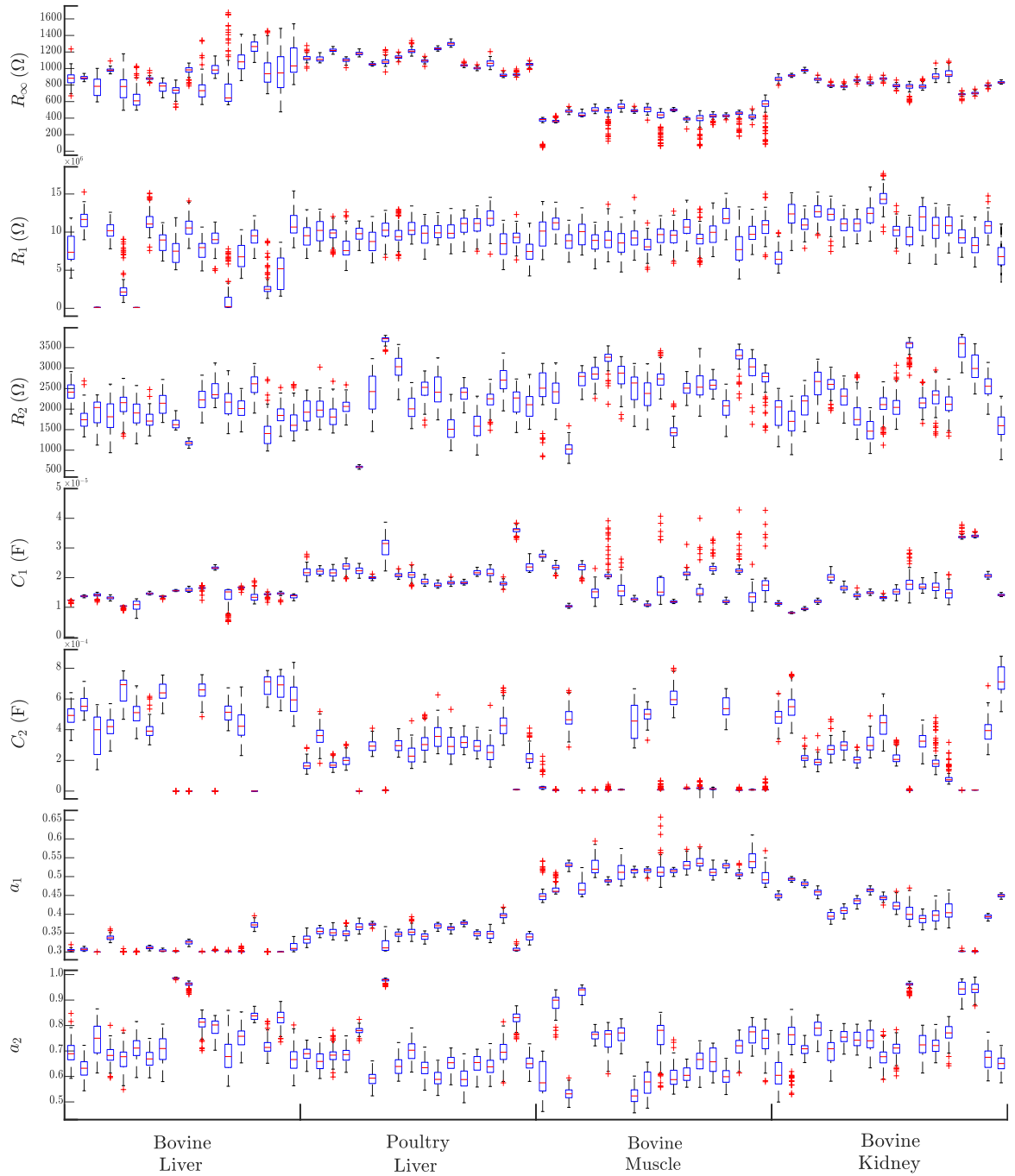
Figure 3.12: Boxplots that display the distribution of the circuit parameters for 4 of the tissues, with 18 samples each, extracted using RPD-NSGA-II. The line within the box denotes the median value. The cross outside of the boxes denote outliers in the data.

3.3 Discussion & Comparison of Methods

There are a few advantages to fitting the raw spectroscopy data to an equivalent circuit model. The fit curve interpolates the data between the measured frequencies, aids in smoothing out slightly noisy data, and provides easy to digest parameters to use when comparing different tissues.

The choice to fit the data to a model comes with some disadvantages. Specifically, the time required to fit the data to the model is of great significance. Ideally, the best fit will be achieved in as little time as possible to aid in the goal of achieving real-time haptic feedback. There is a significant difference in how successful the methods described in this chapter are able to achieve this goal. Both of these methods were implemented in MATLAB 2020a, running on Windows 10, 3.4 GHz CPU with 2 cores and 8 GB installed RAM. On average, a single impedance spectrum provided to the Newton Raphson method takes 0.19 seconds to complete 100 iterations, where parameters can determined to an acceptable level of fit. In comparison, 100 iterations of the RPD-NSGA-II method takes, on average, 1.3 seconds. This is a result of the increased number of function calls for the multi-objective approach, as each member of the population requires additional computations. Furthermore, it is seen that the RPD-NSGA-II method does not produce converge as quickly as the Newton-Raphson method. When looking at Figures 3.13(a) and 3.13(b) it is evident that 100 iterations is not sufficient to fit the sample, and only converged near 2000 iterations. The method took 1.48 seconds to complete 100 iterations and 16.89 seconds in 2000 generations. In comparison, the Newton-Raphson method can successfully converge in 100 iterations, but further generations do not improve the fit, as it has likely entered a local minimum solution that it will not escape. This behaviour perfectly encapsulates the difference between a deterministic and stochastic algorithm in optimisation.

On the other hand, there is a jarring obstacle in using the Newton-Raphson method: the initial guess of parameters. While this chapter presents an empirically tested method in selecting the initial values for the circuit parameters, they do not guarantee
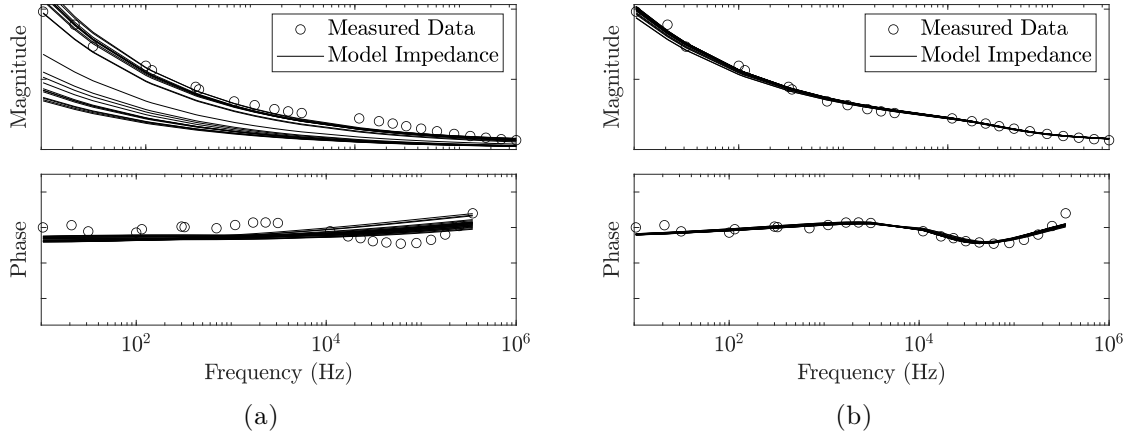
Figure 3.13: A comparison of the number of iterations of the RPD-NSGA-II optimisation method when trying to fit the impedance of a Bovine Liver sample. (a) 100 generations. (b) 2000 generations.

that the method will converge to a set of parameters that yield an acceptable level of fit to the data. In fact, it is possible that the solution may not converge, where one or more parameters fails to approach a steady value. It is for this reason, among other efficiencies, that researchers have explored improved versions of the method, including the Levenberg–Marquardt algorithm [82] [70], which alters the rate of change to a parameter through iterations [83].

The issue with convergence with the Newton-Raphson method is seen by its inability to solve for all 7 of the model parameters. The increase in the dimension of the problem further compounds the difficulty in finding a solution. In comparison, the RPD-NSGA-II method was successfully able to determine all 7 of the parameters.

With the RPD-NSGA-II method, multiple solutions are generated that fit the data. One should consider their strategy in how this data will be used in tissue classification. In a Newton-Raphson method, only a single set of parameters are introduced, making the comparison straightforward. This is not the case in the multi-objective approach, as all of the solutions generated in the Pareto front are equally viable results.

In closing of this chapter, two methods showed how the raw impedance data could be fit to a model, each with their strengths and weaknesses. In the next chapter, tissue classification will be discussed, where the extracted model parameters may be used.

Chapter 4

Classification of Tissues from Electric Impedance Spectroscopy

This chapter develops another crucial part of building toward a haptic feedback surgical tool: tissue discrimination. The task at hand is to determine how a tissue can be classified from electric impedance. There are many ways to approach this problem, and may only be applicable given the available information.

Machine learning based approaches, such as neural networks [84] [22], require very large sets of data to train their models. One needs to be able to provide a database of tissue information, whether that be the impedance data at given frequencies or model parameters, and a corresponding tissue label.

Non-parametric pattern recognition approaches like k-Nearest Neighbours (kNN) [85] [22] could be used but the algorithm is known to struggle with higher dimension problems [86]. Dimension reduction techniques could be utilised to pre-process the data, such as principal component analysis, which determines the most distinct features.

One approach seen from breast cancer researchers, Da Silva, Marques and Jossinet [86] [87] is to use linear discriminant analysis with features of the complex plane plot of the impedance. These features include the impedance at the lowest sampled frequency, the phase angle at 500 kHz, the area under the impedance spectrum, among other properties [86]. Inspired by the features used in [86], Daliri developed a support vector machine using the same features [88].

Another approach is seen by direct comparison of the model parameters found in Chapter 3. In the paper by Laufer et al. the impedance data of healthy liver and a tumour are fit to the Cole-Cole model, and found sufficient difference in the parameters, notably in the electrical conductivity at lower frequencies [89].

A probability based approach, the Naïve Bayes classifier, has been used with impedance spectroscopy in a few publications. Some have used the Bayesian approach to classify from the impedance at select frequencies [90]. The Injeq system has also been used with a Bayesian algorithm for tissue classification [91]. Similarly, there have been attempts at discriminating benign and malignant thyroid cancer from EIS using a

Bayesian belief network [92].

Ultimately, this brief overview of different methods illustrates the open-ended nature of the classification problem. Whether one chooses to look for defining features in the impedance spectra, or compare the values from equivalent circuit parameters, there are many ways to attempt to classify a new tissue sample. The previous chapters of this thesis have introduced the collection of electric impedance data of a tissue and how that data can be fit to an equivalent circuit model. Therefore, this chapter will develop several methods for classification, including a least square error comparison with the impedance or model parameters, a Bayes approach, and a modified kNN method.

In the interest of developing a real-time tissue identification tool, the classifier should be able to rapidly determine the label for a new sample: whether it new sample is provided as raw impedance measurements or extracted model parameters.

Any of these classification methods require examples to compare a new sample against. In this thesis the spectra collected in Section 2 are separated into two categories: training and test data. The training data can be thought of as the database. The database contains the selected samples' impedance spectra and the double-dispersion Cole model parameter values as determined by the algorithms presented in Chapter 3. All of the samples are labelled with that tissue they represent. In comparison, one can think of a sample in the test data as a new measurement - that which has not yet been labelled. The classifiers presented here should be able to correctly predict the true labels for the samples in the test data set.

4.1   Lease Square Error Comparison: Electric Impedance

A simple classification method is introduced in this section. The principle approach is to use the normalised least square error (LSE) of the test sample impedance against that of the training data impedance, with weights applied to the error at specific frequencies. This enables the method to classify where distinguishing features are

most prominent in the spectrum. For example, the location of the pole zero pair seen around 10^4 Hz, the impedance as frequency becomes large ($\omega \to \infty$ Hz) or small ($\omega \to 0$ Hz) may constitute unique features across different types of tissue, and should be weighted such that they have more impact on the outcome of the classifier. The weight for the error at a given frequency is denoted $\mathbf{w}_f$, and the similarity/fitness score $\mathbf{g}$ for the xth training sample can be stated as,

$$\mathbf{g}_x = \left(\sum_{n=1}^{23} \mathbf{w}_{f,n} \left(\frac{|\mathbf{z}|_{\mathbf{t,n}} - |\mathbf{z}|_{\mathbf{s,n,x}}}{|\mathbf{z}|_{\mathbf{t,n}}} \right)^2 \right)^{-1} + \left(\sum_{n=1}^{23} \mathbf{w}_{f,n} \left(\frac{(\angle\mathbf{z})_{\mathbf{t,n}} - (\angle\mathbf{z})_{\mathbf{s,n,x}}}{(\angle\mathbf{z})_{\mathbf{t,n}}} \right)^2 \right)^{-1} \quad (4.1)$$

where n is the frequency index, $\mathbf{w}_{f,n}$ denotes the nth weight applied at the frequency, $|\mathbf{z}|_{\mathbf{s,n,x}}$ and $(\angle\mathbf{z})_{\mathbf{s,n,x}}$ are the magnitude and phase of the xth training sample respectively, equivalently $|\mathbf{z}|_{\mathbf{t,n}}$ and $(\angle\mathbf{z})_{\mathbf{t,n}}$ are for the test sample to be classified.

Simply put, the largest value of $\mathbf{g}$ corresponds to the most similar match between the test and the training sample. Therefore the test sample will adopt the tissue label of the training sample which has the largest value in $\mathbf{g}$. There are 103 samples in the test data set, see Table 4.1 for a detailed list.

4.1.1 Determining Weights for LSE Classifier

The fitness functions in (4.1) use weights to emphasise a particular feature of the impedance spectra. The question then becomes, how to select effective values for these weights. A multitude of optimisation methods could be utilised, but this instance makes use of Particle Swarm Optimisation (PSO). The training data-set is used exclusively to determine the weights with PSO.

PSO is a stochastic algorithm where possible solutions $\mathbf{p}$ are explored based on the individual's personal best success $\mathbf{p_b}$ and the best success of its neighbours $\mathbf{p_g}$. A population member houses a number of variables equal to the dimension of the problem. In this application there are 23 weights to solve for in $\mathbf{w}_f$. Through the ith iteration

of the optimiser, the values of a population member are updated by its respective velocity $\mathbf{v}_i$,

$$\mathbf{v}_{i+1} = \mathbf{v}_i + \left(c_1 r_1 (\mathbf{p_b} - \mathbf{p}_i) + c_2 r_2 (\mathbf{p_g} - \mathbf{p}_i) \right) \tag{4.2}$$

$$\mathbf{p}_{i+1} = \mathbf{p}_i + \mathbf{v}_{i+1} \tag{4.3}$$

where c_1 and c_2 are coefficients used to bias the personal or global best, favouring exploration or convergence. Randomness is introduced by the random numbers r_1 and r_2 for each member in the population.

The objective in this method is to maximise the accuracy in identifying the labels of the training data set. In essence, the same fitness function in (4.1) is used but the test sample is one of the training data samples removed. With the provided weights from the current population member, the "test" sample label is predicted with (4.1). If the "test" sample is correctly labelled, the score of this population member increments. The process iterates through all of the samples in the training data.

The final score, or fitness, for the population member is determined using,

$$f_w = \frac{\text{Number of Correctly Labelled Samples}}{\text{Total Number of Samples}} \tag{4.4}$$

The process repeats until either one of two stopping criteria are met: a maximum number of iterations has been exceeded, or a population member has perfect fitness.

In this application, 25 population members were created and each weight was randomly assigned an initial value between 0.1 and 10. c_1 and c_2 were selected as 1.0 and 2.0 respectively. The maximum number of allowed iterations was 1000.

The PSO method determined the weights at each frequency to be,

$$
\mathbf{w}_f = \begin{bmatrix} 0.010 & 3.629 & 2.281 & 0.010 & 10.000 & 0.010 & 0.010 & 7.870 & \dots \\ 0.010 & 2.300 & 0.010 & 0.010 & 9.445 & 10.000 & 5.204 & 0.010 & \dots \\ 0.010 & 0.010 & 10.000 & 0.010 & 10.000 & 7.037 & 10.000 & & \end{bmatrix} \quad (4.5)
$$

It is interesting to note the frequencies selected by the optimiser as having most distinct features. As expected, since the standard deviation of the impedance is less variable at higher frequencies, their associated weights are much larger than those at lower frequencies. However, some lower frequencies also received large weights, specifically 114.58 Hz and 700 Hz.

4.1.2 Results of LSE Classifier: Electric Impedance

The classifier was equipped with the optimised weights and used on the test data-set. Figure 4.1 displays the correlation between the predicted labels of the test data-set and the actual labels. The classifier displays good performance, achieving an overall accuracy of 80.58 %. An issue is seen in the Gelatin (Green) tissue, where every test sample was incorrectly labelled as Agar (Yellow 1). This result is due to the similar impedance values the two tissues share across the sampled frequencies.

The advantage of the least squares error method is that it eliminates the need to fit the data to a model. Depending on the optimiser used for model fitting, this can lead to substantial savings in computation time, which is desirable to achieve real time tissue classification. However, as addressed in the preceding section, the fitting the data to a model has its own advantages. Therefore, the following classifier addresses how one may utilise the model parameters for classification.
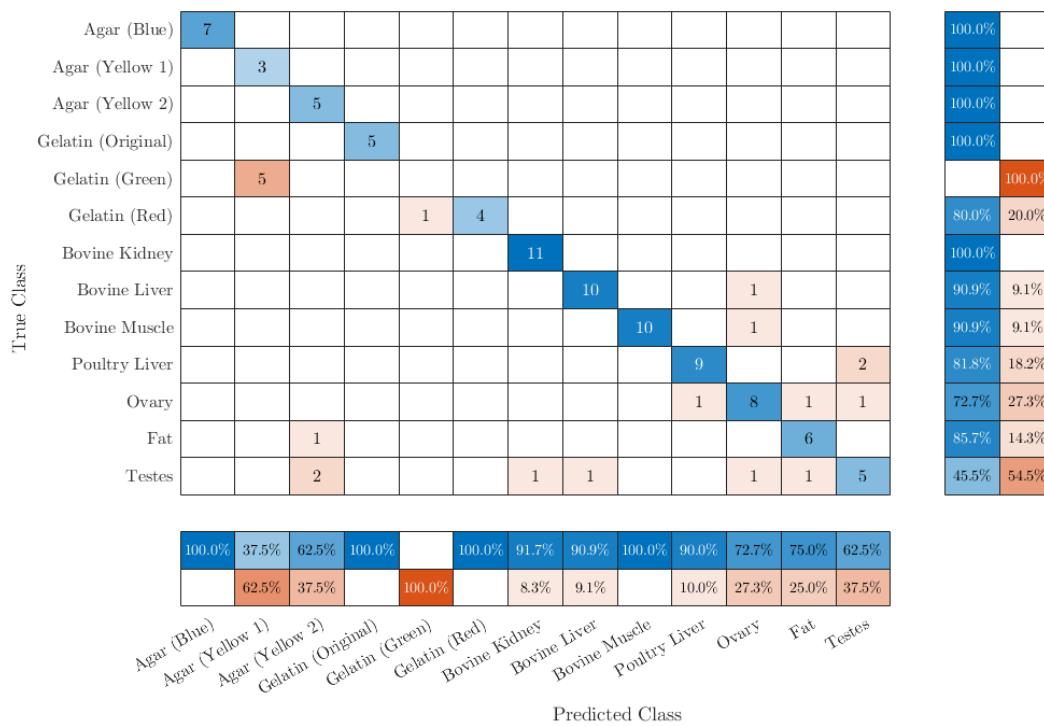
Figure 4.1: A confusion matrix that compares the predicted tissue labels to the actual labels from the LSE classification process with the impedance test data-set and weighted frequencies. The results show a strong correlation between the predicted and actual tissue labels.

4.2 LSE Comparison: Circuit Model Parameters

A similar LSE analysis can be performed with the extracted model parameters from Chapter 3. From the multi-objective approach, multiple solutions are generated that fit the impedance data. The LSE for each solution is compared to all of the solutions within the database. Each test data solution is classified by taking the label of the training sample with the smallest LSE.

For the ith solution of the test sample, the jth parameter $\mathbf{p_{t,j,i}}$ is compared to the jth parameter in the qth solution of the xth training sample $\mathbf{p_{s,j,q,x}}$. The similarity of the solutions determined through LSE of their respective model parameter,

$$\mathbf{h}_i = \sum_{j=1}^{7} \mathbf{w}_{p,j} \left(\frac{\mathbf{p_{t,j,i}} - \mathbf{p_{s,j,q,x}}}{\mathbf{p_{t,j,i}}} \right)^2 \tag{4.6}$$

With all solutions of the xth training sample evaluated, the solution with the smallest value of $\mathbf{h}$ is the most similar to the test sample solution. The label of the training sample, that houses this successful solution, is assigned to the test sample solution.

When all of the test sample solutions are labelled, the unique labels are counted. The most frequent label in the solutions is used as the label for the test sample.

The vector $\mathbf{w}_p$ houses the weights that alter the impact of the parameter error, where subscript j is the index of said vector. As seen in the previous classifier, these weights can be determined through the PSO method, using only the data present in the training samples.

4.2.1 Determine Weights for Model Parameter LSE Classifier

PSO is used here again to determine suitable values to use in the classifier, refer to (4.2) through (4.4). Here, the optimiser is searching for the weights for each model parameter, therefore this is a 7-dimension problem.

Once again, to determine the weights the training data was used exclusively. This time, the training dataset was further segmented into two groups to create new sets of test and training data. The 11 samples were separated into 4 and 7 samples for the new test and training data respectively. From this new batch the optimiser would classify the test samples using the method described in the preceding section and the new training data.

Within the optimiser the weights were bounded between 0.001 and 100, with the initial 50 population members randomly assigned values between them. The variables c_1 and c_2 were both assigned as 2.0. The stopping criteria was a population member achieving perfect fitness between the training and test labels, or exceeding 100 generations.

From this process, the weights were determined to be,

$$\mathbf{w}_p = \begin{bmatrix} 92.4 & 75.47 & 97.73 & 6.36 & 6.35 & 83.3 & 100 \end{bmatrix} \tag{4.7}$$

4.2.2 Results of LSE Classifier: Circuit Model Parameters

The results of this classifier can be seen in Figure 4.2, which displays the success of predicting labels of the test data-set. The overall accuracy of the classifier was 71.84 %. As expected, the classifier still struggled with confusing Gelatin (Green) for Agar (Yellow 1), as the model parameters are based upon their similar impedance data. Interestingly, this classifier was better able to predict Testes tissue, than the previous classifier.
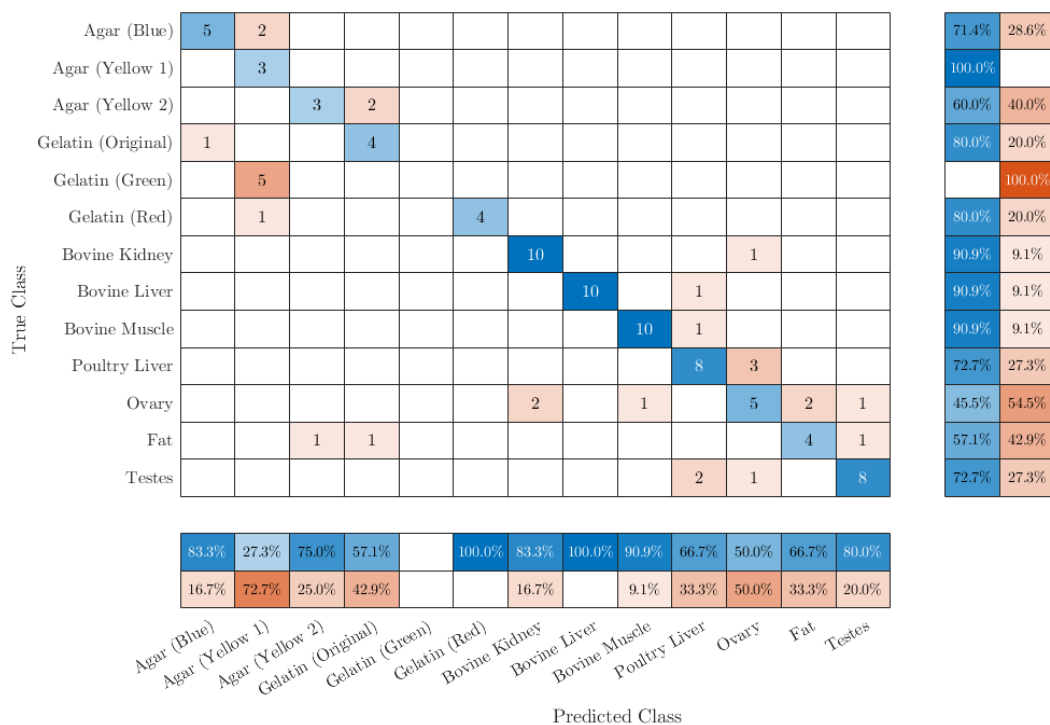
Figure 4.2: A confusion matrix that compares the actual and the predicted tissue labels from the LSE classifier using the extracted circuit model parameter test data set.

Confusion matrix — True Class (rows) vs Predicted Class (columns):

True Class	Agar (Blue)	Agar (Yellow 1)	Agar (Yellow 2)	Gelatin (Original)	Gelatin (Green)	Gelatin (Red)	Bovine Kidney	Bovine Liver	Bovine Muscle	Poultry Liver	Ovary	Fat	Testes		
Agar (Blue)	5	2												71.4%	28.6%
Agar (Yellow 1)		3												100.0%	
Agar (Yellow 2)			3	2										60.0%	40.0%
Gelatin (Original)	1			4										80.0%	20.0%
Gelatin (Green)		5													100.0%
Gelatin (Red)		1				4								80.0%	20.0%
Bovine Kidney							10			1				90.9%	9.1%
Bovine Liver								10		1				90.9%	9.1%
Bovine Muscle									10	1				90.9%	9.1%
Poultry Liver										8	3			72.7%	27.3%
Ovary							2		1		5	2	1	45.5%	54.5%
Fat			1	1								4	1	57.1%	42.9%
Testes											2	1	8	72.7%	27.3%
	83.3%	27.3%	75.0%	57.1%		100.0%	83.3%	100.0%	90.9%	66.7%	50.0%	66.7%	80.0%		
	16.7%	72.7%	25.0%	42.9%			16.7%		9.1%	33.3%	50.0%	33.3%	20.0%		

4.3 Modified k-Nearest Neighbours

A popular, yet relatively simple classification algorithm, kNN operates on the principle of comparing a test sample to training samples through a distance measure. The distance function can take many forms, including Euclidean, Chebychev, and Manhattan [93].

For this application kNN is used with the equivalent circuit model parameters that were extracted from RPD-NSGA-II in Chapter 3. As a reminder, each tissue sample has 25 solutions; where each solution contains values for the 7 parameters of the double-dispersion Cole model, refer to Figure 4.4.

The objective is to determine the label of the test sample. To do this, each of the test sample's 25 solutions are classified using kNN, and the label that occurs the most is used as the label for the test sample.

For each parameter in the solution, the Euclidean distance is determined between test sample solution $\mathbf{p}_{t,j}$ and each of the training sample's solutions $\mathbf{p}_{s,j}$. Since the values for some of the parameters differ by several orders of magnitude, the distances are normalised by the test sample value,

$$d = \left(\sum_{j=1}^{7} \left(\frac{\mathbf{p}_{t,j} - \mathbf{p}_{s,j}}{\mathbf{p}_{t,j}} \right)^2 \right)^{0.5} \tag{4.8}$$

To prevent the solutions from one sample dominating, only the shortest distance is considered. To elaborate, 25 distances are determined, one for each solution, and the minimum value is used to represent the tissue sample. This is repeated for each tissue sample until there is one distance per sample in the training data-set. With the distances to each sample calculated, the vector is sorted in ascending order, and the first k entries depict the nearest training samples to the test solution. The tissue type that occurs most often is used to label the test solution.

With $k = 5$ it is possible that the most frequent label among neighbours is a tie. For example, the 5 nearest neighbours to an arbitrary test solution return 2 Fat solutions, 2 Ovary solutions and 1 Testes solution. The label would be either Fat or Ovary. In this event, the value of k is decreased, such that the nearest 4 solutions are considered. If the tie persists, k is decremented again, to a minimum of 1, until the label is determined for the solution. Note that alternatively one could increment k to consider additional neighbours to break a tie. The testing here found that reducing k produced more accurate results, in part that additional neighbours could introduce more ties with other tissues in some cases.

With all of the solutions labelled, once again, the most frequently occurring label is used as the label for the test sample.

4.3.1 Results of Modified k-Nearest Neighbours

The results of this classifier are presented in Figure 4.3. Overall, the classifier achieved an accuracy of 59.22 %. Ovary and Gelatin (Green) samples struggled significantly in this method, often being mistaken for Bovine Kidney and Agar Yellow 1. The Gelatin and Agar tissues have similar impedance and, as a result would share similar equivalent circuit values. Consequently, significant error is to be expected when using the parameters in classification. Interestingly, the Ovary and Bovine Kidney tissues impedance spectra also share a similar shape, with slightly different impedance, see Figure 2.8. This potentially explains why the parameters may result in similar in issues in classification, where the impedance did not, see Figure 4.1.

True Class \ Predicted	Agar (Blue)	Agar (Yellow 1)	Agar (Yellow 2)	Gelatin (Original)	Gelatin (Green)	Gelatin (Red)	Bovine Kidney	Bovine Liver	Bovine Muscle	Poultry Liver	Ovary	Fat	Testes		
Agar (Blue)	2	5												28.6%	71.4%
Agar (Yellow 1)		3												100.0%	
Agar (Yellow 2)			5											100.0%	
Gelatin (Original)				4							1			80.0%	20.0%
Gelatin (Green)		5													100.0%
Gelatin (Red)						5								100.0%	
Bovine Kidney							9			1	1			81.8%	18.2%
Bovine Liver								11						100.0%	
Bovine Muscle							1		9	1				81.8%	18.2%
Poultry Liver							3			6	2			54.5%	45.5%
Ovary							6		2		1	1	1	9.1%	90.9%
Fat				2			1					2	2	28.6%	71.4%
Testes			3				1	1		1	1		4	36.4%	63.6%
	100.0%	23.1%	62.5%	66.7%		100.0%	42.9%	91.7%	81.8%	60.0%	20.0%	66.7%	57.1%		
		76.9%	37.5%	33.3%			57.1%	8.3%	18.2%	40.0%	80.0%	33.3%	42.9%		

Figure 4.3: A confusion matrix that compares the predicted tissue labels to the actual labels from the k-Nearest Neighbours algorithm and the equivalent circuit model parameters from RPD-NSGA-II.

4.4 Naïve Bayes Classifier

When extracting the circuit model parameters it is possible that the extraction process will not necessarily converge to the same set of parameter values for any given tissue spectroscopy measurement. Each parameter will have a distribution of values for a given tissue, see Figures 3.7 and 3.12. Thus, when it comes to classifying the tissue based on these parameter values, a probability-based approach can be used. The Naïve Bayes classifier is well suited for these types of problems. One defines a set of features from the circuit parameters $\mathbf{p}$ that belongs to a tissue type class c, formerly tissue labels in this chapter. The probability of a test sample belonging to a class given a set of features is defined as [94],

$$P(c_k|\mathbf{p}_j) = \frac{P(\mathbf{p}_j|c_k)P(c_k)}{P(\mathbf{p}_j)} \tag{4.9}$$

where $\mathbf{p}_j$ denotes the jth parameter of $\mathbf{p}$ and c_k refers to a specific tissue type class. $P(c_k|\mathbf{p}_j)$ is then a probability density function for a class given a feature, assuming a Gaussian distribution. The probability of a value for a parameter x belonging to class can be found using the formula,

$$P(\mathbf{p}_j|c_k) = \frac{1}{\sigma\sqrt{2\pi}}e^{-\frac{1}{2}\left(\frac{x-\mu}{\sigma}\right)^2} \tag{4.10}$$

provided that values for the mean μ and standard deviation σ of the class are known.

In essence, from (4.9), one can determine which class a given parameter will belong to based on which has the largest probability [95],

$$\text{predicted class label} \leftarrow \arg\max_{j=1...7} P(c_k|\mathbf{p}_j) \tag{4.11}$$

The classifier is labelled as naïve since the parameters are assumed to be statistically independent from one another [96]. The combined probability density function for a

set of features can be written as,

$$P(\mathbf{p}|\mathbf{c_k}) = \prod_{j=1}^{7} P(\mathbf{p}_j|c_k) \qquad (4.12)$$

thus, the predicted label can be found by considering multiple parameters,

$$\text{predicted class label} \leftarrow \arg\max_{j=1...7} P(c_k) \prod_{j=1}^{7} P(\mathbf{p}_j|c_k) \qquad (4.13)$$

Based on a training set of parameter data, a new tissue sample can be labelled based on the probability of it belonging to a type of tissue with similar circuit parameters. The training data-set contains 11 samples from each tissue type, and the remaining available samples are used in the test data set, refer to Table 4.1.

A summary of the proposed classification process using NBC is shown in Figure 4.4. The impedance data for a test sample is fed into the optimiser to determine the model parameters. The database contains 11 samples of each tissue, where each sample has 25 solutions (combinations of circuit model parameter values) that were generated by RPD-NSGA-II. With the same extraction method 25 solutions are created for the test sample. One of these test sample solutions, the determined model parameters for the test sample, are compared to all of the solutions in the database using Naïve Bayes. The label of the solution in the database with the highest value from (4.13) is assigned to the test solution. This is repeated until the class labels are determined for all solutions from the test sample. The number of labels are then counted, and the label with the most occurrences is used as the overall label for the test sample. Refer to Figure 3.10.

Table 4.1: Number of Training & Test Data Samples

Tissue	No. of Train Samples	No. of Test Samples
Agar (Blue)	11	7
Agar (Yellow 1)	11	3
Agar (Yellow 2)	11	5
Bovine Kidney	11	11
Bovine Liver	11	11
Bovine Muscle	11	11
Fat	11	7
Gelatin (Green)	11	5
Gelatin (Original)	11	5
Gelatin (Red)	11	5
Ovary	11	11
Poultry Liver	11	11
Testes	11	11
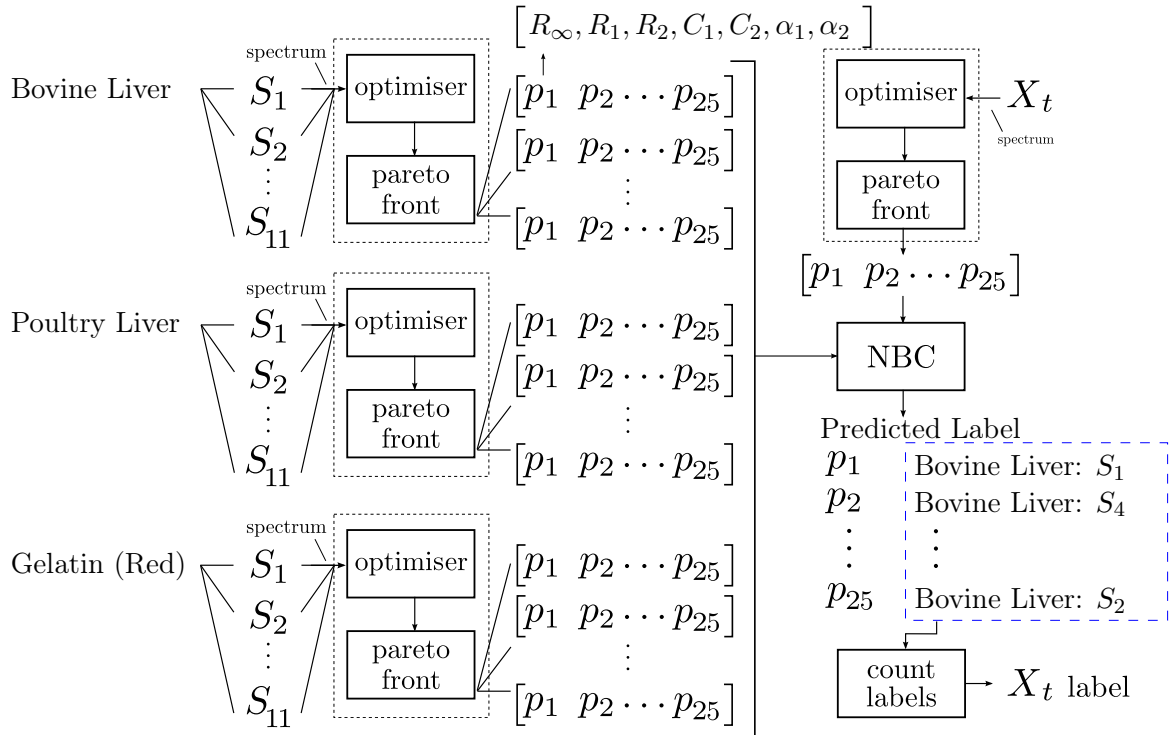
Figure 4.4: The proposed classifier using Naïve Bayes and multiple model parameter solutions. The left side depicts the database, or training data. Each tissue For each tissue 11 samples are present, where each sample has 25 solutions.On the right side of the figure a test sample is introduced. The impedance is converted to 25 different solutions of model parameters. Using Naïve Bayes each test solution is labelled. With all test solutions labelled, the most frequent label is used as the label for the test sample.

4.4.1 Results of the Naïve Bayes Classifier

It is evident from Figure 4.5 that the classifier yielded poor results in classifying the test data-set. For multiple tissues the classifier struggled to predict the samples correctly. In the upcoming section, a modification is made to this method, which aims to potentially remedy the issues seen here.

True Class \ Predicted	Agar (Blue)	Agar (Yellow 1)	Agar (Yellow 2)	Gelatin (Original)	Gelatin (Green)	Gelatin (Red)	Bovine Kidney	Bovine Liver	Bovine Muscle	Poultry Liver	Ovary	Fat	Testes		
Agar (Blue)	5	2												71.4%	28.6%
Agar (Yellow 1)	2				1										100.0%
Agar (Yellow 2)			4		1		1							66.7%	33.3%
Gelatin (Original)				4							1			80.0%	20.0%
Gelatin (Green)		1			3	1								60.0%	40.0%
Gelatin (Red)		3				2								40.0%	60.0%
Bovine Kidney							7		1		3			63.6%	36.4%
Bovine Liver											11				100.0%
Bovine Muscle									4		7			36.4%	63.6%
Poultry Liver										5	6			45.5%	54.5%
Ovary		1					1		1		8			72.7%	27.3%
Fat				1							4	2		28.6%	71.4%
Testes					1						7		3	27.3%	72.7%
	71.4%		80.0%	80.0%	50.0%	66.7%	77.8%		66.7%	100.0%	17.0%	100.0%	100.0%		
	28.6%	100.0%	20.0%	20.0%	50.0%	33.3%	22.2%		33.3%		83.0%				

Figure 4.5: A confusion matrix that compares the predicted tissue labels to the actual labels from the Naïve Bayes classifier with the test data set.

4.5 Weighted Naïve Bayes Classifier

While it is desirable to consider all of the circuit model parameters, some model parameters may be better markers for classification. For example, R_∞ may be distinct among the different tissue samples, whereas values for α_2 might be similar across all tissues. For this reason, the former classifier is built upon, but the addition of weights
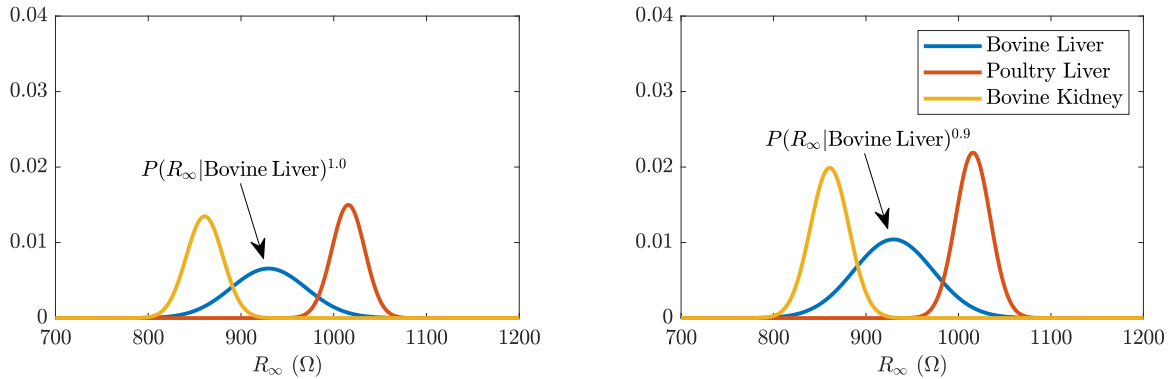
Figure 4.6: A comparison of the probability density functions for three tissue samples with weights 1.0 and 0.9. It is seen that the weights can alter the probability of a model parameter, and by extension, its impact on the classifier.

was considered:

$$\text{predicted label} \leftarrow \arg \max_{j=1...7} P(c_k) \prod_{j=1}^{7} P(\mathbf{p}_j|c_k)^{\mathbf{w}_j} \tag{4.14}$$

where $\mathbf{w}_j$ is the weight attributed to parameter $\mathbf{p}_j$ [97]. Refer to Figure 4.6 to visualise how the weight would impact a parameter.

4.5.1   Determine Weights for Naïve Bayes

Once again, PSO was used to determine the weights that would be used in this classifier, reference (4.2) to (4.4) as needed. The optimiser explored the landscape of a 7-dimension problem to determine the values that would achieve the best possible fitness (the highest amount of correct label predictions).

In this instance, 50 population members were created with random initial values between 0 and 30.

Negative weights were not considered as would have a contradictory effect in some cases. For example, consider a parameter has a value that does not belong to a given tissue: it would have a probability of 0. A negative weight, of -1 for instance, would alter the probability such that it is now infinitely likely. For this reason, should any population member attempt to explore values less than 0, it is set to 0. An upper

77
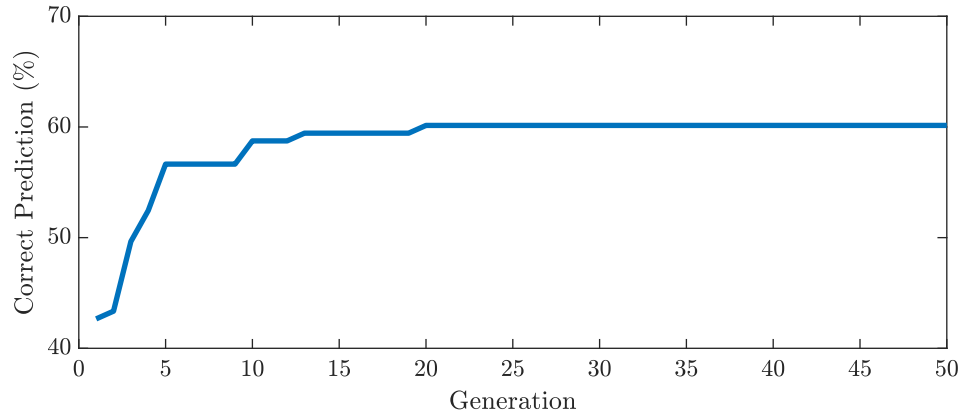
Figure 4.7: The fitness of the global best parameter through the generations of PSO for finding weights to use in weighted Naïve Bayes.

bound is also included, to prevent extreme attenuation of a probability. From repeated empirical testing, it was decided any weight value above 30 is set to 30.

The modifiers c_1 and c_2 were set as 1.0 and 2.0 respectively. The optimiser was executed for 50 generations. Upon completion, the population member with the best global fitness was found to have weights:

$$\mathbf{w} = [9.59 \ \ 2.45 \ \ 0 \ \ 6.92 \ \ 0 \ \ 9.39 \ \ 0] \tag{4.15}$$

It is interesting to note the inclusion of multiple instances where the weights are 0. A weight of 0 effectively removes the impact of a parameter from the classifier, as any positive real number raised to the power of 0 will be unity. According to the this population member the parameters R_2, C_2 and α_2 are not considered for classification.

Furthermore, these weights are determined based when only using the training data-set. Out of all the samples in the training data, the global best was only 60.14% correct in predicting the labels, see Figure 4.7. The implications of this are to be seen in the results with the test data.

4.5.2 Results of the Weighted Naïve Bayes Classifier

The weighted variant of Naïve Bayes performed better than the unweighted classifier, see Figures 4.8 and 4.5. The weighted classifier was able to accurately predict 51.92 % of the test samples overall. However, there is still a stark lack of success across the tissue types.

In an attempt to remedy this, the tissue can be segregated into similar groups. With the test and training data separated into the gel-based group and ex-vivo with freshly excised group, the PSO is executed again to determine the weights for these groups. With the new weights determined, the test samples were classified, see Figures 4.9(a) and 4.9(b). Improvement is seen once more, where the success rate of the classifier increased with the smaller groups.

True Class \ Predicted	Agar (Blue)	Agar (Yellow 1)	Agar (Yellow 2)	Gelatin (Original)	Gelatin (Green)	Gelatin (Red)	Bovine Kidney	Bovine Liver	Bovine Muscle	Poultry Liver	Ovary	Fat	Testes		
Agar (Blue)	5	2												71.4%	28.6%
Agar (Yellow 1)	1			2											100.0%
Agar (Yellow 2)		2	3									1		50.0%	50.0%
Gelatin (Original)				4							1			80.0%	20.0%
Gelatin (Green)					4	1								80.0%	20.0%
Gelatin (Red)		1			1	3								60.0%	40.0%
Bovine Kidney							7				4			63.6%	36.4%
Bovine Liver								4		1	6			36.4%	63.6%
Bovine Muscle							1		9		1			81.8%	18.2%
Poultry Liver										4	4		3	36.4%	63.6%
Ovary							1		2		8			72.7%	27.3%
Fat				1							4	2		28.6%	71.4%
Testes		1	3							2	4		1	9.1%	90.9%
	83.3%		50.0%	80.0%	57.1%	75.0%	77.8%	100.0%	81.8%	57.1%	25.0%	100.0%	20.0%		
	16.7%	100.0%	50.0%	20.0%	42.9%	25.0%	22.2%		18.2%	42.9%	75.0%		80.0%		

Figure 4.8: A confusion matrix that compares the predicted tissue labels to the actual labels from the weighted Naïve Bayes classifier with the test data set. Values for the weights were $\mathbf{w} = [9.59\ 2.45\ 0\ 6.92\ 0\ 9.39\ 0]$.

(a) Gel-based tissues — True Class vs Predicted Class

True Class \ Predicted	Agar (Blue)	Agar (Yellow 1)	Agar (Yellow 2)	Gelatin (Green)	Gelatin (Original)	Gelatin (Red)		
Agar (Blue)	4	3					57.1%	42.9%
Agar (Yellow 1)	1	1		1			33.3%	66.7%
Agar (Yellow 2)			5		1		83.3%	16.7%
Gelatin (Green)				4		1	80.0%	20.0%
Gelatin (Original)					5		100.0%	
Gelatin (Red)						5	100.0%	
	80.0%	25.0%	100.0%	80.0%	83.3%	83.3%		
	20.0%	75.0%		20.0%	16.7%	16.7%		

(a)

(b) Ex-vivo and freshly excised tissues — True Class vs Predicted Class

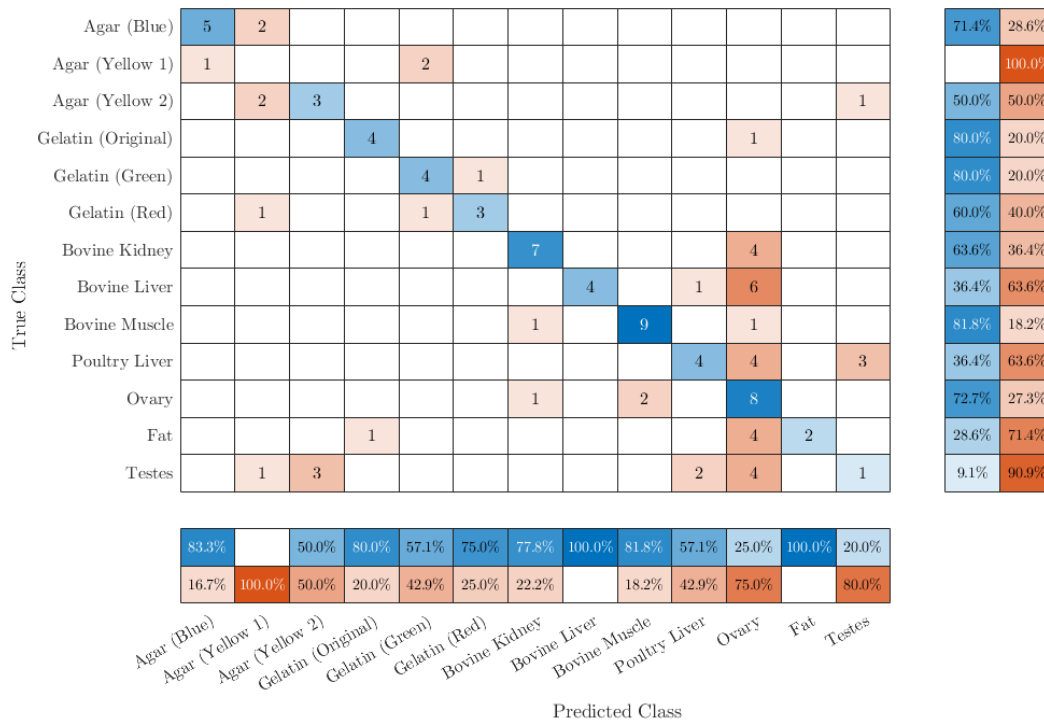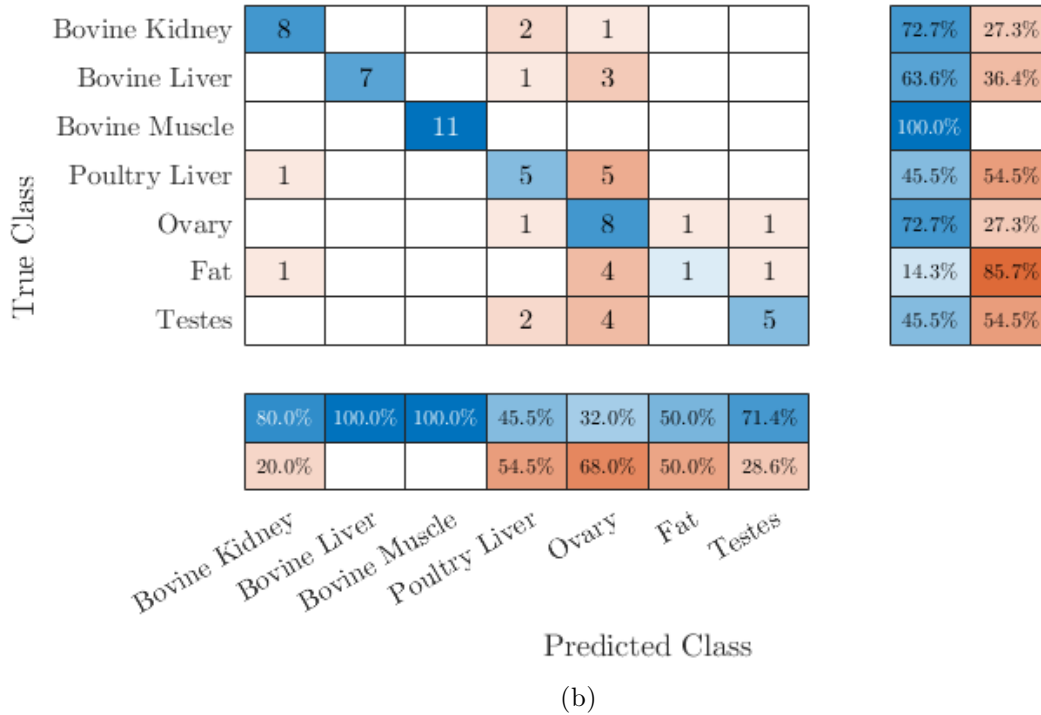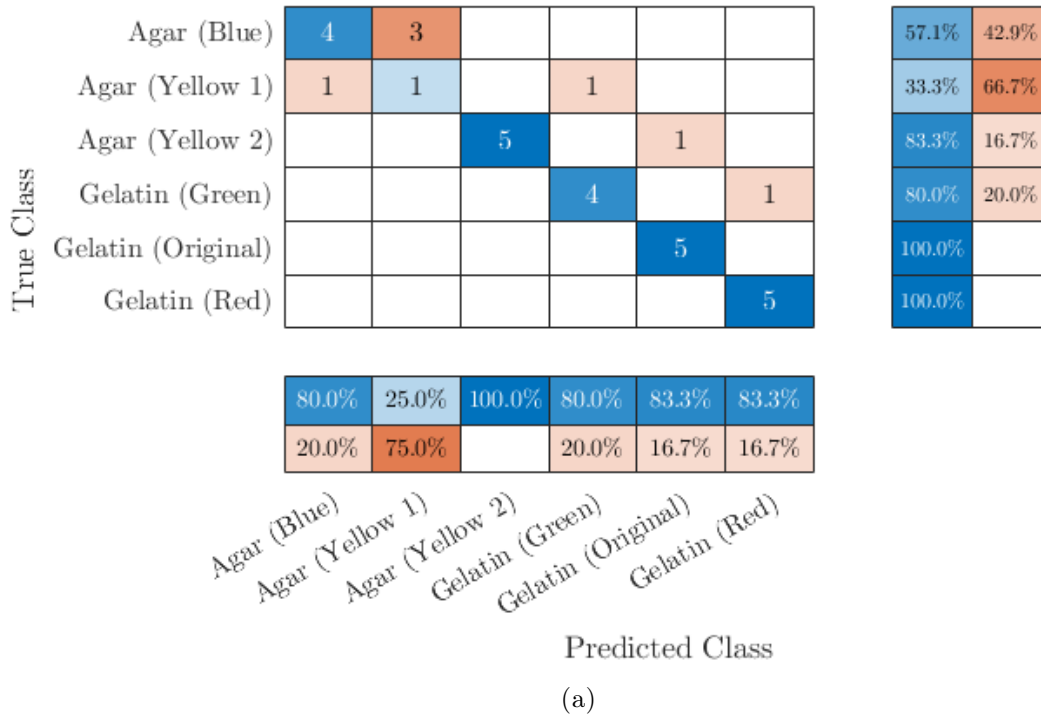| True Class \ Predicted	Bovine Kidney	Bovine Liver	Bovine Muscle	Poultry Liver	Ovary	Fat	Testes		
Bovine Kidney	8			2	1			72.7%	27.3%
Bovine Liver		7		1	3			63.6%	36.4%
Bovine Muscle			11					100.0%	
Poultry Liver	1			5	5			45.5%	54.5%
Ovary				1	8	1	1	72.7%	27.3%
Fat	1				4	1	1	14.3%	85.7%
Testes				2	4		5	45.5%	54.5%
	80.0%	100.0%	100.0%	45.5%	32.0%	50.0%	71.4%		
	20.0%			54.5%	68.0%	50.0%	28.6%		

(b)

Figure 4.9: Confusion matrices that compare the predicted tissue labels to the actual labels from the weighted Naïve Bayes classifier with the test data set for (a) gel-based tissues only where $\mathbf{w} = [0.20\ 0\ 0\ 3.55\ 0\ 11.48\ 0]$, and (b) ex-vivo and freshly excised tissues only with $\mathbf{w} = [30.00\ 0.04\ 0\ 0\ 12.63\ 0\ 0]$.

Table 4.2: Summary of Classifier Results

Classifier	Overall Accuracy	Figure No.
LSE Comparison: Electric Impedance	80.58 %	4.1
LSE Comparison: Model Parameters	71.84 %	4.2
Modified K-Nearest Neighbours	59.22 %	4.3
Naïve Bayes Classifier	45.19 %	4.5
Weighted Naïve Bayes Classifier:		
For All Tissues	51.92 %	4.8
For Gel-Based Phantoms	77.42 %	4.9(a)
For Ex-Vivo & Freshly Excised Tissues	61.64 %	4.9(b)

4.6   Comparing the Classifiers

This chapter explored multiple methods to classify a tissue from its electric properties, and with varying degrees of success. Looking at overall accuracy, the LSE classifier with weighted frequencies performed the best. However, there are merits and drawbacks to each method. In the LSE classifier it would have been possible for a sample in the training set to be an anomaly, and by chance happen to have similar impedance at the critical frequencies and different impedance elsewhere. This is feasible concern, as the impedance at lower frequencies has a relatively large standard deviation. It is for this reason one could consider the other classifiers such as kNN, to be more robust. The kNN classifier looks at multiple solutions, not just the most similar, and therefore one could argue it makes a stronger claim to its prediction.

A significant limitation to this analysis stems from the number of available samples. Depending on the application, machine learning approaches require a large amount of data to develop sound models that are relatively free of bias and noise. Furthermore, the robustness of the classifier could be tested through cross validation with independent test data-sets.

The performance of these classifiers could be improved by honing in the selected tissues in the training data. If one was attempting to discriminate tissues in prostate

brachytherapy for instance, one would only need tissues they would reasonably expect to encounter. In this example, the training data might consist of impedance data for glandular tissue, malignant cells or benign hyperplasia; you would not need to consider tissue you would not expect such as renal cortex of a kidney.

Ultimately, there are multiple ways to classify a tissue sample from the electric properties. In the next chapter, tissue classification is utilised in practical applications, and the culmination of this thesis is to be seen.

Chapter 5

Applications of EIS and Tissue Classification to Haptic Feedback

The preceding chapters of this thesis have developed the methods required to discriminate between different tissues using EIS, and shown its efficacy. With this capability unlocked, one needs to determine how it could be used to best communicate tissue information during surgery. One may wonder why the impedance spectra could not be directly shown as visual feedback. It could be presented as such, but one must remember in the higher cognitive load environment of the operating room, multiple sources vie for the surgeons attention, and adding another monitor to look at may lead to visual sensory overload [98]. As an alternative to recreating force or tactile sensation, some have turned to the idea of sensory substitution: replacing information we normally expect through touch to a different sense, such as hearing, temperature or smell. This was explored in [98], where auditory and visual feedback were used in RMIS. The results in one benchmark test showed that these alternative forms of feedback performed comparably to their force feedback trials. However, during the experiments the surgeons had preferred visual over audible feedback; something to note when considering continuous real-time information against discrete single-event information such as an audio alarm.

The principal motivations of implementing haptic feedback is to replicate the sensations that are lost in teleoperation, or to enhance otherwise imperceptible changes in tissue structure in traditionally manual procedures. As mentioned in Chapter 1, force sensors would be the intuitive choice, as it is well recognised that the mechanical stiffness of healthy and malignant tissue differ. There are known challenges with using these devices and a great deal of research has gone into resolving the issues of compensating for friction forces along the needle shaft, sensor placement, size, etc. Haptic feedback, simply put, is a means of communication in delivering information to the recipient. The recipient may be ignorant of how the data is acquired, in the surgery example, physicians need only know what tissue the tool is in to perform their tasks. Thus, force sensors are not necessary in conveying tissue information, the tissue can be determined through alternative means. For these reasons, the applications of haptic feedback that are traditionally used alongside force sensors are investigated

here with EIS in its stead.

Haptic systems normally seen with force sensors can be broadly fit into the categories of force feedback and tactile feedback. Force feedback, generally speaking, is accomplished where the input device also impedes the motion of the user, such that it recreates forces that the user expects while interacting with a virtual object. Many devices use active force feedback, where the forces are generated by elements like motors, but there is an increasing interest in passive haptic devices as well, where forces are realised through dissipative elements such as brakes [99]. Tactile feedback is concerned with recreating the sensation of touch [100]. Palpation is a common technique used by physicians to perceive or gauge the properties of tissue: shape, size, stiffness, etc. During RMIS the surgeon may not be able to utilise their sense of touch, hence the desire to recreate this lost sense. Vibrotactile feedback [101] can recreate tactile information through discrete vibration signals, harsh bumps can simulate a rough uneven surface, where short clicks can emulate key presses.

The following subsections of this chapter explore different implementations of haptic feedback with EIS as the sensing method. Force feedback in teleoperation and vibrotactile feedback in handheld tool insertion are tested and discussed.

5.1 Vibrotactile Feedback for Tissue Discrimination

5.1.1 Application Context

The scenario recreated in this application is a surgical procedure where the surgeon needs to manually insert a needle into tissue, and identify what it is. A real world analogue would be biopsy for breast cancer, where only a small amount of tissue is taken a sample for further histological analysis. If the biopsy tool was capable of alerting its wielder of tissue composition at the needle tip, including malignancy, before the biopsy core is extracted, it may lead to fewer false-negatives in instances where healthy tissue would have been otherwise sampled.

5.1.2 Relating Electric Impedance to Vibrotactile Feedback

The bridge between the tissue's electric impedance to haptic feedback is developed here. Biopsy is typically a handheld procedure and guided by ultrasound. Since the surgeon is in direct contact with the tool, a modification to the handheld tool is proposed. Vibrotactile feedback is easily achieved by installing a small vibration disc motor into the handle of the tool, see Figure 5.4. A small vibration motor (from Adafruit, New York, USA) is installed on the needle shaft to convey information to its wielder, see Figure 5.4. The vibration motor is connected to an IRFZ44N MOSFET motor driver and an ATmega328P microcontroller. The intensity of the vibration is controlled by altering the PWM signal sent to the gate of the MOSFET. The PWM frequency is configured to 30.64 Hz. The microcontroller was subsequently connected to a computer running the classification program. When the needle is inserted into tissue, EIS is used to classify what is at the tip and the motor will generate a vibration pattern that has been assigned to the tissue, allowing the wielder to identify where the needle tip is traversing.
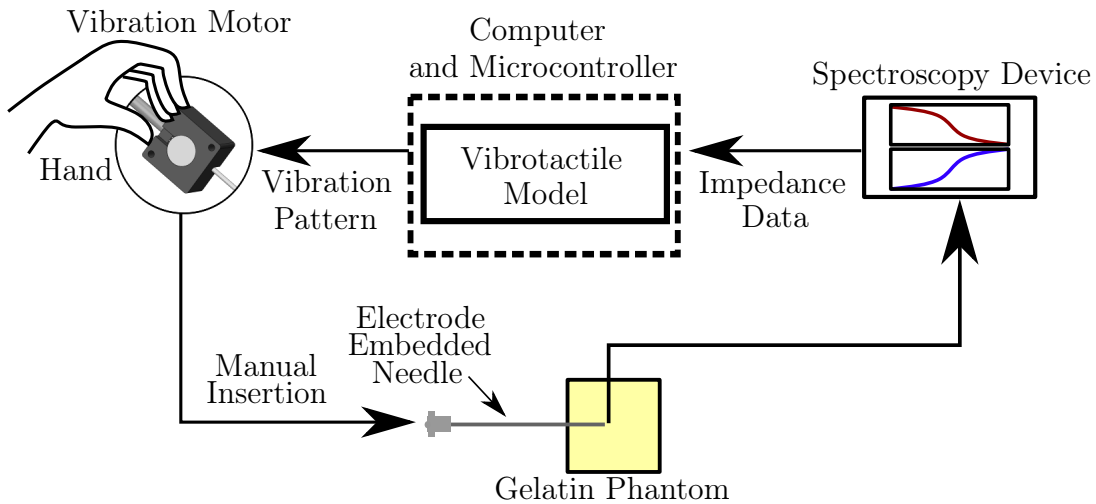
Figure 5.1: The proposed vibrotactile feedback system for manual insertion. The user holds the needle by an installed box that houses a vibration motor. When inserted into the phantom, the electric impedance is measured, and the tissue classified. The corresponding vibration pattern is sent to the user.

For this application, discrete vibration signals were assigned to the 3 broad categories one would expect in the surgery: healthy, benign, and malignant. To create these

Figure 5.2: The 5 vibration patterns initially considered to be used for vibrotactile feedback. The vibration signal envelope has a period of 0.6 seconds. (a) Pattern 1 (b) Pattern 2 (c) Pattern 3 (d) Pattern 4 (e) Pattern 5.

patterns, one can control a few parameters: the duration of the vibration envelope, the amplitude by altering the duty cycle, and vibration frequency of the signal. There are a few criteria to be cognisant of when dev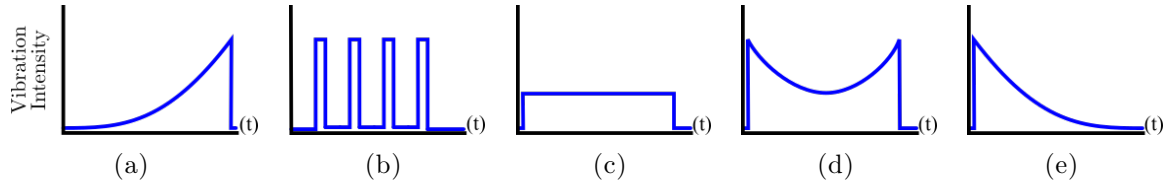eloping these signals. Foremost, it is crucial that these 3 patterns be distinct such that they would not be misinterpreted. Secondly, the signal envelope should be succinct enough to rapidly respond to the surgeon as they manoeuvre the needle, but long enough for them to recognise the pattern. To this end, 5 patterns were created, shown in Figure 5.2, and a pattern recognition experiment was conducted to determine which patterns the participants found to be the most distinct. From their feedback, the 3 most distinct signals can be assigned to represent the tissues.

To validate that the patterns in Figure 5.2 are uniquely identifiable, a preliminary test was performed with 10 participants, of various age and gender. These volunteers were tasked with recognising a vibration pattern and record its corresponding tissue type. Each test participant was given the same set of written instructions prior to starting the experiment. Each participant was trained on the vibration patterns and their correspondingly assigned tissue types. They held the needle at its base where the vibration motor was installed. When the participant was familiar with the vibrotactile feedback the test commenced. The participant sequentially received a vibration pattern and would write the corresponding tissue type on a provided answer sheet. Each participant was asked to identify 20 patterns in total: 10 for each hand. The pattern sequence and composition was built randomly.

Figure 5.3: Results of the vibration recognition trials presented as a confusion matrix. Rows represent the actual vibration pattern given to the participant and what they perceived is tallied in the columns. If the participant was not confident in their guess or unable to to determine the pattern, it was tallied under the rightmost column. All values listed as percentages.

5.1.3 Preliminary Pattern Recognition Experiment Results

The results of the vibration perception test are presented in Figure 5.3. It is seen that the users were able to more clearly identify some patterns over others. The most distinct patterns were Pattern 1, Pattern 2, and Pattern 4. With the selected patterns the results suggest strong correlation between the perceived and actual vibration pattern. Thus, the vibrotactile feedback can be integrated with the tissue classification method, which is investigated in the next section.

5.1.4 User Trial Study: Setup

In the second test a new group of participants were tasked with using the electrode embedded needle to probe a tissue phantom that was hidden from view, see Figure 5.4. The measurement, Newton-Raphson parameter extraction and weighted Naïve Bayes classification algorithms would then be incorporated into the experiment, from which the vibrotactile feedback pattern corresponding to the identified tissue is displayed.

To prepare for these user trials 3 gelatin phantom tissues were created and hidden

from the participant using the recipes for Gelatin (Original), (Green) and (Red) as detailed in Chapter 2. Gelatin phantoms were used in the experiments predominantly for control over the electric impedance, ensuring repeatable measurements, as new phantoms needed to be created to replace deteriorating samples after repeated use in the experiment. The Gelatin (Original), (Green) and (Red) tissues are relabelled as Tissue 1, Tissue 2 and Tissue 3, respectively, for the remainder of this section. In the experiment the participants were trained to identify them as healthy, benign and malignant tissue respectively, the assignment of which was arbitrarily selected. For each tissue 4 samples were created.

The user trials consisted of 12 new participants, which consisted of men and woman ranging in age from 22 years old to 57 years old and did not participate in the preliminary pattern recognition experiment. Each participant was trained to recognise the 3 vibration patterns and their corresponding tissue type prior to commencing the experiment. The training consisted of providing them with the vibration signal and verbally informed what it represented. When all patterns were communicated the participant was then quizzed on the patterns, where they were randomly provided with a signal and correctly respond with the associated label. When the participant was confident in recognising the patterns they were given the a standard set of written instructions to read prior to starting the test. They were instructed to use the electrode embedded needle to sequentially probe each of the hidden phantoms and based only on the perceived haptic feedback write down what they believe the tissue to be. They were only allowed to probe the tissue once before making a decision on the tissue type. They were tasked with identifying 12 phantoms in total. The user trial participants were not aware of the quantity of samples present, in essence, they were not informed that the tissues were equally represented.

The EIS system would continually monitor the impedance of the tissue, and attempt to classify the tissue at the needle tip. In this application the double-dispersion Cole model parameters were found using Newton-Raphson. A training set was also established using Newton-Raphson. Naïve Bayes was used as the classifier. When the
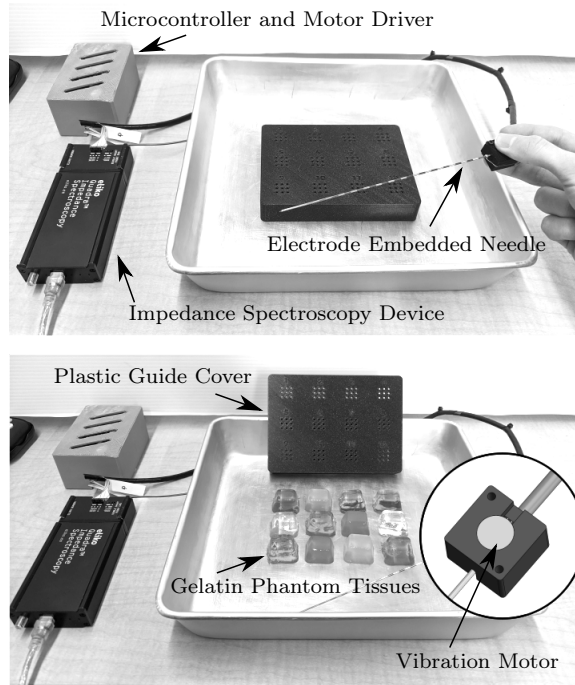
Figure 5.4: The experiment setup. The user holds an electrode embedded needle with by the base that houses a vibration motor. The needle is blindly inserted into one of the designated holes and punctures the gel based phantom tissue. The electric impedance measured at tip using spectroscopy determines the type of vibration pattern to be displayed to the user through a small motor encased at the base of the needle.

sample was classified the corresponding vibration pattern would be delivered.

The method described for this application, including the spectroscopy device interfacing, optimiser, classifier and microcontroller communication, was implemented in MATLAB 2019b. The method takes approximately 3.05 seconds to execute, where the impedance spectroscopy sample takes 2.995 seconds, Newton-Raphson takes 0.042 seconds to converge, Naïve Bayes takes 0.004 seconds to classify a new sample, and the serial communication to the microcontroller takes 0.002 seconds.

5.1.5 User Trial Study: Results

The results of this experiment, shown in Figure 5.5, are separated into 3 categories: the actual tissue and the label determined through the Naïve Bayes classifier, the vibration signal sent to the user once it was classified and what they perceived the vibration/tissue as, and the end result of the actual tissue to the user's guess.

Figure 5.5: Results from the user trials presented as confusion matrices. (a) The actual tissue sample against what the algorithm classified the tissue as. (b) The classified tissue against what the user perceived the tissue as through the vibrotactile feedback. (c) Comparison of the actual tissue to what tissue the user perceived. All values are listed as percentages.

5.1.6 Discussion: Outcome of the Application

The results from the user experiments reinforce the earlier observations. In Figure 5.5(a), there is a strong correlation between the actual and classified tissue, but the algorithm struggled with the similar samples. It is believed the algorithm had difficulty in distinguishing between the parameter values, as they are relatively similar than in the other tissue, see Figures 3.7. The most unique parameter among them is R_∞, which corresponds to the high frequency impedance. The remaining 4 parameters share some overlap, which may explain the inaccuracy in discriminating between tissues.

The results shown in Figure 5.5(b) further corroborate the findings in Figure 5.3 that, after a training session, the users were able to discern the tissue type based purely on the vibrotactile feedback with a relatively high degree of accuracy. Most of the volunteers had perfect perception of the vibrotactile feedback. The feedback received from the participants that struggled was the perceived similarity in the vibration patterns. This may be remedied by further exploring unique vibration patterns or the incorporating additional vibration motors, which enables many new possibilities for vibration patterns.

The series of experiments conducted suggest that vibrotactile feedback at the base of the needle was successful in communicating information about the tissue at the tip of the needle. However, the single vibration source is limited in the number of distinguishable patterns. The developed method struggled in classifying tissue samples with similar electric impedance. The presented method of combining electric impedance spectroscopy with vibrotactile feedback holds promise and with further development may one day be used to improve the clinical practices used today.

Not all procedures can be performed manually. Many procedures are performed with surgeon removed from the patient, where they control a robot remotely to operate on the patient. The upcoming section will explore this further, and how EIS can be used to develop haptic feedback in a different way.

5.2 Force Feedback in Teleoperation

5.2.1 Application Context

Over the past few years there has been an increasing interest in the development of robot aided minimally invasive surgery (RMIS). There are several benefits to using these systems including teleoperation, repeatable movements, and accurate positioning of tools that would otherwise require more invasive procedures. As a result patient recovery has been known to faster.

The commercially available systems, like the da Vinci robot, do not have haptic feedback built into the joysticks. Consequently, surgeons who are first learning to use the system have a steep learning curve to overcome the lack of haptic and kinaesthetic feedback they are used to when performing traditional surgery.

Thus, this application will explore recreating force feedback for RMIS teleoperation. The specific surgery used in this scenario is low dose rate prostate brachytherapy. This procedure involves steering the brachytherapy needle to the prostate under ultrasound guidance to deposit radioactive seeds that will destroy malignant cells. It has been reported that some prostate tumours are not visible through ultrasound imaging, thus making it difficult to place the seeds directly in the tumour. Consequently, some surgeons place seeds throughout the prostate such that the radiation has greater coverage and an increased chance to destroy cancer cells, undesirably irradiating healthy tissue in the process.

Since the surgeon is performing the task through teleoperation, they are unable to make use of the force feedback they would expect by inserting the needle by hand. As discussed previously, there are assorted challenges in using force sensors, but in this scenario are further complicated by needle-tissue interaction forces. It has been shown elsewhere that for needle-tissue interaction force at the base of the needle is comprised of puncturing, cutting and friction forces [102] [15], creating a non-trivial challenge in extracting only the relevant information such as tissue stiffness for haptic

feedback.

Thus, once again, it is proposed to use EIS to determine the tissue at the needle tip, and a corresponding force be generated to alert the robot operator. The following section describes how this relationship is developed and the experiments used to test its effectiveness.
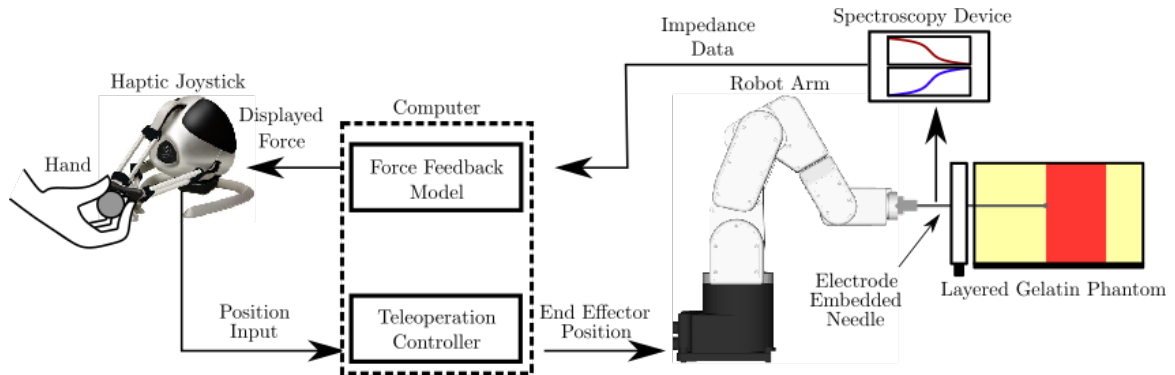
Figure 5.6: The proposed teleoperated RMIS system with force feedback setup. The user moves the handle of haptic device where the movements are transformed to movement of the robotic arm as it inserts the needle into the phantom tissue. The electrode at the tip of the needle is used by the spectroscopy device to determine the local electric impedance of the phantom. The impedance is converted to a force and displayed to the user as haptic feedback.

5.2.2 Relating Electric Impedance to Force Feedback

When comparing malignant to healthy tissues in organs, such as the prostate or breast, malignant cells are generally more stiff and have greater electric impedance [69] [103] [20] [104]. A crude model can be made, where the mechanical stiffness K is proportional to the electrical impedance $Z(\omega)$ of a given tissue,

$$K = \gamma_1 Z(\omega) \tag{5.1}$$

where γ_1 is a conversion factor. The conversion factor will differ for any given tissue and should be calibrated for the specific situation.

As mentioned above there are multiple components that contribute to the force one

would feel at the base of the needle. When recreating haptic feedback one has to determine what information they wish to recreate in the displayed force. To simplify the model, assume that the needle has already punctured the tissue, eliminating the puncturing force. As the needle is further inserted into the tissue, the surface area of the needle in contact with the tissue increases and the friction forces are observed. These friction forces can be troublesome, as they can be obscure information about tissue stiffness. Eliminating the friction component would improve the haptic feedback for tissue discrimination. Thus, only cutting forces are presented where the force at the base of the needle F is proportional to the tissue stiffness K through a factor γ_2,

$$F = \gamma_2 K \tag{5.2}$$

In combining (5.1) and (5.2) a lumped conversion factor $\gamma = \gamma_1 \gamma_2$ relates electric impedance to force,

$$F = \gamma Z(\omega) \tag{5.3}$$

It should be noted that is is not a universally applicable model. The assumption in this model is that an increase in tissue stiffness relates to an increase in electric impedance. This is not true for all tissues; cancerous cells can offer better electrical conductivity relative to healthy tissue, as seen in liver cancer [89]. Thus, the model proposed here should be adapted accordingly depending on the application.

For this scenario consider a needle with EIS electrodes at the tip that has punctured an organ which is comprised of only uniform healthy tissue with a malignant at an unknown depth. The electric impedance of the tissue at the tip can be evaluated by averaging n electric impedance measurements. To discriminate between the two tissues, the electric impedance data is compensated to be relative to the measurement immediately after puncturing into the healthy tissue. The initial electric impedance $Z(\omega, 0)$ is consequently removed from measurements at needle tip depth d. The haptic

force can then be estimated as,

$$F(d) = \gamma\Big(\frac{\sum_{i=1}^{n} Z_i(\omega, d)}{n} - Z(\omega, 0)\Big) \tag{5.4}$$

In summary, using electric impedance measurements, one can determine the local electric impedance at the tip of the needle and render that as a force F to the user. The haptic force can be scaled through a tunable parameter γ. With the relationship between the electric impedance and haptic force now developed, the following section describes the RMIS setup and phantom tissues used to test the proposed force feedback model.

5.2.3 Experiment Setup

The experimental setup used to validate the concept is shown in Figure 5.7.

The Meca500 6-DOF serial robot arm (Mecademic, Montréal, Canada) inserts an electrode embedded needle as controlled by the operator with the Novint Falcon 3-DOF parallel manipulator haptic joystick (Novint Technologies, New Mexico, USA). The impedance data gathered by a spectroscopy system is then used in the force feedback model to display a force to the user through the haptic device.

The phantom tissue was made using unflavoured porcine gelatin. Layers of gelatin were created to fabricate one of the phantoms used in testing: a cancer layer adjacent to healthy tissue on either side, refer to Figure 5.7. For the healthy tissue, a ratio of 25 grams of gelatin with 5 grams of iodized salt was added to 240 mL of water. To make the cancerous layer, the ratio used was 40 grams of gelatin to 240 mL of water.

The healthy and cancerous phantom types were prepared such that they would acquire unique mechanical and electrical properties. The stiffness of the gelatin phantoms was measured through indentation tests. The tests were repeated at set internal temperatures, as the mechanical properties of the gelatin were temperature dependent.

The Young's modulus K was determined with the relation [105] [106],

$$K = \frac{(1 - v^2)F_k}{2ax\kappa} \tag{5.5}$$

where x and F_k are the indentation depth and force, respectively, a is the radius of the cylinder indenter, and κ was taken as unity since the indenter radius was significantly smaller than the surface area of the phantom. Poisson's ratio v was approximated as 0.45, a value between the those seen in the literature, 0.4 [107] and 0.495 [108].

The Young's modulus of the phantom was determined using data from four different internal temperatures with five compressions each. The Young's modulus for the healthy tissue gelatin phantom and the cancerous gelatin phantom were determined to be 6.88 ± 0.10 kPa and 12.0 ± 0.17 kPa respectively at 14°C. These values are comparable to those obtained for gelatin phantoms in other publications [108]. The created phantoms are less stiff than actual human organs but do mirror the behaviour of prostate cancer, which has nearly twice the elastic modulus of healthy tissue [104].
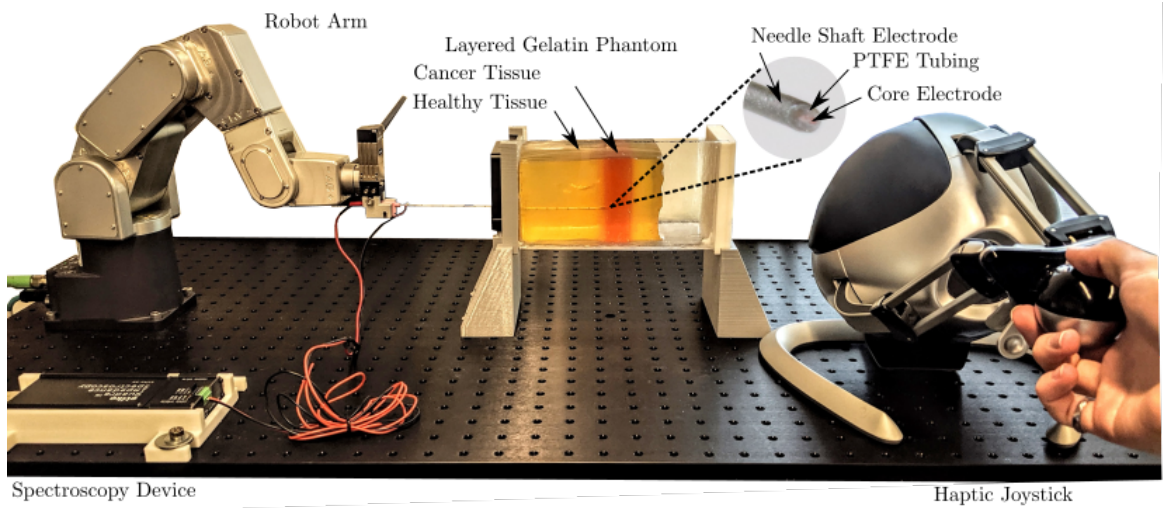

Figure 5.7: The setup for teleoperated RMIS force feedback experiment. The robotic arm (left) inserts the needle into the gelatin phantom tissue. The properties of the tissue are measured as the needle progresses into the tissue. The user controls the position of the end effector by moving the joystick of the haptic feedback device (right).

5.2.4 Experiment Results

The model formulated in (5.4) is integrated in the system shown in Figure 5.7. The complete results of the experiment are in shown in Figure 5.9.

An unmodified 18 gauge brachytherapy needle was attached to a load cell to determine the axial insertion force, see Figure 5.9 (b). This plot is representative of the force the surgeon would feel by inserting the needle by hand. The components of the needle-tissue interaction are clearly visible: cutting, friction and puncturing. Noticeably, the slope of the force increases while transitioning into the cancer phantom. This is a result of the increased stiffness created by altering the water to gelatin ratio in the phantom fabrication for the respective layers. The overall difference in force seen along the needle depth is relatively inappreciable, which would make it difficult to distinguish between the tissue types while inserting by hand. Thus, for the haptic feedback RMIS scenario, it is prudent that the force be more discernible for the transition into the cancer layer.

Figure 5.9(a) showcases the difference in electric impedance of the gelatin layers with respect to an alternating frequency ω through EIS measurements. The addition of salt in the healthy gelatin resulted in a distinctly different conductivity compared to the cancerous layer.

In the RMIS control loop the magnitude of the phantom's electric impedance at the needle tip was determined by averaging $n = 10$ spectra samples. The electric impedance at lower frequencies provided the greatest relative difference in the tissue types as shown in Figure 5.9(a). In an effort to achieve responsive force feedback, it is critical that the tissue be classified quickly. To accomplish this a significantly simpler approach is taken rather than fitting the data to a circuit model and extracting the parameter values. The magnitude of the electric impedance at a single frequency, $\omega = 1$ kHz, was used in calculating the displayed force in (5.4).

The electrode embedded needle was inserted into the tissue and the impedance at a

given depth was recorded, see Figure 5.9(c). These impedance values are evaluated as a force to be displayed to the user as shown in Figure 5.9(d). For any $F(d) < 0$ was taken as $F(d) = 0$, otherwise the haptic device would pull the user in rather than impede their insertion. Furthermore, to provide a safe limit to the displayable force any $F(d) > F_{max}$ was set such that $F(d) = F_{max}$. In comparison to (b), the force is significantly more noticeable during the transition into the cancer phantom.

The results of the experiment suggested that the haptic feedback would be more detectable than inserting the needle manually. User trials conducted to confirm this theory are discussed in the following section.
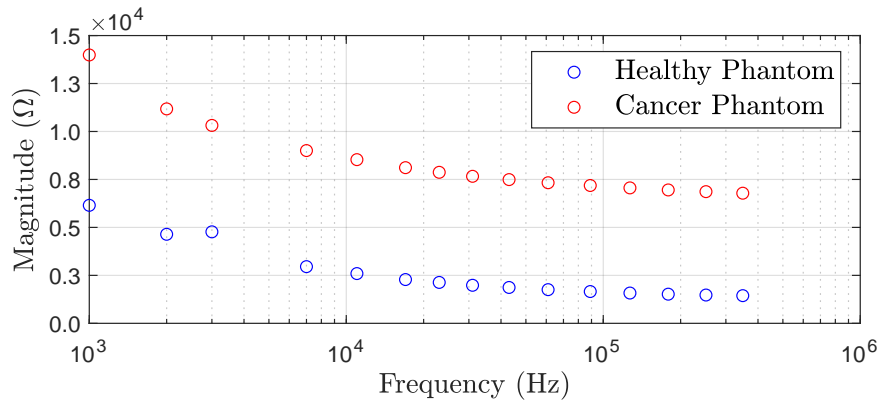
Figure 5.8: The difference in the electric impedance can be seen clearly. The lower concentration of salt enables the cancerous phantom to have a higher impedance than the healthy phantom.
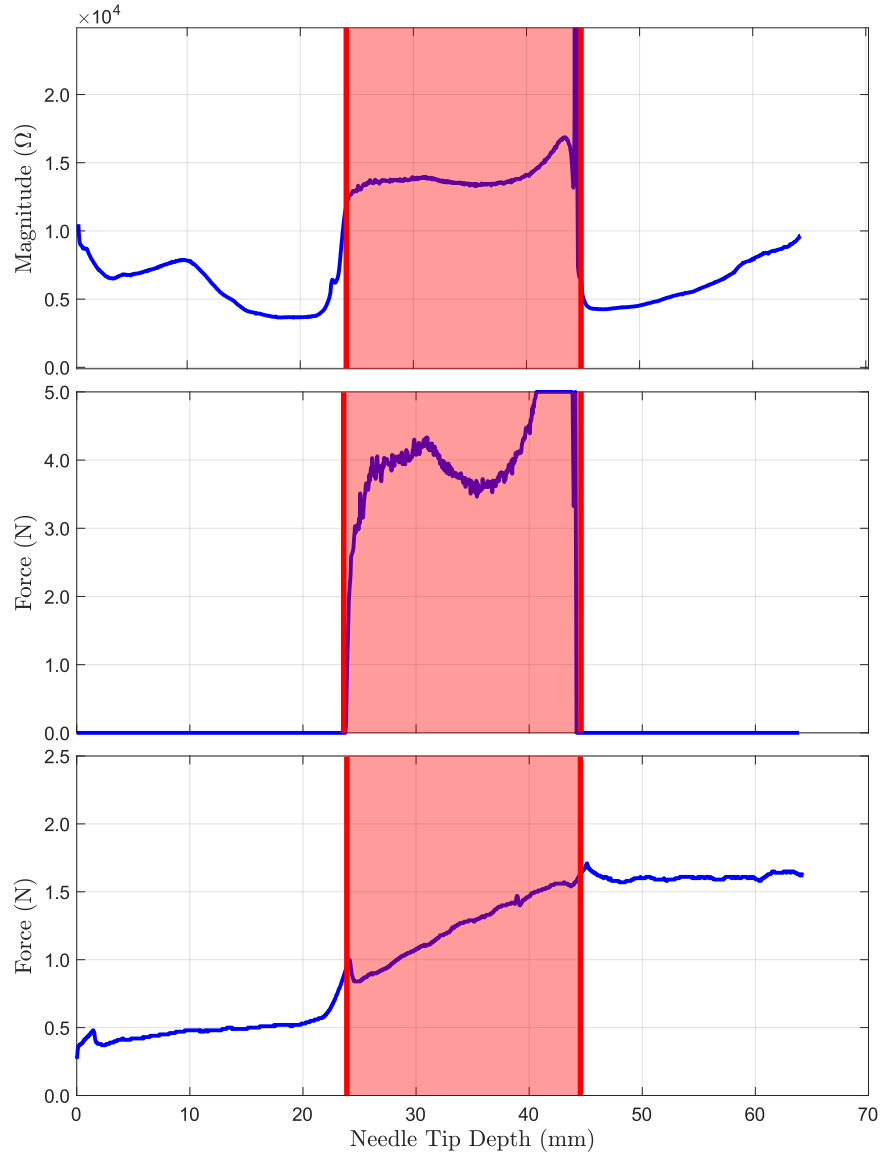
Figure 5.9: Measured properties during insertion of the electrode embedded needle into the layered phantom. The top plot illustrates the measured electric impedance magnitude at the tip of the needle with respect to insertion depth. The middle plot shows what the force the haptic device should deliver to the user through (5.3), at a given depth in the phantom. The bottom plot depicts the force measured by the load cell at the base of the needle during insertion. The shaded region represents the cancer layer of the phantom.

5.2.5 User Trial Study: Setup

An additional study was conducted to test if the developed haptic feedback method was applicable to in a practical test. A set of user trials were designed to mimic a surgeon inserting a needle during percutaneous brachytherapy. First, the user would

insert the needle by hand into unique phantoms, see Figure 5.10(a). Following this, a robot arm wields the needle probe at the end effector, which the user would control through the haptic device, where they would detect the force based on the developed method, see Figure 5.10(b). The participant's objective was to determine where the cancer layer existed in the hidden gelatin phantom using only force feedback. In the hand trial the user would stop inserting the needle when they perceived the cancer layer, and leave it within the tissue. In the teleoperated test, the user would press a button on the haptic device handle to signal their perceived change in tissue and record the needle tip depth.

Multiple phantoms were used with the cancer layer at different depths. The test participant was unable to view any of the phantoms so they had to rely only on force feedback. The participant would insert the electrode embedded needle into the phantom through a traditional brachytherapy grid template.

These user trials consisted of 16 participants. All participants were given the same set of written instructions prior to the start of the test. Each participant was shown an example gelatin phantom that they could practice with hand insertion to familiarise themselves with the needle force associated with the healthy and cancerous layers of the gelatin. Additionally, a simulated force was presented to the user in the haptic device such that they could recognise the haptic force they were to expect in the actual trials. Each participant was only permitted one insertion per phantom.

5.2.6 User Trial Study: Results

Figure 5.11 shows the final depths that the user perceived the cancer for both tests in each of the phantoms. The teleoperated trials performed significantly better than the hand trials overall. The hand trials were more successful at finding the cancer layer in Phantom 2, where the layer was at a shallow depth. It is speculated that the users had more difficulty in Phantom 1 and Phantom 3 hand trials due to the amount of friction experienced. In the teleoperation scenario, friction is eliminated, since the haptic device only displayed a force from the electric properties of the phantom, which

(a)   (b)

Figure 5.10: The two stages of the user trials. (a) The test participant would first insert the needle by hand to determine the depth of the cancer layer in the unique phantoms. (b) The participant would then determine the depths using haptic feedback in the teleoperated scenario.

may explain the increase in performance.

Many of the teleoperated results show final depths recorded before the transition line. This perceived preemptive stop is likely caused by two things. First, while the gelatin layers were prepared separately, when combined in the phantom, the salt ions diffuse gradually into the non-salinated layer which alters the local conductivity near the layer transition. Second, the haptic force pushes against the user, causing them to unintentionally move the joystick handle slightly outward and consequently move the needle out of the cancer. For the latter it can be seen in the Phantom 2 and Phantom 3 results that the users more readily anticipate the haptic force and become more consistent in stopping within the cancer layer.

The average depth with standard deviation for each of the phantoms in the two test scenarios are listed in Table 5.1 along with the percentage of trials that successfully finished within the cancer layer.

Table 5.1: User Trial Statistics (Units are in [mm])

	Phantom 1		Phantom 2		Phantom 3	
	Cancer Start:	112.5	Cancer Start:	56.0	Cancer Start:	94.5
	Cancer End:	134.5	Cancer End:	78.0	Cancer End:	116.5
	Avg Depth	**Success**	**Avg Depth**	**Success**	**Avg Depth**	**Success**
Test 1: Hand	74.9 ± 18.5	0%	61.7 ± 11.1	78%	72.5 ± 15.5	6%
Test 2: Robot	109.1 ± 9.1	25%	59.9 ± 11.3	75%	96.6 ± 4.3	81%
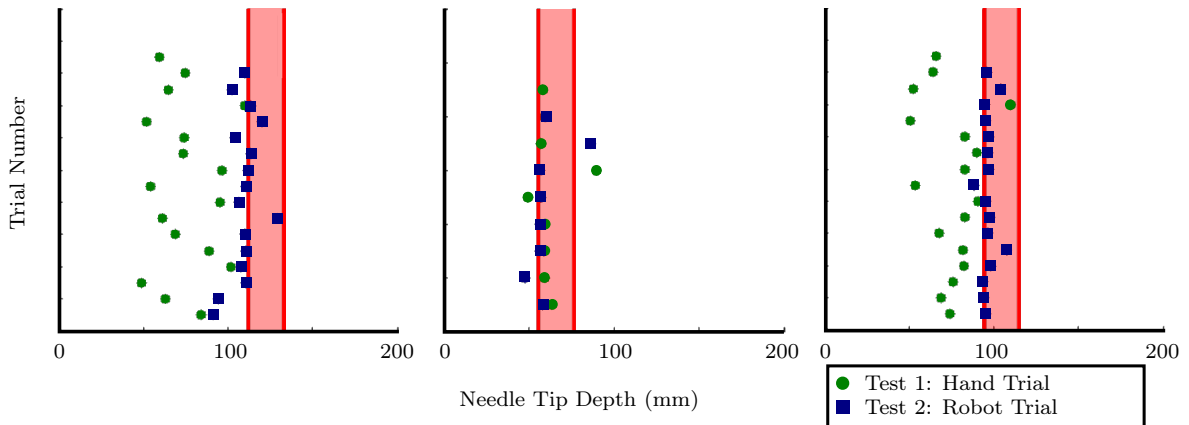
Figure 5.11: Results of the user trials in each of the phantoms. The shaded region represents the cancer layer of the phantom.

5.2.7 Discussion: Outcome of the Application

Implementing traditional force sensors on needles for haptic force feedback in tele-operated RMIS is not a trivial task. This scenario introduces an alternative sensor through analysis of a tissue's electric impedance. The user trials and experimental results indicate that the addition of haptic feedback derived from the spectroscopy data improved the operators ability to detect where the cancer layer started in the phantom tissue. The proposed method of using electric impedance to display haptic feedback may hold new possibilities in several medical procedures including percutaneous brachytherapy, nephrolithotomy, angioplasty and stereotactic surgeries.

The developed model for this application is rudimentary due to the controlled composition of the phantom tissues. Further development could be performed using the classification methods discussed in the previous chapters of this manuscript to classify more complex and realistic tissues.

Chapter 6

Manuscript Conclusion

6.1 Summary of Presented Work

This thesis explores an opportunity to improve some of the surgical procedures currently being performed under robotic assistance. Specifically, this thesis contributes to a larger goal of differentiating tissue types from its surroundings in minimally invasive surgeries like biopsy and brachytherapy. Robot assisted minimally invasive surgery has been increasingly used as a means of improving surgical procedures, including the aforementioned. The lack of force and tactile feedback in the commercially available robot systems pose difficulties for novice practitioners. The addition of haptic feedback can replace lost sensations when performing the operation remotely through teleoperation. Thus, the incorporation of haptic feedback into these devices has been a field of great interest in recent years. There have been attempts at installing sensors in surgical instruments to determine what type of feedback should be sent to the user. Deriving haptic feedback from force sensors on the surgical tools pose several challenges.

An alternative approach for the design of a new tool was introduced in Chapter 2, where the electrical properties are used instead of using the mechanical properties of the tissue. A coaxial electrode arrangement is integrated into a surgical needle and combined with a multi-frequency electric impedance analyser to perform electric impedance spectroscopy on the tissue at the needle tip. The literature has shown that cancerous tissue can be identified from its healthy counterpart by analysing the electric impedance. A hand crafted prototype of the tool was made and to validate its functionality, was used to measure the electric impedance of many tissues, including gel-based phantoms, ex-vivo organs, and freshly excised tissues from a veterinarian clinic, as a surrogate for healthy and cancerous tissues. The measurements for these samples confirmed that, for some tissues, one could use the electric impedance to identify and differentiate them.

The electric impedance of tissues has been a subject of interest for decades. Throughout the years, researchers have fit electric impedance data to models to help char-

acterise and study them. A popular approach is to develop an equivalent circuit of well recognised circuit elements like resistors and capacitors, that have a similar impedance spectrum to that of the measured tissue. An assortment of these models were explored in Chapter 3 of this thesis. The double-dispersion Cole model provided a flexible model that could be used for the variety of impedance spectra seen in the tissue samples. The remainder of the chapter proposed and validated different algorithms for determining the values for the double-dispersion Cole model. Deterministic and stochastic approaches were considered, as each have their own strengths. The deterministic method, Newton-Raphson, is a relatively fast optimisation process, but is not guaranteed to converge on a solution and has a heavy dependence on the initial conditions of the model parameters. The stochastic method, RPD-NSGA-II, has the advantage of exploring many possible solutions but at the added cost of computation time.

In order for haptic feedback to be sent to the user, the tissue needs to be classified from the EIS data. Chapter 4 introduced several classification methods, and compared their effectiveness. The classifiers ranged from simply comparing the measured electric impedance to the advanced methods that evaluated probabilities of the fit circuit model element values. Weighted variants of these classifiers were investigated, where defining features were determined through optimisation methods. The least square error classifier was the most accurate in the experiments and could be executed quickly, but is not robust, as it is susceptible to incorrectly classifying samples with impedance similar of any sample of another tissue. The k-Nearest Neighbours algorithm aimed to improve upon the shortcomings of the former method, but suffered in its accuracy. The Naïve Bayes classifiers utilised probabilities for classification but needed to have tissue groups separated to have a high accuracy.

The combination of developments in the prototype tool, equivalent circuit model and classifier culminated in Chapter 5 to implement haptic feedback in needle-based applications: in teleoperated RMIS and vibrotactile manual insertion. Vibrotactile feedback had potential in communicating the tissue composition to the user. Unique

and distinguishable vibration patterns were developed and tested with user trials. However, it was found that this is difficult to achieve with only the one vibration motor installed at the base of the needle. Nonetheless, the results of the black-box tissue identification study, where users had to identify gelatin phantoms using the electrode embedded needle and only vibrotactile feedback, showed the method was successful in differentiating tissues with different impedance.

Force feedback, on the other hand, showed promise in a simulated teleoperated robot assisted surgery. The electrode embedded needle was wielded by a robotic arm, which was controlled by an operator through a haptic force feedback joystick. The electric impedance sensed at the needle tip was converted into a corresponding force to be displayed to the user through a rudimentary model. A set of experiments conducted had users try to find the depth of a tumour in gelatin phantoms by manually inserting a needle by hand and then with the force feedback from EIS system. The trials showed that users were more accurate in placement of the needle in a phantom when using the feedback than they were with manual insertion.

6.2   Future Work

The proposed methods and developed prototype can be improved upon, and could consist of:

- The bore of the developed prototype needle is currently blocked, which prevents it from performing surgical functions. Refinement of the prototype electrode embedded needle, including miniaturising the electrodes such that they do not interfere with its primary function as seen in [25] [26] [109] is recommended.

- Measurements with actual healthy and cancerous tissues of varying malignancy. It is yet to be seen if the methods discussed in this manuscript are able to detect the differences in the impedance for these tissues, most notably in-vivo. A large number of samples are required to form effective databases and enable meaningful analysis of the data.

- The combination of the developed systems is currently not feasible for real-time haptic feedback. Currently, the combination of the Quadra measurement for 23 frequencies, Newton-Raphson model fitting and Naïve Bayes classification take 3.05 seconds to execute. Finding efficiencies in the measurement, model fitting and classifier that could enable the entire system to be used in real-time.

- The features used for classification in this thesis produced less than desired performance. This thesis focused on the comparison of either measured impedance or model parameter values exclusively. It is recommended to investigate features from the electric impedance spectra beyond those discussed here. Some merit may be seen in comparing the calculated impedance from the fit model. Alternative classification features such as critical frequencies, physical characteristics of the patient such as age or otherwise may all be useful in improving the classification measurement.

- This thesis provided examples of two haptic feedback applications, which limits the proof of the system's effectiveness. It would be beneficial to explore additional methods of haptic feedback that may outperform those described here including multiple motors in vibrotactile feedback, or the combination of vibrotactile feedback with force feedback.

Beyond the immediate recommendations there are many directions this work could expand into. Perhaps the most promising is the further development of sensorized needles. Yu et al. have recently implemented piezoelectric sensors on a surgical needle to measure the elastic modulus of tissues to great success in differentiating tissues [110]. With the specific application of prostate cancer in mind, tests that monitors prostate-specific antigen (PSA) have been used clinically for assessing malignancy. PSA detection with the combination of EIS has been studied before [111]. It is exciting to consider the combination of these sensing technologies on the same needle, which could provide simultaneous PSA information, mechanical and electrical impedance data of the tissues.

This thesis investigated the use-cases of force and vibrotactile feedback separately. It is worthwhile to note that information can be communicated in additional ways, such as audible or visual feedback. The findings in [112] reported that users responded favourably to the use of multi-modal feedback: a combination of visual, audible and vibrotactile haptic feedback. A future avenue to explore could involve multi-model feedback with the sensorized needle that could simultaneously sample force and electric impedance measurements. For instance, consider the haptic joystick shown in Figure 5.7 with a vibration motor installed in the handle. The force feedback could be proportional to the force measurements, and vibrotactile feedback could be determined by tissue classification from electric impedance measurements. Another example where multiple sources of haptic feedback could enhance the user perception include expanding the force feedback to three degrees of freedom. With multiple piezoelectric sensors along the needle shaft the haptic feedback could recreate the sensation of the needle surrounded by tissue.

Lastly, the methods proposed in this thesis could be reinforced by increasing the number of tissue samples and number of participants in the haptic feedback trials. The number of tissues sampled has shown that it is possible to differentiate some tissues by their electric impedance, but an increase in the number of samples would enable one to test the robustness of the classifiers through methods such as cross-validation. Concerning the number of participants in the haptic feedback trials, it is important to note the variance in user perception to haptic feedback. Studies have shown that factors like age [112] [113] and gender [113] could influence the perception of haptic feedback.

6.3   Concluding Statements

For further reading the author highly recommends the book by Martinsen and Grimnes [35]. The text covers all facets of the topics discussed in this thesis including the history of bioimpedance, equivalent models, classification, and more.

In conclusion, this thesis presents a haptic feedback integrated surgical needle tool that could determine the tissue at the needle tip through electric impedance spectroscopy. The prototype was able to differentiate an assortment of tissues through their electric impedance. The biosensor was reliable in the application experiments where haptic feedback was used. Thus, the proposed methods may one day contribute to improving the surgical procedures used today.

Appendix A

Impedance Plots of Tissue

Figure A.1: Impedance magnitude and phase for 22 canine and feline testicle samples. Right figure captures the impedance from 1 kHz to 349 kHz, to call attention to the deviation of the impedance not easily seen in the left figure.

Figure A.2: Impedance magnitude and phase for 22 canine and feline ovary samples. Right figure captures the impedance from 1 kHz to 349 kHz, to call attention to the deviation of the impedance not easily seen in the left figure.
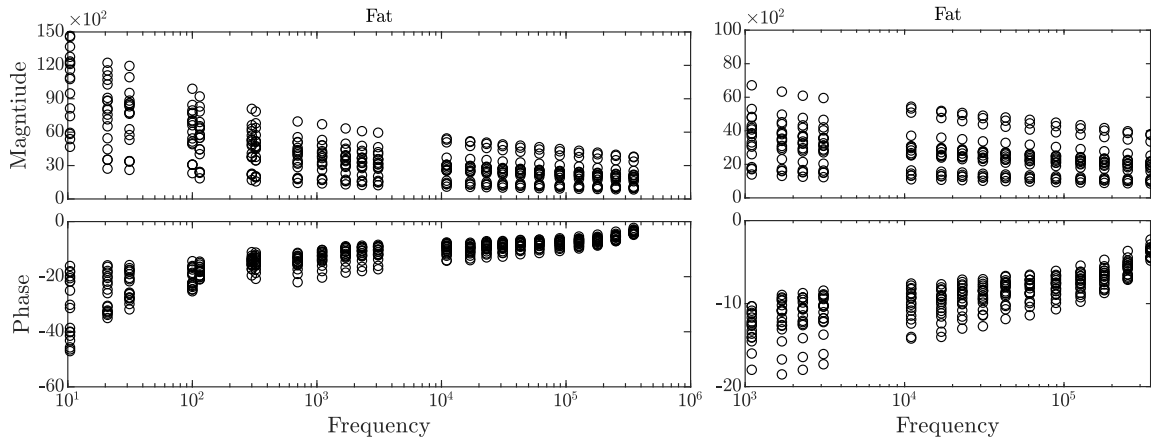
Figure A.3: Impedance magnitude and phase for 18 fat samples. Right figure captures the impedance from 1 kHz to 349 kHz, to call attention to the deviation of the impedance not easily seen in the left figure.
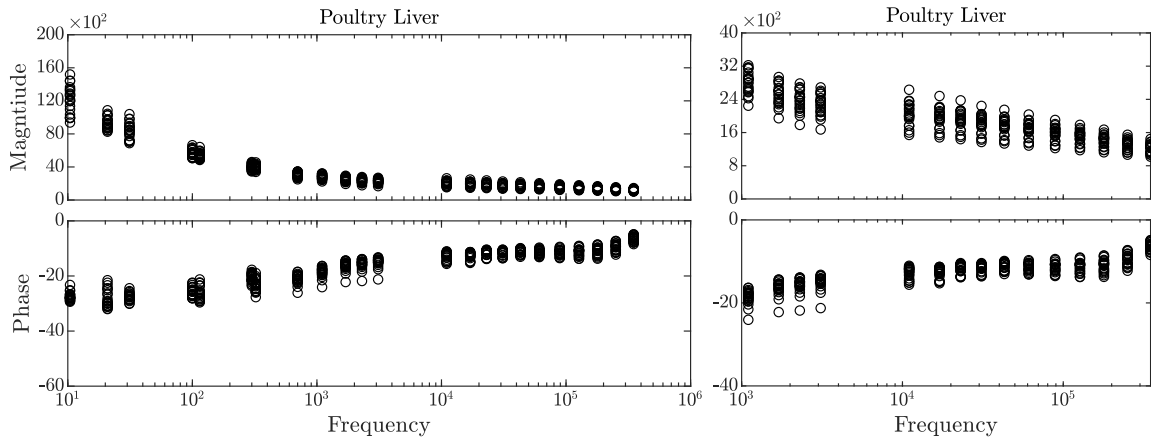
Figure A.4: Impedance magnitude and phase for 22 poultry liver samples. Right figure captures the impedance from 1 kHz to 349 kHz, to call attention to the deviation of the impedance not easily seen in the left figure.
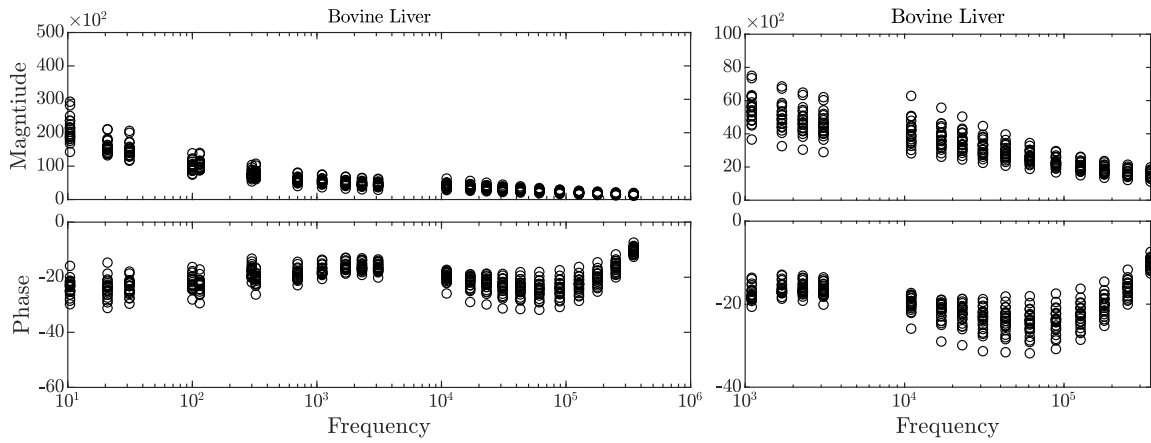
Figure A.5: Impedance magnitude and phase for 22 bovine liver samples. Right figure captures the impedance from 1 kHz to 349 kHz, to call attention to the deviation of the impedance not easily seen in the left figure.
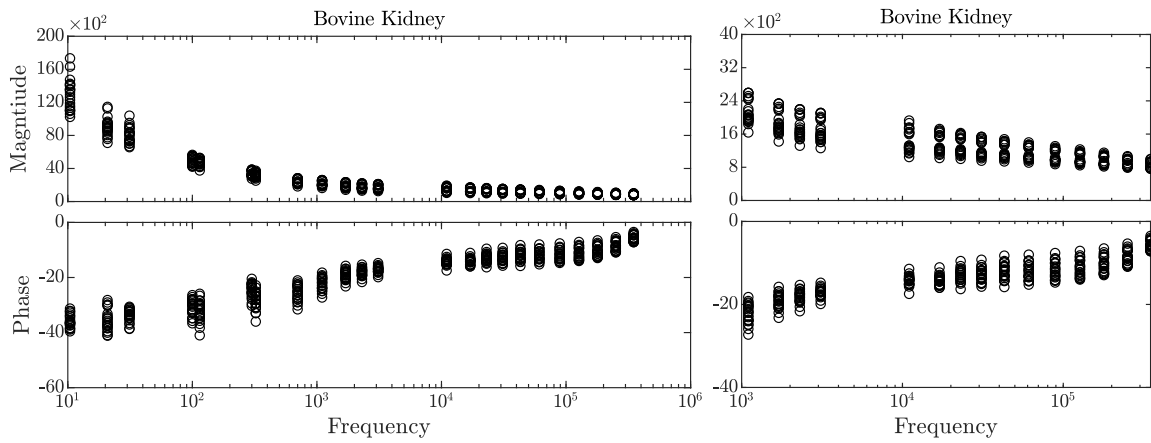
Figure A.6: Impedance magnitude and phase for 22 bovine kidney samples. Right figure captures the impedance from 1 kHz to 349 kHz, to call attention to the deviation of the impedance not easily seen in the left figure.
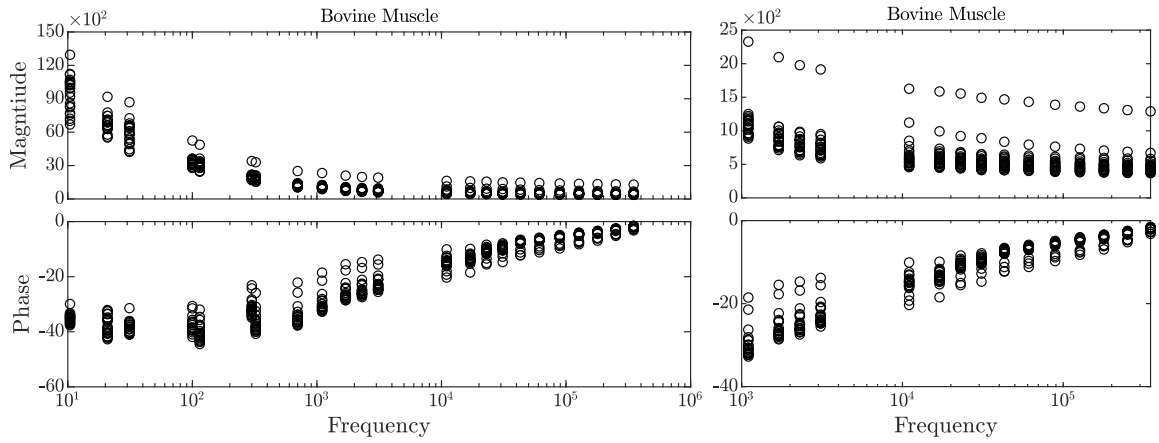
Figure A.7: Impedance magnitude and phase for 22 bovine muscle samples. Right figure captures the impedance from 1 kHz to 349 kHz, to call attention to the deviation of the impedance not easily seen in the left figure.
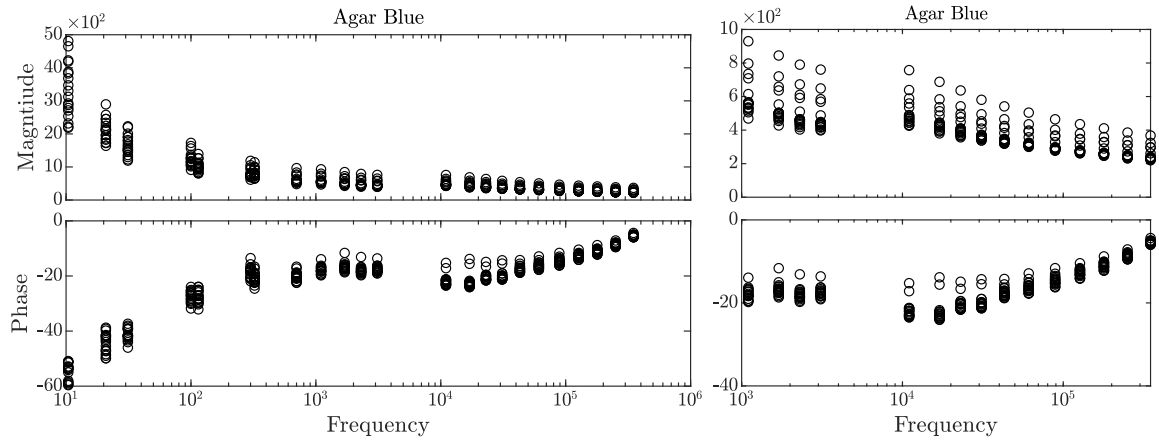
Figure A.8: Impedance magnitude and phase for 18 agar (Blue) samples. Right figure captures the impedance from 1 kHz to 349 kHz, to call attention to the deviation of the impedance not easily seen in the left figure.
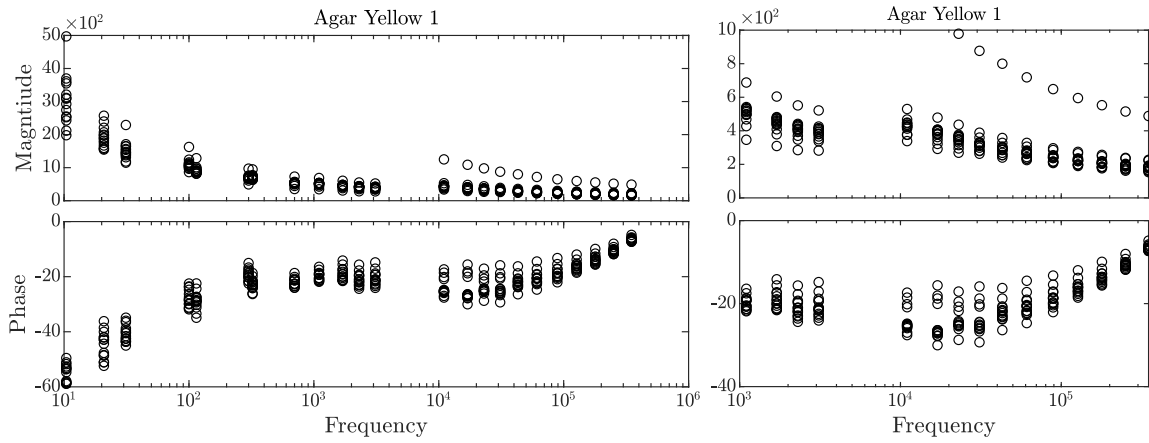
Figure A.9: Impedance magnitude and phase for 14 agar (Yellow 1) samples. Right figure captures the impedance from 1 kHz to 349 kHz, to call attention to the deviation of the impedance not easily seen in the left figure.
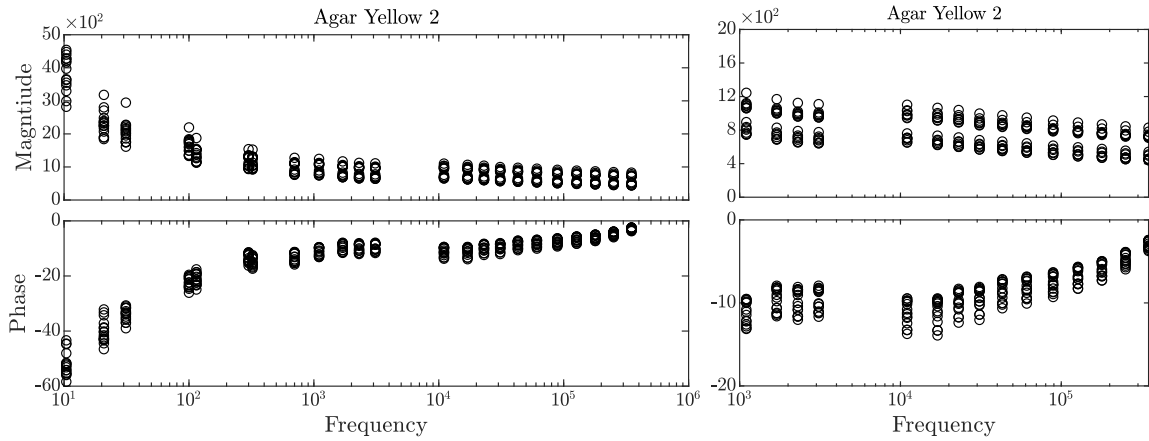
Figure A.10: Impedance magnitude and phase for 16 agar (Yellow 2) samples. Right figure captures the impedance from 1 kHz to 349 kHz, to call attention to the deviation of the impedance not easily seen in the left figure.
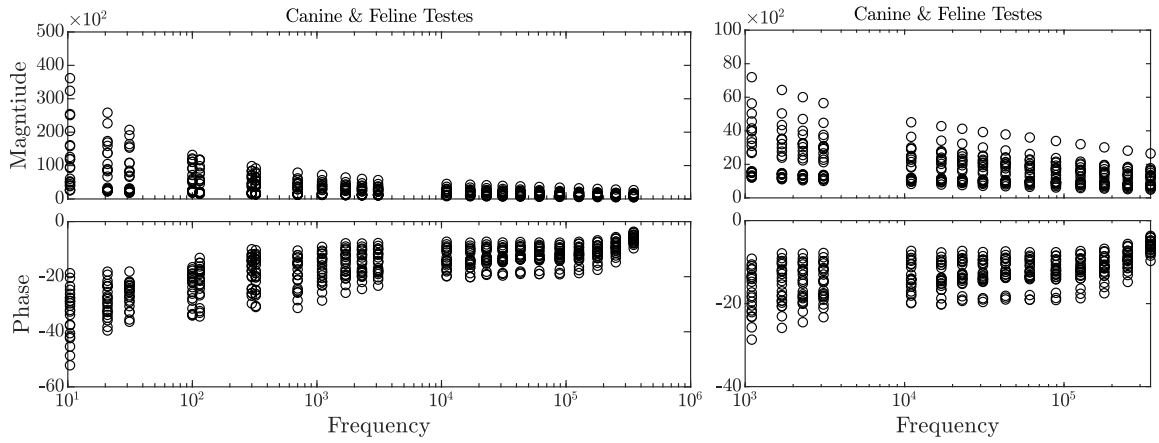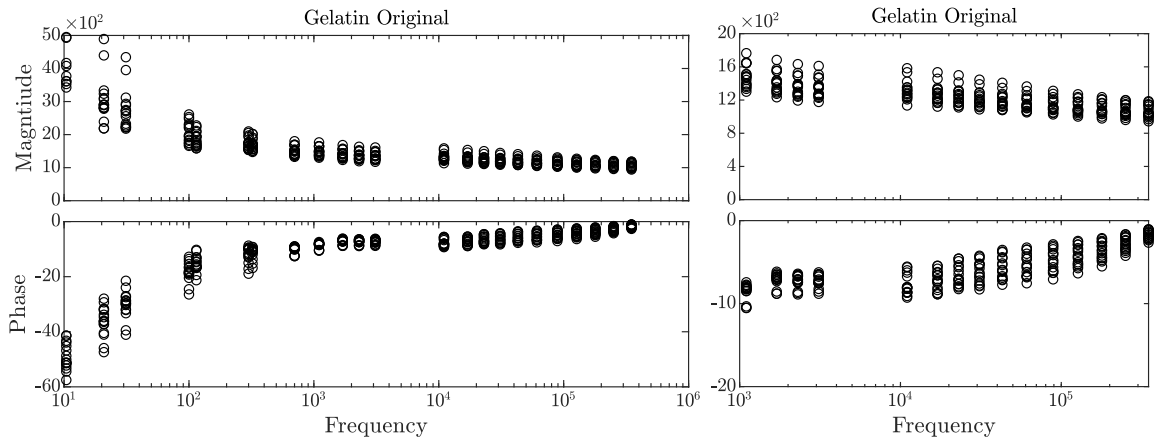
Figure A.11: Impedance magnitude and phase for 16 gelatin (Original) samples. Right figure captures the impedance from 1 kHz to 349 kHz, to call attention to the deviation of the impedance not easily seen in the left figure.
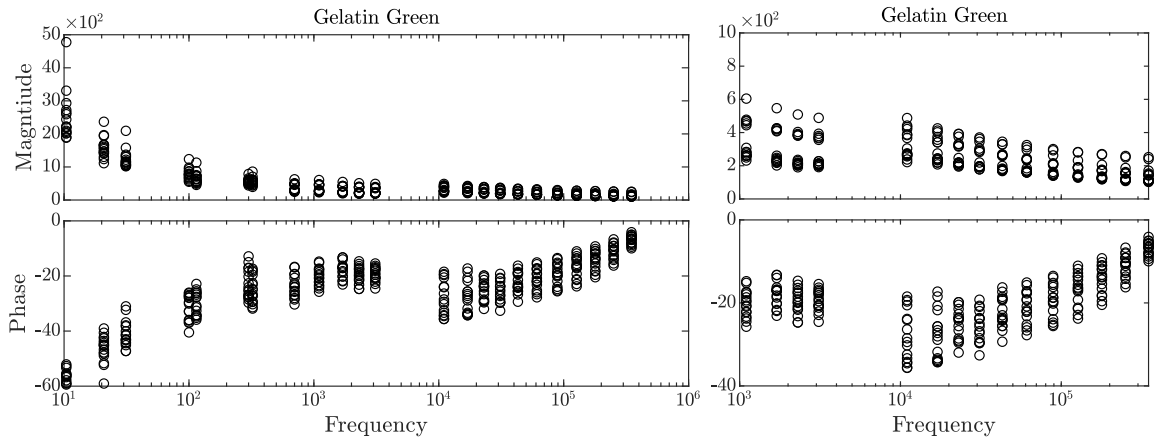
Figure A.12: Impedance magnitude and phase for 16 gelatin (Green) samples. Right figure captures the impedance from 1 kHz to 349 kHz, to call attention to the deviation of the impedance not easily seen in the left figure.
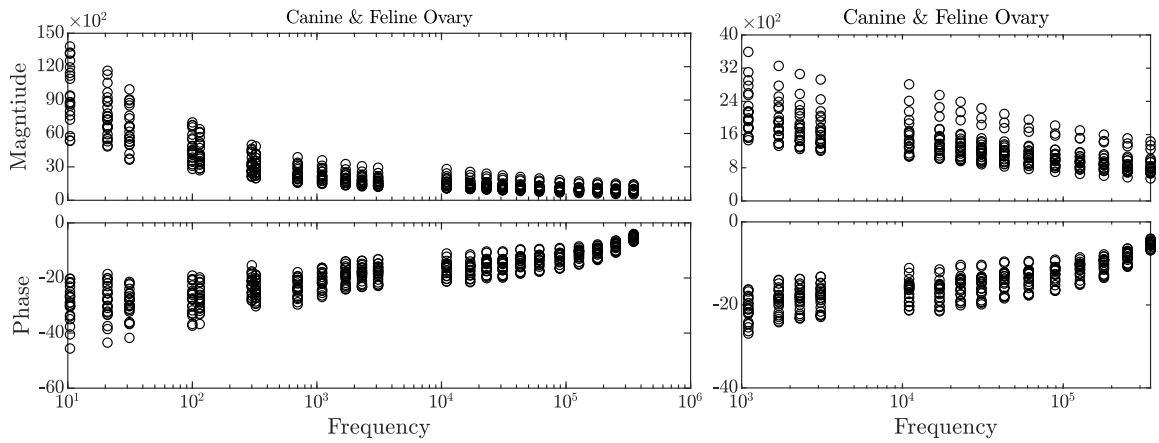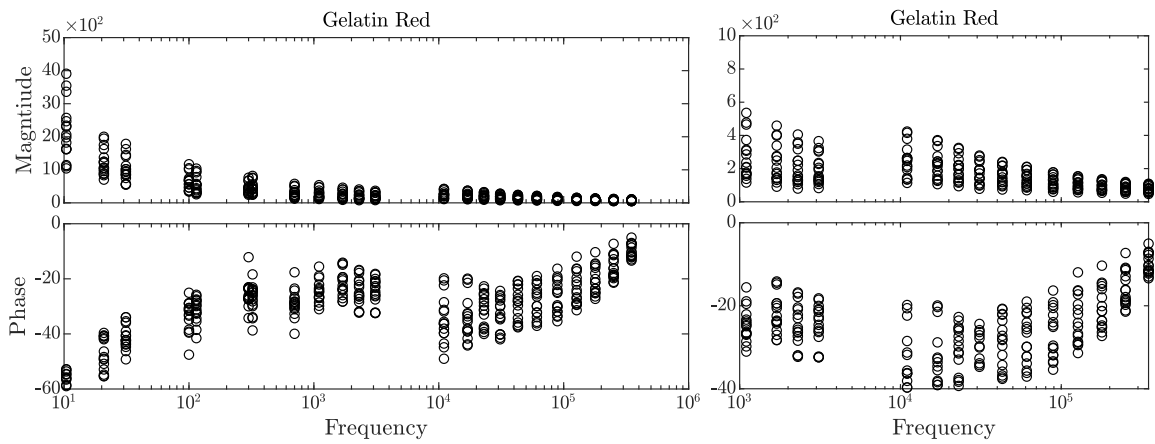
Figure A.13: Impedance magnitude and phase for 16 gelatin (Red) samples. Right figure captures the impedance from 1 kHz to 349 kHz, to call attention to the deviation of the impedance not easily seen in the left figure.

Appendix B

Impedance Values for Tissue Samples

Table B.1: Average Value & Standard Deviation of the Impedance Magnitude at 23 Frequencies for All Tissue Samples

Tissue	10.4 Hz	20.8 Hz	31.3 Hz	100 Hz	114.6 Hz
Bovine Liver	20859 ± 3450	15983 ± 2114	14896 ± 2214	10002 ± 1524	10328 ± 1405
Poultry Liver	12208 ± 1579	9275 ± 693	8421 ± 950	5727 ± 405	5418 ± 377
Bovine Muscle	9475 ± 1575	6832 ± 762	5933 ± 1033	3309 ± 498	3123 ± 483
Bovine Kidney	12971 ± 1793	9043 ± 1022	8083 ± 951	4947 ± 437	4727 ± 375
Ovary	9987 ± 2825	7622 ± 1958	6449 ± 1740	4727 ± 1219	4243 ± 1094
Testes	12193 ± 9755	8923 ± 7071	7822 ± 5993	5897 ± 3909	5227 ± 3629
Gelatin (Original)	5048 ± 1635	3045 ± 687	2753 ± 601	2063 ± 306	1856 ± 218
Gelatin (Green)	2501 ± 704	1588 ± 297	1238 ± 265	782 ± 166	658 ± 162
Gelatin (Red)	2158 ± 834	1237 ± 387	1020 ± 362	635 ± 249	541 ± 247
Agar (Yellow 1)	3036 ± 743	1925 ± 297	1514 ± 268	1101 ± 170	923 ± 115
Agar (Yellow 2)	3979 ± 718	2326 ± 340	2058 ± 302	1636 ± 226	1391 ± 196
Agar (Blue)	3317 ± 798	2128 ± 319	1656 ± 301	1244 ± 210	1024 ± 155
Fat	10467 ± 3388	7758 ± 2829	7136 ± 2618	5962 ± 2059	5336 ± 2082

Tissue	300 Hz	322.9 Hz	700 Hz	1.1 kHz	1.7 kHz	2.3 kHz
Bovine Liver	7556 ± 1129	7724 ± 1135	5904 ± 921	5491 ± 868	5017 ± 809	4748 ± 769
Poultry Liver	4004 ± 308	3951 ± 263	3034 ± 260	2803 ± 254	2519 ± 248	2368 ± 244
Bovine Muscle	2022 ± 342	1889 ± 345	1283 ± 291	1113 ± 286	926 ± 275	839 ± 267
Bovine Kidney	3386 ± 314	3224 ± 289	2378 ± 282	2148 ± 279	1897 ± 273	1771 ± 263
Ovary	3237 ± 842	3015 ± 783	2364 ± 616	2154 ± 550	1909 ± 483	1774 ± 447
Testes	4185 ± 2640	3868 ± 2440	3164 ± 1872	2906 ± 1656	2604 ± 1441	2435 ± 1328
Gelatin (Original)	1741 ± 175	1694 ± 170	1514 ± 134	1485 ± 128	1410 ± 121	1365 ± 117
Gelatin (Green)	566 ± 79	567 ± 106	369 ± 114	349 ± 112	309 ± 106	286 ± 100
Gelatin (Red)	434 ± 149	451 ± 179	290 ± 134	271 ± 127	232 ± 111	209 ± 99
Agar (Yellow 1)	698 ± 98	714 ± 77	531 ± 77	508 ± 71	450 ± 62	410 ± 56
Agar (Yellow 2)	1174 ± 182	1162 ± 172	975 ± 165	952 ± 163	889 ± 161	852 ± 159
Agar (Blue)	804 ± 141	805 ± 126	625 ± 120	599 ± 115	538 ± 105	498 ± 99
Fat	4564 ± 1698	4392 ± 1714	3763 ± 1428	3573 ± 1358	3319 ± 1272	3165 ± 1221

Tissue	3.1 kHz	11 kHz	17 Hz	23 kHz	31 kHz	43 kHz
Bovine Liver	4554 ± 735	4118 ± 786	3771 ± 670	3497 ± 587	3189 ± 513	2906 ± 439
Poultry Liver	2275 ± 244	2048 ± 264	1959 ± 240	1895 ± 225	1806 ± 212	1747 ± 199
Bovine Muscle	791 ± 264	656 ± 259	628 ± 240	609 ± 231	578 ± 225	567 ± 218
Bovine Kidney	1691 ± 256	1433 ± 258	1365 ± 223	1315 ± 202	1244 ± 190	1197 ± 170
Ovary	1688 ± 419	1549 ± 445	1446 ± 399	1372 ± 370	1281 ± 345	1219 ± 322
Testes	2323 ± 1240	1957 ± 985	1855 ± 915	1780 ± 869	1682 ± 814	1612 ± 773
Gelatin (Original)	1348 ± 114	1317 ± 112	1273 ± 105	1246 ± 102	1217 ± 96	1192 ± 92
Gelatin (Green)	278 ± 93	330 ± 83	298 ± 75	274 ± 72	249 ± 68	228 ± 63
Gelatin (Red)	198 ± 85	248 ± 94	221 ± 81	199 ± 70	175 ± 61	156 ± 51
Agar (Yellow 1)	391 ± 51	485 ± 217	431 ± 187	393 ± 167	357 ± 147	326 ± 135
Agar (Yellow 2)	840 ± 158	848 ± 158	814 ± 159	790 ± 158	757 ± 152	737 ± 152
Agar (Blue)	480 ± 95	502 ± 84	457 ± 76	424 ± 70	389 ± 63	364 ± 59
Fat	3074 ± 1188	2875 ± 1293	2762 ± 1224	2681 ± 1183	2576 ± 1141	2504 ± 1108

Tissue	61 kHz	89 kHz	127 kHz	179 kHz	251 kHz	349 kHz
Bovine Liver	2600 ± 371	2286 ± 317	2031 ± 276	1817 ± 246	1632 ± 226	1497 ± 211
Poultry Liver	1672 ± 186	1580 ± 170	1496 ± 154	1408 ± 138	1313 ± 121	1231 ± 108
Bovine Muscle	550 ± 211	531 ± 205	519 ± 200	509 ± 196	498 ± 192	491 ± 189
Bovine Kidney	1139 ± 153	1072 ± 136	1015 ± 119	959 ± 103	901 ± 88	854 ± 76
Ovary	1148 ± 299	1071 ± 277	1011 ± 259	957 ± 244	904 ± 231	864 ± 220
Testes	1527 ± 725	1428 ± 673	1344 ± 627	1261 ± 583	1176 ± 539	1108 ± 503
Gelatin (Original)	1166 ± 87	1138 ± 82	1115 ± 78	1094 ± 75	1075 ± 73	1060 ± 72
Gelatin (Green)	212 ± 57	189 ± 54	173 ± 50	160 ± 48	148 ± 46	140 ± 45
Gelatin (Red)	141 ± 44	120 ± 37	106 ± 30	95 ± 26	84 ± 22	77 ± 19
Agar (Yellow 1)	299 ± 119	271 ± 108	250 ± 99	232 ± 92	216 ± 85	205 ± 81
Agar (Yellow 2)	714 ± 149	685 ± 145	664 ± 143	644 ± 142	624 ± 140	609 ± 139
Agar (Blue)	341 ± 54	315 ± 50	297 ± 47	281 ± 44	264 ± 42	253 ± 40
Fat	2418 ± 1070	2321 ± 1030	2238 ± 994	2156 ± 955	2070 ± 914	1997 ± 876

Table B.2: Average Value & Standard Deviation of the Impedance Phase at 23 Frequencies for All Tissue Samples

Tissue	10.4 Hz	20.8 Hz	31.3 Hz	100 Hz	114.6 Hz
Bovine Liver	−23.7 ± 2.9	−24 ± 3.5	−23.6 ± 2.8	−21.9 ± 2.6	−22.9 ± 2.5
Poultry Liver	−27.5 ± 1.4	−28.2 ± 3.2	−27.6 ± 1.4	−25.6 ± 1.7	−26.3 ± 2.4
Bovine Muscle	−35.1 ± 1.7	−37.7 ± 3.5	−38.5 ± 2.2	−37.7 ± 2.7	−40.1 ± 3.1
Bovine Kidney	−35.7 ± 2.3	−35.4 ± 3.8	−33.8 ± 2.3	−30.7 ± 2.9	−32.2 ± 3.7
Ovary	−29.2 ± 6.4	−28.4 ± 6.4	−29.4 ± 5	−27.6 ± 5.1	−27.5 ± 4.4
Testes	−33.3 ± 8.8	−28.7 ± 5.9	−26.6 ± 4.6	−23.8 ± 5.5	−22.1 ± 6.2
Gelatin (Original)	−49 ± 4.7	−36.2 ± 5.3	−30.2 ± 4.7	−18.2 ± 3.5	−15.3 ± 2.8
Gelatin (Green)	−57.8 ± 3.5	−46.4 ± 4.8	−41.1 ± 4.6	−31.3 ± 4.6	−29.8 ± 4.1
Gelatin (Red)	−58.6 ± 4.4	−48.1 ± 6.5	−41.1 ± 4.3	−33.3 ± 5.3	−31.4 ± 4.3
Agar (Yellow 1)	−55.3 ± 3.6	−44.9 ± 4.9	−40.6 ± 3	−27.7 ± 3	−28.8 ± 3.1
Agar (Yellow 2)	−51.9 ± 4.3	−40.1 ± 4	−33.9 ± 2.3	−22.3 ± 1.9	−21.1 ± 2
Agar (Blue)	−55.3 ± 3.4	−44.4 ± 3.6	−41.1 ± 2.2	−27.4 ± 2	−27.5 ± 2.2
Fat	−31.4 ± 11	−25.9 ± 6.6	−23.3 ± 5	−20.7 ± 3.3	−18.1 ± 1.9

Tissue	300 Hz	322.9 Hz	700 Hz	1.1 kHz	1.7 kHz	2.3 kHz
Bovine Liver	-18.1 ± 2.1	-20.4 ± 2.1	-19.1 ± 2	-17.5 ± 1.7	-16.2 ± 1.5	-16.2 ± 1.5
Poultry Liver	-20.5 ± 1.5	-23.3 ± 2.1	-21 ± 1.7	-18.6 ± 1.7	-16.3 ± 1.7	-15.7 ± 1.7
Bovine Muscle	-31.3 ± 2.9	-36.7 ± 3.4	-34.4 ± 3.7	-29.7 ± 3.5	-25.7 ± 3.3	-24.4 ± 3.1
Bovine Kidney	-24.5 ± 2.5	-28.3 ± 3.2	-25.6 ± 2.8	-22.2 ± 2.3	-19.1 ± 1.8	-18.1 ± 1.4
Ovary	-22.7 ± 3.5	-24.6 ± 3.3	-23.6 ± 3.2	-21.2 ± 3.1	-19 ± 3	-18.6 ± 2.9
Testes	-18.1 ± 5.6	-18.9 ± 6.1	-18.9 ± 5.7	-17.2 ± 5.2	-15.5 ± 4.8	-15.3 ± 4.5
Gelatin (Original)	-11.8 ± 2.8	-11.3 ± 2.1	-10.1 ± 1.2	-8.5 ± 1	-7.1 ± 0.8	-7.3 ± 0.8
Gelatin (Green)	-22.8 ± 5.2	-25.1 ± 4.7	-23.7 ± 4	-20.2 ± 3.1	-17.9 ± 2.9	-19.5 ± 3
Gelatin (Red)	-25.4 ± 4.5	-27.3 ± 4.9	-28.9 ± 4.7	-24.6 ± 4	-21.9 ± 4.5	-24.6 ± 5
Agar (Yellow 1)	-19.3 ± 2	-22.8 ± 2	-22.1 ± 1.5	-19.8 ± 1.6	-19 ± 2.2	-21 ± 2.3
Agar (Yellow 2)	-13.3 ± 1.5	-14.7 ± 1.6	-13.2 ± 1.6	-11.1 ± 1.3	-9.5 ± 1.3	-9.8 ± 1.4
Agar (Blue)	-18.5 ± 2	-20.8 ± 2	-20.1 ± 1.6	-17.8 ± 1.4	-16.7 ± 1.5	-17.9 ± 1.4
Fat	-14.8 ± 1.9	-15 ± 2.3	-14.7 ± 2.6	-13.3 ± 2.6	-11.8 ± 2.5	-11.5 ± 2.5

Tissue	3.1 kHz	11 kHz	17 Hz	23 kHz	31 kHz	43 kHz
Bovine Liver	-16.4 ± 1.5	-19.8 ± 1.9	-21.8 ± 2.3	-22.4 ± 2.6	-23.6 ± 2.9	-24 ± 3
Poultry Liver	-15 ± 1.7	-12.9 ± 1.4	-12.7 ± 1.2	-11.7 ± 1.1	-11.6 ± 1	-11.1 ± 0.9
Bovine Muscle	-22.6 ± 2.9	-15.1 ± 2.1	-13.6 ± 1.6	-11.1 ± 1.7	-10 ± 1.4	-8.1 ± 1.6
Bovine Kidney	-17.2 ± 1.1	-14.2 ± 1.2	-14.1 ± 1.2	-13 ± 1.5	-12.8 ± 1.6	-12.1 ± 1.8
Ovary	-18.1 ± 2.9	-16.6 ± 2.7	-16.7 ± 2.7	-15.4 ± 2.6	-15.2 ± 2.6	-14 ± 2.5
Testes	-15 ± 4.3	-13.6 ± 3.6	-13.7 ± 3.5	-12.9 ± 3.3	-13 ± 3.2	-12.4 ± 3.1
Gelatin (Original)	-7.3 ± 0.7	-7.7 ± 1.2	-7.2 ± 1.1	-6.6 ± 1.2	-6.2 ± 1.3	-5.7 ± 1.3
Gelatin (Green)	-19.4 ± 2.5	-27.9 ± 6	-27.6 ± 5.6	-25 ± 3.7	-25.5 ± 3.7	-22.3 ± 3.6
Gelatin (Red)	-24.6 ± 4.6	-34.6 ± 8.2	-34 ± 7.6	-31.1 ± 5.8	-33.2 ± 5.9	-28.9 ± 5.9
Agar (Yellow 1)	-20.6 ± 2.4	-23.9 ± 3.1	-24.7 ± 4.3	-23.8 ± 2.9	-23.9 ± 3.5	-21.9 ± 2.3
Agar (Yellow 2)	-9.6 ± 1.3	-11.1 ± 1.4	-10.9 ± 1.5	-9.8 ± 1.3	-9.5 ± 1.2	-8.6 ± 1.2
Agar (Blue)	-17.5 ± 1.2	-21.7 ± 2.1	-22.1 ± 2.7	-20.2 ± 1.7	-19.8 ± 1.9	-17.5 ± 1.2
Fat	-11.2 ± 2.4	-10.1 ± 1.9	-10.1 ± 1.8	-9.3 ± 1.6	-9.2 ± 1.5	-8.5 ± 1.4

Tissue	61 kHz	89 kHz	127 kHz	179 kHz	251 kHz	349 kHz
Bovine Liver	-24.5 ± 3.1	-24.1 ± 3	-22.7 ± 2.8	-20.2 ± 2.5	-16.2 ± 1.9	-10.2 ± 1.2
Poultry Liver	-11.3 ± 1	-11.4 ± 1.1	-11.3 ± 1.3	-11 ± 1.4	-9.5 ± 1.4	-6.4 ± 1
Bovine Muscle	-7.2 ± 1.4	-6.1 ± 1.3	-5.1 ± 1.2	-4.3 ± 1	-3.2 ± 0.8	-2 ± 0.4
Bovine Kidney	-12 ± 1.9	-11.7 ± 2	-11.2 ± 2	-10.4 ± 1.9	-8.6 ± 1.7	-5.7 ± 1.1
Ovary	-13.6 ± 2.4	-12.8 ± 2.2	-11.7 ± 2	-10.4 ± 1.7	-8.3 ± 1.3	-5.3 ± 0.8
Testes	-12.5 ± 3.1	-12.4 ± 3	-12 ± 2.9	-11.2 ± 2.7	-9.4 ± 2.3	-6.2 ± 1.5
Gelatin (Original)	-5.3 ± 1.3	-4.8 ± 1.3	-4.2 ± 1.2	-3.6 ± 1	-2.8 ± 0.8	-1.7 ± 0.5
Gelatin (Green)	-21.1 ± 3.8	-19.4 ± 3.9	-16.8 ± 3.8	-14.3 ± 3.4	-11.1 ± 2.7	-6.9 ± 1.6
Gelatin (Red)	-28.2 ± 5.8	-26.8 ± 5.8	-23.5 ± 5.7	-20.5 ± 4.9	-16 ± 4.1	-10 ± 2.4
Agar (Yellow 1)	-20.6 ± 2.4	-18.6 ± 2.2	-16.2 ± 1.7	-13.7 ± 1.5	-10.6 ± 1	-6.5 ± 0.7
Agar (Yellow 2)	-8.1 ± 1	-7.5 ± 1	-6.8 ± 0.9	-6 ± 0.8	-4.7 ± 0.7	-3 ± 0.4
Agar (Blue)	-16.2 ± 1.2	-14.6 ± 1.1	-12.7 ± 0.9	-11 ± 0.8	-8.6 ± 0.6	-5.4 ± 0.4
Fat	-8.3 ± 1.3	-8 ± 1.2	-7.5 ± 1.1	-6.9 ± 1.1	-5.7 ± 0.9	-3.7 ± 0.6

Appendix C

Freshly Excised Tissue Donor Data

Species	Breed	Age	Weight	Organ ID
Canine	Yorkshire Terrier	8 months	2.4 kg	Testes_S1 Testes_S2
Canine	German Shepard Mix	6 months	14.0 kg	Ovary_S1 Ovary_S2
Canine	German Shepard Mix	6 months	16.0 kg	Ovary_S3 Ovary_S4
Canine	Jack Russel Mix	8 months	8.0 kg	Ovary_S5 Ovary_S6
Canine	Golden Doodle	6 months	11.8 kg	Ovary_S7 Ovary_S8
Canine	Yorkie Mix	12 months	2.3 kg	Ovary_S9 Ovary_S10

Canine	Basenji	5 months	8.7 kg	Ovary_S11
				Ovary_S12
Feline	Unknown	Uknown	Unknown	Ovary_S13
				Ovary_S14
				Cyst
Canine	Mini Schnauzer	8 months	7.9 kg	Testes_S3
				Testes_S4
Canine	Golden Doodle	7 months	15.4 kg	Ovary_S15
				Ovary_S16
Canine	Cockapoo*	13 yrs old	9.1 kg	Testes_S5
				Testes_S6
	*Perianal Cyst Abscess			Tumor_$S1_1$
	*Perianal Cyst Abscess			Tumor_$S1_2$
Canine	German Shepard Mix	6 months	19.0 kg	Ovary_S17
				Ovary_S18
Canine	Husky Mix	6 months	18.1 kg	Ovary_S19
				Ovary_S20
Canine	Black Lab*	6 years	36.3 kg	Ovary_S21
	*4 days after excision			Ovary_S22
Canine	Schnauzer	7 months	12.7 kg	Ovary_S23
				Ovary_S24

Canine	Bernedoodle	6 months	28.1 kg	Testes_S7
				Testes_S8
Canine	German Shepard	18 months	40.8 kg	Testes_S9
				Testes_S10
Canine	French Bulldog Mix	6 months	9.5 kg	Testes_S11
				Testes_S12
Canine	Golden Doodle* *Oral growth	11 years	14.9 kg	Tumor_S2
Canine	Pomeranian Mix	9 months	5.5 kg	Testes_S13
				Testes_S14
Canine	Bernese Mountain Dog Mix* *Removed: 6/12/2020 Analyzed: 6/15/2020, S16 - Was undescended	13 months	31.7 kg	Testes_S15
				Testes_S16
Feline	Domestic Shorthair	8 months	5.5 kg	Testes_S17
				Testes_S18
Canine	Cocker Spaniel	7 months	7.7 kg	Ovary_S25
				Ovary_S26
Canine	Chocolate Lab	7 months	21.5 kg	Ovary_S27
				Ovary_S28

Canine	Mini Australian Shepherd	6 months	9.2 kg	Testes_19
				Testes_20
Canine	Pug	16 months	7.2 kg	Ovary_S29
				Ovary_S30
Canine	Husky Mix	12 months	58 lbs	Testes_21
				Testes_22

Bibliography

[1] Z. Wei, G. Wan, L. Gardi, G. Mills, D. Downey, and A. Fenster, "Robot-assisted 3d-trus guided prostate brachytherapy: System integration and validation," *Medical physics*, vol. 31, no. 3, pp. 539–548, 2004.

[2] Y. Yu, T. Podder, Y. Zhang, W.-S. Ng, V. Misic, J. Sherman, L. Fu, D. Fuller, E. Messing, D. Rubens *et al.*, "Robot-assisted prostate brachytherapy," in *International Conference on Medical Image Computing and Computer-Assisted Intervention*. Springer, 2006, pp. 41–49.

[3] H. Su, W. Shang, G. A. Cole, K. Harrington, and G. S. Fischer, "Haptic system design for mri-guided needle based prostate brachytherapy," in *2010 IEEE Haptics Symposium*. IEEE, 2010, pp. 483–488.

[4] B. Ihnatsenka and A. P. Boezaart, "Ultrasound: Basic understanding and learning the language," *International journal of shoulder surgery*, vol. 4, no. 3, p. 55, 2010.

[5] A. Ebeid and A. Elshamy, "Hypoechoic versus hypervascular lesion in the diagnosis of prostatic carcinoma," *African Journal of Urology*, vol. 24, no. 3, pp. 169–174, 2018.

[6] M. Norberg, L. Egevad, L. Holmberg, P. Sparen, B. Norlen, and C. Busch, "The sextant protocol for ultrasound-guided core biopsies of the prostate underestimates the presence of cancer," *Urology*, vol. 50, no. 4, pp. 562–566, 1997.

[7] T. Graif, S. Loeb, K. A. Roehl, S. N. Gashti, C. Griffin, X. Yu, and W. J. Catalona, "Under diagnosis and over diagnosis of prostate cancer," *The Journal of urology*, vol. 178, no. 1, pp. 88–92, 2007.

[8] B. Djavan, M. Remzi, C. C. Schulman, M. Marberger, and A. R. Zlotta, "Repeat prostate biopsy: who, how and when?: a review," *European urology*, vol. 42, no. 2, pp. 93–103, 2002.

[9] D. N. Costa, B. N. Bloch, D. F. Yao, M. G. Sanda, L. Ngo, E. M. Genega, I. Pedrosa, W. C. DeWolf, and N. M. Rofsky, "Diagnosis of relevant prostate cancer using supplementary cores from magnetic resonance imaging-prompted areas following multiple failed biopsies," *Magnetic resonance imaging*, vol. 31, no. 6, pp. 947–952, 2013.

[10] O. Acosta, A. Simon, F. Monge, F. Commandeur, C. Bassirou, G. Cazoulat, R. De Crevoisier, and P. Haigron, "Evaluation of multi-atlas-based segmentation of ct scans in prostate cancer radiotherapy," in *2011 IEEE International Symposium on Biomedical Imaging: From Nano to Macro.* IEEE, 2011, pp. 1966–1969.

[11] A. M. Okamura, "Methods for haptic feedback in teleoperated robot-assisted surgery," *Industrial Robot: An International Journal*, vol. 31, no. 6, pp. 499–508, 2004.

[12] T. Ortmaier, B. Deml, B. Kübler, G. Passig, D. Reintsema, and U. Seibold, "Robot assisted force feedback surgery," in *Advances in Telerobotics.* Springer, 2007, pp. 361–379.

[13] R. Kokes, K. Lister, R. Gullapalli, B. Zhang, A. MacMillan, H. Richard, and J. P. Desai, "Towards a teleoperated needle driver robot with haptic feedback for rfa of breast tumors under continuous mri," *Medical image analysis*, vol. 13, no. 3, pp. 445–455, 2009.

[14] W. Shang, H. Su, G. Li, and G. S. Fischer, "Teleoperation system with hybrid pneumatic-piezoelectric actuation for mri-guided needle insertion with haptic feedback," in *2013 IEEE/RSJ International Conference on Intelligent Robots and Systems.* IEEE, 2013, pp. 4092–4098.

[15] C. Rossa and M. Tavakoli, "Issues in closed-loop needle steering," *Control Engineering Practice*, vol. 62, pp. 55–69, 2017.

[16] S. Elayaperumal, J. H. Bae, D. Christensen, M. R. Cutkosky, B. L. Daniel, R. J. Black, J. M. Costa, F. Faridian, and B. Moslehi, "Mr-compatible biopsy needle with enhanced tip force sensing," in *2013 World Haptics Conference (WHC).* IEEE, 2013, pp. 109–114.

[17] A. M. Okamura, "Haptic feedback in robot-assisted minimally invasive surgery," *Current opinion in urology*, vol. 19, no. 1, p. 102, 2009.

[18] B. H. Brown, "Electrical impedance tomography (EIT): a review," *Journal of medical engineering & technology*, vol. 27, no. 3, pp. 97–108, 2003.

[19] V. Mishra, A. Schned, A. Hartov, J. Heaney, J. Seigne, and R. Halter, "Electrical property sensing biopsy needle for prostate cancer detection," *The Prostate*, vol. 73, no. 15, pp. 1603–1613, 2013.

[20] J. Jossinet, "The impedivity of freshly excised human breast tissue," *Physiological measurement*, vol. 19, no. 1, p. 61, 1998.

[21] A. Keshtkar, A. Keshtkar, and R. H. Smallwood, "Electrical impedance spectroscopy and the diagnosis of bladder pathology," *Physiological Measurement*, vol. 27, no. 7, p. 585, 2006.

[22] P. Åberg, U. Birgersson, P. Elsner, P. Mohr, and S. Ollmar, "Electrical impedance spectroscopy and the diagnostic accuracy for malignant melanoma," *Experimental dermatology*, vol. 20, no. 8, pp. 648–652, 2011.

[23] K. R. Foster, H. P. Schwan *et al.*, "Dielectric properties of tissues," *CRC handbook of biological effects of electromagnetic fields*, pp. 27–96, 1986.

[24] R. J. Halter, A. Schned, J. Heaney, A. Hartov, S. Schutz, and K. D. Paulsen, "Electrical impedance spectroscopy of benign and malignant prostatic tissues," *The Journal of urology*, vol. 179, no. 4, pp. 1580–1586, 2008.

[25] N. Vasylieva, S. Marinesco, D. Barbier, and A. Sabac, "Silicon/su8 multi-electrode micro-needle for in vivo neurochemical monitoring," *Biosensors and Bioelectronics*, vol. 72, pp. 148–155, 2015.

[26] J. Yun, G. Kang, Y. Park, H. W. Kim, J.-J. Cha, and J.-H. Lee, "Electrochemical impedance spectroscopy with interdigitated electrodes at the end of hypodermic needle for depth profiling of biotissues," *Sensors and Actuators B: Chemical*, vol. 237, pp. 984–991, 2016.

[27] R. J. Andrews and R. W. Mah, "The NASA smart probe project for real-time multiple microsensor tissue recognition," *Stereotactic and functional neurosurgery*, vol. 80, no. 1-4, pp. 114–119, 2003.

[28] J. Yun, Y.-T. Hong, K.-H. Hong, and J.-H. Lee, "Ex vivo identification of thyroid cancer tissue using electrical impedance spectroscopy on a needle," *Sensors and Actuators B: Chemical*, vol. 261, pp. 537–544, 2018.

[29] J. Park, W.-M. Choi, K. Kim, W.-I. Jeong, J.-B. Seo, and I. Park, "Biopsy needle integrated with electrical impedance sensing microelectrode array towards real-time needle guidance and tissue discrimination," *Scientific reports*, vol. 8, no. 1, p. 264, 2018.

[30] M. Grossi and B. Riccò, "Electrical impedance spectroscopy (eis) for biological analysis and food characterization: a review," *Journal of Sensors and Sensor Systems*, pp. 303 – 325, 2017, 10.1016/j.corsci.2008.08.049, HAL Id: hal-01579247.

[31] J. Kari, K. Annala, P. Annus, V.-P. Seppä, and K. Kronström, "A thin needle with bio-impedance measuring probe: tissue recognition performance assessed in in vivo animal study," *Injeq Oy Ltd., Tech. Rep*, 2015.

[32] C. Chassagne, D. Bedeaux, J. Van Der Ploeg, and G. Koper, "Theory of electrode polarization: application to parallel plate cell dielectric spectroscopy experiments," *Colloids and Surfaces A: Physicochemical and Engineering Aspects*, vol. 210, no. 2-3, pp. 137–145, 2002.

[33] H. Kalvøy, L. Frich, S. Grimnes, Ø. G. Martinsen, P. K. Hol, and A. Stubhaug, "Impedance-based tissue discrimination for needle guidance," *Physiological measurement*, vol. 30, no. 2, p. 129, 2009.

[34] D. Trebbels, F. Fellhauer, M. Jugl, G. Haimerl, M. Min, and R. Zengerle, "Online tissue discrimination for transcutaneous needle guidance applications using broadband impedance spectroscopy," *IEEE transactions on biomedical engineering*, vol. 59, no. 2, pp. 494–503, 2011.

[35] O. G. Martinsen and S. Grimnes, *Bioimpedance and bioelectricity basics*. Academic press, 2011, third Edition.

[36] C. J. De Luca and W. J. Forrest, "An electrode for recording single motor unit activity during strong muscle contractions," *IEEE Transactions on Biomedical Engineering*, vol. BME-19, no. 5, pp. 367–372, 1972.

[37] F. Yu, R. Li, L. Ai, C. Edington, H. Yu, M. Barr, E. Kim, and T. K. Hsiai, "Electrochemical impedance spectroscopy to assess vascular oxidative stress," *Annals of biomedical engineering*, vol. 39, no. 1, pp. 287–296, 2011.

[38] F. Yu, X. Dai, T. Beebe, and T. Hsiai, "Electrochemical impedance spectroscopy to characterize inflammatory atherosclerotic plaques," *Biosensors and Bioelectronics*, vol. 30, no. 1, pp. 165–173, 2011.

[39] M. Habibi, D. P. Klemer, and V. Raicu, "Two-dimensional dielectric spectroscopy: Implementation and validation of a scanning open-ended coaxial probe," *Review of Scientific Instruments*, vol. 81, no. 7, p. 075108, 2010.

[40] P. Azimi and H. Golnabi, "Precise formulation of electrical capacitance for a cylindrical capacitive sensor," *J. Appl. Sci*, vol. 9, no. 8, pp. 1556–1561, 2009.

[41] H. Schwan, "Electrode polarization impedance and measurements in biological materials," *Annals of the New York Academy of Sciences*, vol. 148, no. 1, pp. 191–209, 1968.

[42] M. Min, M. Lehti-Polojärvi, J. Hyttinen, M. Rist, R. Land, and P. Annus, "Bioimpedance spectro-tomography system using binary multifrequency excitation," *International Journal of Bioelectromagnetism*, vol. 209, pp. 76–79, 05 2018.

[43] M. Min, M. Lehti-Polojärvi, J. Hyttinen, M. Rist, R. Land, and P. Annus, "Bioimpedance spectro-tomography system using binary multifrequency excitation," *International Journal of Bioelectromagnetism*, vol. 209, pp. 76–79, 2018.

[44] M. Rist, M. Reidla, R. Land, T. Parve, O. Märtens, P. Annus, J. Ojarand, and M. Min, "Modular system for spectral analysis of time-variant impedances," in *6th European Conference*

of the International Federation for Medical and Biological Engineering. Springer, 2015, pp. 858–861.

[45] O. Martens, R. Land, M. Min, P. Annus, M. Rist, and M. Reidla, "Improved impedance analyzer with binary excitation signals," in *2015 IEEE 9th International Symposium on Intelligent Signal Processing (WISP) Proceedings.* IEEE, 2015, pp. 1–5.

[46] H. P. Schwan, "Electrical properties of tissues and cell suspensions: mechanisms and models," in *Proceedings of 16th Annual International Conference of the IEEE Engineering in Medicine and Biology Society*, vol. 1. IEEE, 1994, pp. A70–A71.

[47] D. Dean, T. Ramanathan, D. Machado, and R. Sundararajan, "Electrical impedance spectroscopy study of biological tissues," *Journal of electrostatics*, vol. 66, no. 3-4, pp. 165–177, 2008.

[48] S. Grimnes and Ø. G. Martinsen, "Alpha-dispersion in human tissue," in *Journal of Physics: Conference Series*, vol. 224, no. 1, 2010, pp. 1–4.

[49] F. Zhang, T. Jin, Q. Hu, and P. He, "Distinguishing skin cancer cells and normal cells using electrical impedance spectroscopy," *Journal of Electroanalytical Chemistry*, vol. 823, pp. 531–536, 2018.

[50] L. Geddes, "Historical evolution of circuit models for the electrode-electrolyte interface," *Annals of biomedical engineering*, vol. 25, no. 1, p. 1, 1997.

[51] E. Warburg, "Ueber das verhalten sogenannter unpolarisirbarer elektroden gegen wechselstrom," *Annalen der Physik*, vol. 303, no. 3, pp. 493–499, 1899.

[52] D. C. Grahame, "Mathematical theory of the faradaic admittance," *J. electrochem. Soc*, vol. 99, no. 12, pp. 370–385, 1952.

[53] G. Platt, "How do i convert a continuous-time model to a discrete-time model?" accessed: 2020-03-06.

[54] H. Fricke and S. Morse, "The electric resistance and capacity of blood for frequencies between 800 and 41/2 million cycles," *The Journal of general physiology*, vol. 9, no. 2, p. 153, 1925.

[55] A. Ivorra, M. Genescà, A. Sola, L. Palacios, R. Villa, G. Hotter, and J. Aguiló, "Bioimpedance dispersion width as a parameter to monitor living tissues," *Physiological measurement*, vol. 26, no. 2, p. S165, 2005.

[56] F. Zhang, B. Sanchez, S. B. Rutkove, Y. Yang, H. Zhong, J. Li, and Z. Teng, "Numerical estimation of fricke–morse impedance model parameters using single-frequency sinusoidal excitation," *Physiological measurement*, vol. 40, no. 9, p. 09NT01, 2019.

[57] K. Cole, "Dispersion and absorption in dielectrics," *J. Chem. Phys*, vol. 9, p. 341, 1941.

[58] T. J. Freeborn, B. Maundy, and A. S. Elwakil, "Extracting the parameters of the double-dispersion cole bioimpedance model from magnitude response measurements," *Medical & biological engineering & computing*, vol. 52, no. 9, pp. 749–758, 2014.

[59] A. Lasia, "Electrochemical impedance spectroscopy and its applications," in *Modern aspects of electrochemistry*. Springer, 2002, pp. 143–248.

[60] M. N. Kakaei, J. Neshati, and A. R. Rezaierod, "On the extraction of the effective capacitance from constant phase element parameters," *Protection of Metals and Physical Chemistry of Surfaces*, vol. 54, no. 3, pp. 548–556, 2018.

[61] A. S. Elwakil and B. Maundy, "Experimental technique for estimating the dispersion coefficient of a constant phase element," in *2011 20th European Conference on Circuit Theory and Design (ECCTD)*. IEEE, 2011, pp. 469–471.

[62] J. E. B. Randles, "Kinetics of rapid electrode reactions," *Discussions of the faraday society*, vol. 1, pp. 11–19, 1947.

[63] T. M. Nahir, "Impedance spectroscopy: Theory, experiment, and applications, edited by evgenij barsoukov (texas instruments inc.) and j. ross macdonald (university of north carolina, chapel hill). john wiley & sons, inc.: Hoboken, nj. 2005. xvii+ 596 pp. isbn 0471-64749-7." 2005.

[64] T. J. Freeborn, "A survey of fractional-order circuit models for biology and biomedicine," *IEEE Journal on emerging and selected topics in circuits and systems*, vol. 3, no. 3, pp. 416–424, 2013.

[65] B. Rigaud, L. Hamzaoui, M. Frikha, N. Chauveau, and J.-P. Morucci, "In vitro tissue characterization and modelling using electrical impedance measurements in the 100 hz-10 mhz frequency range," *Physiological measurement*, vol. 16, no. 3A, p. A15, 1995.

[66] B. J. Maundy, A. S. Elwakil, and A. Allagui, "Extracting the parameters of the single-dispersion cole bioimpedance model using a magnitude-only method," *Computers and Electronics in Agriculture*, vol. 119, pp. 153–157, 2015.

[67] D. A. McRae, M. A. Esrick, and S. C. Mueller, "Changes in the noninvasive, in vivo electrical impedance of three xenografts during the necrotic cell-response sequence," *International Journal of Radiation Oncology* Biology* Physics*, vol. 43, no. 4, pp. 849–857, 1999.

[68] A. Campbell and D. Land, "Dielectric properties of female human breast tissue measured in vitro at 3.2 ghz," *Physics in Medicine & Biology*, vol. 37, no. 1, p. 193, 1992.

[69] R. J. Halter, A. Schned, J. Heaney, A. Hartov, and K. D. Paulsen, "Electrical properties of prostatic tissues: I. single frequency admittivity properties," *the Journal of Urology*, vol. 182, no. 4, pp. 1600–1607, 2009.

[70] T. Dai and A. Adler, "Blood impedance characterization from pulsatile measurements," in *2006 Canadian Conference on Electrical and Computer Engineering*. IEEE, 2006, pp. 983–986.

[71] A. S. Bondarenko, "Analysis of large experimental datasets in electrochemical impedance spectroscopy," *Analytica chimica acta*, vol. 743, pp. 41–50, 2012.

[72] T. Springer, T. Zawodzinski, M. Wilson, and S. Gottesfeld, "Characterization of polymer electrolyte fuel cells using ac impedance spectroscopy," *Journal of the Electrochemical Society*, vol. 143, no. 2, p. 587, 1996.

[73] P. Bueschel, U. Troeltzsch, and O. Kanoun, "Use of stochastic methods for robust parameter extraction from impedance spectra," *Electrochimica Acta*, vol. 56, no. 23, pp. 8069–8077, 2011.

[74] J. M. Ortega and W. C. Rheinboldt, *Iterative solution of nonlinear equations in several variables*. Siam, 1970, vol. 30, edition from 2000 republication of 1970 publication.

[75] T. J. Yorkey, J. G. Webster, and W. J. Tompkins, "Comparing reconstruction algorithms for electrical impedance tomography," *IEEE Transactions on Biomedical Engineering*, vol. BME-34, no. 11, pp. 843–852, 1987.

[76] M. Elarbi, S. Bechikh, A. Gupta, L. B. Said, and Y.-S. Ong, "A new decomposition-based nsga-ii for many-objective optimization," *IEEE transactions on systems, man, and cybernetics: systems*, vol. 48, no. 7, pp. 1191–1210, 2017.

[77] K. Deb, A. Pratap, S. Agarwal, and T. Meyarivan, "A fast and elitist multiobjective genetic algorithm: Nsga-ii," *IEEE transactions on evolutionary computation*, vol. 6, no. 2, pp. 182–197, 2002.

[78] Z. Zhao, B. Liu, C. Zhang, and H. Liu, "An improved adaptive nsga-ii with multi-population algorithm," *Applied Intelligence*, vol. 49, no. 2, pp. 569–580, 2019.

[79] K. Deb and D. Deb, "Analysing mutation schemes for real-parameter genetic algorithms," *International Journal of Artificial Intelligence and Soft Computing*, vol. 4, no. 1, pp. 1–28, 2014.

[80] K. Deb, R. B. Agrawal *et al.*, "Simulated binary crossover for continuous search space," *Complex systems*, vol. 9, no. 2, pp. 115–148, 1995.

[81] K. Kumar and K. Deb, "Real-coded genetic algorithms with simulated binary crossover: Studies on multimodal and multiobjective problems," *Complex syst*, vol. 9, pp. 431–454, 1995.

[82] H.-R. Tränkler, O. Kanoun, M. Min, and M. Rist, "Smart sensor systems using impedance spectroscopy," *Proc. Estonian Acad. Sci. Eng*, vol. 13, no. 4, pp. 455–478, 2007.

[83] M. I. Lourakis *et al.*, "A brief description of the levenberg-marquardt algorithm implemented by levmar," *Foundation of Research and Technology*, vol. 4, no. 1, pp. 1–6, 2005.

[84] A. Helwan, J. B. Idoko, and R. H. Abiyev, "Machine learning techniques for classification of breast tissue," *Procedia computer science*, vol. 120, pp. 402–410, 2017.

[85] U. Birgersson, *Electrical impedance of human skin and tissue alterations: Mathematical modeling and measurements.* Inst för klinisk vetenskap, intervention och teknik/Dept of Clinical Science . . . , 2012.

[86] J. E. Da Silva, J. M. De Sá, and J. Jossinet, "Classification of breast tissue by electrical impedance spectroscopy," *Medical and Biological Engineering and Computing*, vol. 38, no. 1, pp. 26–30, 2000.

[87] J. Jossinet and B. Lavandier, "The discrimination of excised cancerous breast tissue samples using impedance spectroscopy," *Bioelectrochemistry and Bioenergetics*, vol. 45, pp. 161—-167, 1998.

[88] M. R. Daliri, "Combining extreme learning machines using support vector machines for breast tissue classification," *Computer methods in biomechanics and biomedical engineering*, vol. 18, no. 2, pp. 185–191, 2015.

[89] S. Laufer, A. Ivorra, V. E. Reuter, B. Rubinsky, and S. B. Solomon, "Electrical impedance characterization of normal and cancerous human hepatic tissue," *Physiological measurement*, vol. 31, no. 7, p. 995, 2010.

[90] S. Wasterlain, D. Candusso, F. Harel, X. François, and D. Hissel, "Diagnosis of a fuel cell stack using electrochemical impedance spectroscopy and bayesian networks," in *2010 IEEE Vehicle Power and Propulsion Conference.* IEEE, 2010, pp. 1–6.

[91] J. Kari, V. Seppä, K. Annala, and K. Kronström, "In-vivo tissue identification using bioimpedance spectroscopy with conventional anaesthesia needles."

[92] B. Zheng, M. E. Tublin, A. H. Klym, and D. Gur, "Classification of thyroid nodules using a resonance-frequency–based electrical impedance spectroscopy: A preliminary assessment," *Thyroid*, vol. 23, no. 7, pp. 854–862, 2013.

[93] P. Mulak and N. Talhar, "Analysis of distance measures using k-nearest neighbor algorithm on kdd dataset," *International Journal of Science and Research*, vol. 4, no. 7, pp. 2101–2104, 2015.

[94] K. B. Korb and A. E. Nicholson, *Bayesian artificial intelligence.* CRC press, 2010.

[95] S. Raschka, "Naive bayes and text classification i-introduction and theory," *arXiv preprint arXiv:1410.5329*, 2014.

[96] S. Theodoridis, *Machine learning: a Bayesian and optimization perspective*. Academic Press, 2015.

[97] H. Zhang and S. Sheng, "Learning weighted naive bayes with accurate ranking," in *Fourth IEEE International Conference on Data Mining (ICDM'04)*. IEEE, 2004, pp. 567–570.

[98] M. Kitagawa, D. Dokko, A. M. Okamura, and D. D. Yuh, "Effect of sensory substitution on suture-manipulation forces for robotic surgical systems," *The Journal of thoracic and cardiovascular surgery*, vol. 129, no. 1, pp. 151–158, 2005.

[99] M. Lacki and C. Rossa, "On the feasibility of multi-degree-of-freedom haptic devices using passive actuators," in *2019 IEEE/RSJ International Conference on Intelligent Robots and Systems (IROS)*. IEEE, 2019, pp. 7288–7293.

[100] E. P. Westebring-van der Putten, R. H. Goossens, J. J. Jakimowicz, and J. Dankelman, "Haptics in minimally invasive surgery–a review," *Minimally Invasive Therapy & Allied Technologies*, vol. 17, no. 1, pp. 3–16, 2008.

[101] J. T. Dennerlein, P. A. Millman, and R. D. Howe, "Vibrotactile feedback for industrial telemanipulators," in *Sixth Annual Symposium on Haptic Interfaces for Virtual Environment and Teleoperator Systems, ASME International Mechanical Engineering Congress and Exposition*, vol. 61, 1997, pp. 189–195.

[102] M. Khadem, C. Rossa, N. Usmani, R. S. Sloboda, and M. Tavakoli, "A two-body rigid/flexible model of needle steering dynamics in soft tissue," *IEEE/ASME Transactions on Mechatronics*, vol. 21, no. 5, pp. 2352–2364, 2016.

[103] Q. Li, G. Y. Lee, C. N. Ong, and C. T. Lim, "AFM indentation study of breast cancer cells," *Biochemical and biophysical research communications*, vol. 374, no. 4, pp. 609–613, 2008.

[104] T. Krouskop, T. Wheeler, F. Kallel, B. Garra, and T. Hall, "Elastic moduli of breast and prostate tissues under compression," *Ultrasonic imaging*, vol. 20, no. 4, pp. 260–274, 1998.

[105] M. P. Ottensmeyer and J. K. Salisbury, "In vivo data acquisition instrument for solid organ mechanical property measurement," in *Int. Conf. on Medical Image Computing and Computer-Assisted Intervention*. Springer, 2001, pp. 975–982.

[106] T. Lehmann, C. Rossa, N. Usmani, R. S. Sloboda, and M. Tavakoli, "Intraoperative tissue young's modulus identification during needle insertion using a laterally actuated needle," *IEEE Transactions on Instrumentation and Measurement*, vol. 67, no. 2, pp. 371–381, 2017.

[107] A. Markidou, W. Y. Shih, and W.-H. Shih, "Soft-materials elastic and shear moduli measurement using piezoelectric cantilevers," *Review of Scientific Instruments*, vol. 76, no. 6, p. 064302, 2005.

[108] T. J. Hall, M. Bilgen, M. F. Insana, and T. A. Krouskop, "Phantom materials for elastography," *IEEE transactions on ultrasonics, ferroelectrics, and frequency control*, vol. 44, no. 6, pp. 1355–1365, 1997.

[109] C. Russell, A. C. Ward, V. Vezza, P. Hoskisson, D. Alcorn, D. P. Steenson, and D. K. Corrigan, "Development of a needle shaped microelectrode for electrochemical detection of the sepsis biomarker interleukin-6 (il-6) in real time," *Biosensors and Bioelectronics*, vol. 126, pp. 806–814, 2019.

[110] X. Yu, H. Wang, X. Ning, R. Sun, H. Albadawi, M. Salomao, A. C. Silva, Y. Yu, L. Tian, A. Koh *et al.*, "Needle-shaped ultrathin piezoelectric microsystem for guided tissue targeting via mechanical sensing," *Nature biomedical engineering*, vol. 2, no. 3, pp. 165–172, 2018.

[111] G. Chornokur, S. K. Arya, C. Phelan, R. Tanner, and S. Bhansali, "Impedance-based miniaturized biosensor for ultrasensitive and fast prostate-specific antigen detection," *Journal of Sensors*, vol. 2011, 2011.

[112] M. J. Pitts, M. A. Williams, T. Wellings, and A. Attridge, "Assessing subjective response to haptic feedback in automotive touchscreens," in *Proceedings of the 1st international Conference on Automotive User interfaces and interactive Vehicular Applications*, 2009, pp. 11–18.

[113] C. Geitner, S. Birrell, C. Krehl, and P. Jennings, "Haptic foot pedal: Influence of shoe type, age, and gender on subjective pulse perception," *Human factors*, vol. 60, no. 4, pp. 496–509, 2018.